EVOLUTION OF THE GALAXY - DARK MATTER CONNECTION AND THE ASSEMBLY OF GALAXIES IN DARK MATTER HALOS

Xiaohu Yang[1], H.J. Mo [2], Frank C. van den Bosch[3], Youcai Zhang[1], Jiaxin Han[1]

Draft version March 29, 2012

ABSTRACT

We present a new model to describe the galaxy-dark matter connection across cosmic time, which unlike the popular subhalo abundance matching technique is self-consistent in that it takes account of the facts that (i) subhalos are accreted at different times, and (ii) the properties of satellite galaxies may evolve after accretion. Using observations of galaxy stellar mass functions out to $z \sim 4$, the conditional stellar mass function at $z \sim 0.1$ obtained from SDSS galaxy group catalogues, and the two-point correlation function (2PCF) of galaxies at $z \sim 0.1$ as function of stellar mass, we constrain the relation between galaxies and dark matter halos over the entire cosmic history from $z \sim 4$ to the present. This relation is then used to predict the median assembly histories of different stellar mass components within dark matter halos (central galaxies, satellite galaxies, and halo stars). We also make predictions for the 2PCFs of high-z galaxies as function of stellar mass. Our main findings are the following: (i) Our model reasonably fits all data within the observational uncertainties, indicating that the ΛCDM concordance cosmology is consistent with a wide variety of data regarding the galaxy population across cosmic time. (ii) At low-z, the stellar mass of central galaxies increases with halo mass as $M^{0.3}$ and $M^{\gtrsim 4.0}$ at the massive and low-mass ends, respectively. The ratio $M_{*,c}/M$ reveals a maximum of ~ 0.03 at a halo mass $M \sim 10^{11.8} h^{-1} M_\odot$, much lower than the universal baryon fraction (~ 0.17). At higher redshifts the maximum in $M_{*,c}/M$ remains close to ~ 0.03, but shifts to higher halo mass. (iii) The inferred time-scale for the disruption of satellite galaxies is about the same as the dynamical friction time scale of their subhalos. (iv) The stellar mass assembly history of central galaxies is completely decoupled from the assembly history of its host halo; the ratio $M_{*,c}/M$ initially increases rapidly with time until the halo mass reaches $\sim 10^{12} h^{-1} M_\odot$, at which point $M_{*,c}/M \sim 0.03$. Once $M \gtrsim 10^{12} h^{-1} M_\odot$, there is little growth in $M_{*,c}$, causing the ratio $M_{*,c}/M$ to decline. In Milky-Way sized halos more than half of the central stellar mass is assembled at $z \lesssim 0.5$. (v) In low mass halos, the accretion of satellite galaxies contributes little to the formation of their central galaxies, indicating that most of their stars must have formed *in situ*. In massive halos more than half of the stellar mass of the central galaxy has to be formed *in situ*, and the accretion of satellites can only become significant at $z \lesssim 2$. (vi) The total mass in halo stars is more than twice that of the central galaxy in massive halos, but less than 10 percent of $M_{*,c}$ in Milky Way sized halos. (vii) The 2PCFs of galaxies on small scales holds important information regarding the evolution of satellite galaxies, and at high-z is predicted to be much steeper than at low-z, especially for more massive galaxies. We discuss various implications of our findings regarding the formation and evolution of galaxies in a ΛCDM cosmology.

Subject headings: dark matter - large-scale structure of universe - galaxies: halos

1. INTRODUCTION

In recent years, much effort has been made to establish the statistical connection between galaxies and dark matter halos, as parameterized via the conditional luminosity function (CLF) (Yang, Mo & van den Bosch 2003) or the halo occupation distribution (HOD) (Jing et al. 1998; Peacock & Smith 2000). This galaxy-dark matter connection describes how galaxies with different properties occupy halos of different mass, and yields important insight into how galaxies form and evolve in dark matter halos. In practice, the various methods that have been used to constrain the galaxy-dark mat-

ter connection (galaxy clustering, galaxy-galaxy lensing, galaxy group catalogues, abundance matching, satellite kinematics) use the fact that the halo properties, such as mass function, mass profile, and clustering, are well understood in the current ΛCDM model of structure formation (e.g., Mo, van den Bosch & White 2010).

At low-redshift, large redshift surveys, such as the two-degree Field Galaxy Redshift Survey (2dFGRS; Colless et al. 2001) and the Sloan Digital Sky Survey (SDSS; York et al. 2000), have provided accurate estimates of the luminosity and stellar mass functions of galaxies (e.g., Norberg et al. 2002b; Blanton et al. 2003; Li & White 2009), of their two-point correlation functions (2PCF) as function of various galaxy properties (e.g., Norberg et al. 2002a; Zehavi et al. 2005, 2011; Wang et al. 2007), their satellite kinematics (e.g., van den Bosch et al. 2004; More et al. 2009, 2011), and even of their excess surface densities, a measure for the tangential shear caused by gravitational lensing due to their mass distributions

[1] Key Laboratory for Research in Galaxies and Cosmology, Shanghai Astronomical Observatory; Nandan Road 80, Shanghai 200030, China; E-mail: xhyang@shao.ac.cn
[2] Department of Astronomy, University of Massachusetts, Amherst MA 01003-9305
[3] Astronomy Department, Yale University, P.O. Box 208101, New Haven, CT 06520-8101

(e.g., Mandelbaum et al. 2005). All these results have been used to infer how galaxies with different properties are distributed in halos of different masses (e.g. Jing et al. 1998; Peacock & Smith 2000; Yang et al. 2003; van den Bosch et al. 2003a, 2007; Zheng et al. 2005; Tinker et al. 2005; Mandelbaum et al. 2006; Brown et al. 2008; More et al. 2009, 2011; Cacciato et al. 2009; Neistein et al. 2011a,b; Avila-Reese & Firmani 2011). In addition, these large galaxy redshift surveys can also be used to identify galaxy systems (groups), defined as those galaxies that share a common dark matter host halo (Yang et al. 2005a; 2007). Such group catalogs can be used to examine the halo - galaxy connection even more directly than the methods mentioned above (e.g., Eke et al. 2004; Yang et al. 2005b, 2008, 2009b). These analyses have revealed a number of important properties regarding the relation between galaxies and their dark matter halos. The stellar mass to halo mass ratio has a minimum for halos of $\sim 10^{12}\,h^{-1}\mathrm{M}_\odot$, and increases rapidly towards both lower and higher halo masses (Yang et al. 2003, 2005b, 2008, 2009b; van den Bosch et al. 2003a; Tinker et al. 2005; Leauthaud et al. 2012), suggesting that galaxy formation is most efficient in halos with a present-day mass of $\sim 10^{12}\,h^{-1}\mathrm{M}_\odot$, i.e., these halos have the highest integrated star formation efficiencies. Yet, their total stellar masses are only a few percent of that of the halo, indicating that the overall star formation efficiency is very low.

Ideally, we would like to carry out similar analyses at various redshifts, so as to investigate how star formation proceeds and how galaxies assemble as their host halos grow within the cosmic density field. Such analyses are now becoming possible at intermediate redshift, $z \sim 1$, where reliable luminosity and stellar mass functions of galaxies have been obtained from various redshift surveys, such as the DEEP2 survey (Davis et al. 2003), the COMBO-17 survey (Wolf et al. 2004), VVDS (Le Fevre et al. 2005), and zCOSMOS (Lilly et al. 2007). In addition, these surveys have been used to measure the 2PCFs of galaxies as function of their luminosity, stellar mass and/or color (e.g., Daddi et al. 2003; Coil et al. 2006; Phleps et al. 2006; Pollo et al. 2006; Mc-Cracken et al. 2008; Meneux et al. 2008, 2009; Foucaud et al. 2010; de la Torre et al. 2010). These observations have prompted a series of investigations into the galaxy-dark matter connection and its evolution between $z \sim 1$ and the present (e.g., Bullock et al. 2002; Moustakas & Somerville 2002; Yan et al. 2003; Zheng 2004; Lee et al. 2006; Hamana et al. 2006; Cooray 2005, 2006; Cooray & Ouchi 2006; Conroy et al. 2005, 2007; White et al. 2007; Zheng et al. 2007; Conroy & Wechsler 2009; Wang & Jing 2010; Wetzel & White 2010; Wang & Jing 2010; Leauthaud et al. 2011; Wake et al. 2011).

With the advent of deep, multi wave-band surveys, it has even become possible to estimate the luminosity/stellar mass functions of galaxies out to $z \sim 8$ (e.g. Drory et al. 2005; Fontana et al. 2006; Perez-Gonzalez et al. 2008; Marchesini et al. 2009; Stark et al. 2009; Bouwens et al. 2011). However, the data samples are still small (and hence subject to cosmic variance), with large discrepancies among different measurements (see Marchesini et al. 2009). Furthermore, since reliable clustering measurements are in general unavailable for these high redshift galaxy samples, it is not possible to carry out the same HOD/CLF analyses for these high-z galaxies as for galaxies at low z. Nevertheless, attempts have been made to establish the relation between galaxies and their dark matter halos out to high z using a technique known as abundance matching, in which galaxies of a given luminosity or stellar mass are linked to dark matter halos of given mass by matching the observed abundance of the galaxies in question to the halo abundance obtained from the halo mass function (typically also accounting for subhalos). This approach was first used by Mo & Fukugita (1996) and Mo, Mao & White (1999) to model the number density and clustering of Lyman-break galaxies. More recently, several studies have used abundance matching techniques to probe the galaxy-dark matter connection out to $z \sim 5$ (e.g., Vale & Ostriker 2004, 2006; Conroy, Wechsler & Kravtsov 2006; Shankar et al. 2006; Conroy & Wechsler 2009; Moster et al. 2010; Guo et al. 2010; Behroozi, Conroy & Weschler 2010).

An important aspect of abundance matching is the treatment of dark matter subhalos. It is usually assumed that a central galaxy resides at the center of each halo, and orbiting around it are satellite galaxies associated with the subhalos of the host halo. These subhalos were distinctive (host) halos themselves before they were accreted into their hosts, namely satellite galaxies were themselves central galaxies before their host halo became a subhalo. The modeling of the total galaxy population can therefore be separated into two parts: (i) the formation of central galaxies in dark matter halos at different redshifts, and (ii) the accretion and evolution of satellite galaxies in their host halos. With the use of high-resolution numerical simulations and extended Press-Schechter theory (Bond et al. 1991; Lacey & Cole 1993), the properties of the subhalo population have now been determined with great accuracy (e.g. Gao et al. 2004; De Lucia et al. 2004; Tormen et al. 2004; van den Bosch et al. 2005a; Weller et al. 2005; Diemand et al. 2007; Giocoli et al. 2008; Li & Mo 2009). If satellite galaxies are indeed associated with subhalos, these properties should be relevant to the modeling of the galaxy population. In particular, since subhalos were host halos before accretion, the subhalo property that seems most relevant is its mass *at the time of accretion*. Consequently, many abundance matching studies to date have linked galaxies of property $\mathcal{P}$ (i.e., galaxy luminosity or stellar mass) to dark matter (sub)-halos of mass M using

$$\int_{\mathcal{P}}^{\infty} n_{\mathrm{g}}(\mathcal{P}, z)\,\mathrm{d}\mathcal{P} = \int_{M}^{\infty} n_{\mathrm{h}}(M, z)\,\mathrm{d}M$$
$$+ \int_{M}^{\infty} n_{\mathrm{sub}}(m_a, z)\,\mathrm{d}m_a. \quad (1)$$

Here $n_{\mathrm{g}}(\mathcal{P}, z)$ is the comoving number density of galaxies of property $\mathcal{P}$ at redshift z, $n_{\mathrm{h}}(M, z)$ is the halo mass function at redshift z, and $n_{\mathrm{sub}}(m_a, z)$ is the comoving number density of subhaloes identified at redshift z which at accretion have a mass m_a. Hence, in such abundance matching the property of a satellite galaxy is assumed to depend only on its halo mass at accretion.

Although subhalo abundance matching yields galaxy correlation functions that are in remarkably good agreement with observations (e.g., Conroy et al. 2006; Guo et al. 2010; Wang & Jing 2010), it implies a particular path for the evolution of satellite galaxies. Indeed,

assuming that the stellar masses of satellite galaxies depend only on their halo mass at accretion implies either that the relation between $\mathcal{P}$ and halo mass M is independent of the time when the subhalo is accreted, and the evolution after accretion is independent of the host halo into which the subhalo has been accreted and how long ago it has been accreted, or that the effects of different accretion times and subsequent evolutions in different hosts conspire to give a stellar mass that depends only on the mass of the subhalo at accretion. Such evolution of satellites is neither physically motivated nor the only possible path which satellite galaxies could take. In fact, applying the abundance matching technique as described above to data at different z results in a $\mathcal{P}(M)$ relation that changes with redshift (e.g., Conroy et al. 2006; Conroy & Wechsler 2009; Moster et al. 2010; Wang & Jing 2010). If one accepts that $\mathcal{P}$ for central galaxies depends on both M and z, then the properties of satellite galaxies do not just depend on the host halo mass at accretion, m_a, but also on the accretion redshift, z_a. Furthermore, after accretion a satellite galaxy may lose or gain stellar mass and even be disrupted due to tidal stripping and disruption, such that $\mathcal{P}$ of satellite galaxies may depend on other properties in addition to both m_a and z_a. So far these effects have not been modeled in any detail in abundance-matching studies.

In this paper, we develop a new, self-consistent approach to model the relation between galaxies and dark matter halos over cosmic time. Our approach is based on the model of Yang et al. (2011), which gives subhalo abundance as a function of both mass at accretion and accretion time. This allows us to use a galaxy-halo relation that depends on subhalo accretion time and to follow the dynamical evolution after their accretion. Furthermore, since satellites observed in halos (galaxy systems) at the present time are 'fossil records' of both the formation of central galaxies at high-z and the subsequent dynamical evolution, the observed abundance and clustering of satellite galaxies at the present time can be used to constrain the galaxy - halo relations at different redshifts. In the present work, we use our model together with various observational data to obtain the stellar mass - halo mass relation as a function of redshift from $z \sim 4$ to the present. This paper is organized as follows. In Section 2 we outline the halo model ingredients to be used. In Section 3 we describe how we model the stellar mass function, the conditional stellar mass function, and the two point correlation function of galaxies. The observational constraints used for our analysis are presented in Section 4. The results are presented in Section 5, while Section 6 describes the implications regarding the assembly of galaxies and the evolution of the galaxy dark matter connection. We summarize our results in Section 7, which also includes a detailed discussion regarding various implications for galaxy formation and evolution.

Throughout this paper we will mostly focus on a ΛCDM 'concordance' cosmology whose parameters are consistent with the seventh-year data release of the WMAP mission (Komatsu et al. 2011; hereafter WMAP7). However, in order to investigate the possible cosmology dependence of our results, we also present results for the following set of ΛCDM cosmologies: WMAP1, with parameters consistent with the first-year data release of the WMAP mission (Spergel et

TABLE 1
ΛCDM COSMOLOGICAL MODELS USED IN THIS PAPER.

Name	Ω_{m}	Ω_{Λ}	n_s	h	σ_8
WMAP1	0.30	0.70	1.00	0.70	0.90
WMAP3	0.238	0.762	0.951	0.73	0.75
WMAP5	0.258	0.742	0.963	0.719	0.796
WMAP7	0.275	0.725	0.968	0.702	0.816
Millennium	0.25	0.75	1.00	0.73	0.90

al. 2003); WMAP3, with parameters given in Spergel et al. (2007); WMAP5, with parameters given in Dunkley et al. (2009), and finally a cosmology ('Millenium') with parameters that are identical to those adopted in Springel et al. (2005) for the Millennium Simulation. Table 1 lists the parameters for all these cosmologies.

2. DARK MATTER HALOS AND SUBHALOS

The main goal of this paper is to obtain a self-consistent model for the link between galaxies and dark matter halos accross cosmic time. In this section we describe our model ingredients for halos and subhalos that are needed for our investigation.

2.1. Dark Matter Halo Mass Function

The mass function of dark matter halos, $n_{\mathrm{h}}(M, z)\,\mathrm{d}M$, describes the number density of dark matter halos of mass M at redshift z. The Press-Schechter formalism (Press & Schechter 1974) yields an analytical estimate for $n_{\mathrm{h}}(M, z)$, and we use the revised form given in Sheth, Mo & Tormen (2001) based on the ellipsoidal collapse model:

$$n_{\mathrm{h}}(M, z)\,\mathrm{d}M = \frac{\overline{\rho}}{M^2}\nu f(\nu) \left| \frac{\mathrm{d}\ln\sigma}{\mathrm{d}\ln M} \right| \mathrm{d}M, \qquad (2)$$

where $\bar{\rho}$ is the mean matter density of the Universe at z, $\sigma(M)$ is the mass variance, and $\nu = \delta_{\mathrm{c}}(z)/\sigma(M)$ with $\delta_{\mathrm{c}}(z)$ the critical over-density required for collapse at redshift z. The function $f(\nu)$ is given by

$$\nu f(\nu) = 2A \left(1 + \frac{1}{\nu'^{2q}} \right) \left(\frac{\nu'^2}{2\pi} \right)^{1/2} \exp\left(-\frac{\nu'^2}{2} \right) \quad (3)$$

with $\nu' = \sqrt{a}\,\nu$, $a = 0.707$, $q = 0.3$ and $A \approx 0.322$. The resulting mass function has been shown to be in excellent agreement with numerical simulations, as long as halo masses are defined as the masses inside a sphere with an average over-density of about 180 that of the background mass density (Sheth & Tormen 1999; Jenkins et al. 2001). As an illustration, the left-hand panel of Fig. 1 shows the halo mass functions at several redshifts for the WMAP7 cosmology, predicted using Eq. (2).

2.2. Halo Density Profile

Throughout this paper we assume that dark matter halos are spherical and follow an NFW density profile (e.g., Navarro, Frenk & White 1997):

$$\rho(r) = \frac{\overline{\delta}\,\overline{\rho}}{(r/r_{\mathrm{s}})(1 + r/r_{\mathrm{s}})^2}, \qquad (4)$$

where r_{s} is a characteristic radius, and $\bar{\delta}$ is a dimensionless amplitude which can be expressed in terms of the
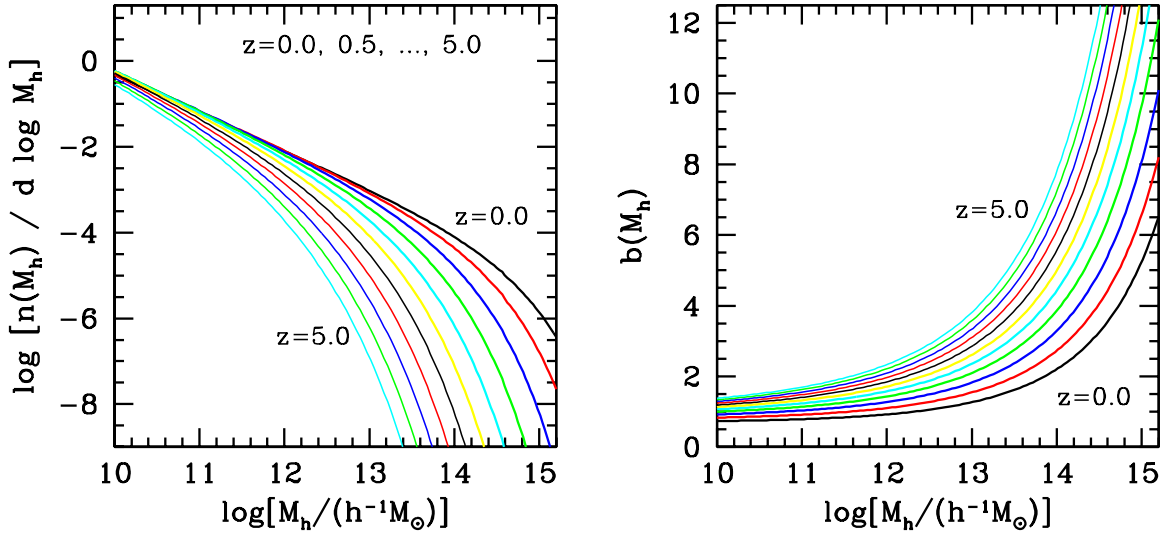
FIG. 1.— Left panel: the halo mass functions predicted using the Sheth Mo & Tormen (2001) model for the WMAP7 cosmology at different redshifts, as indicated. Right panel: the bias parameter of dark matter halos, again predicted using the Sheth, Mo & Tormen (2001) model for the WMAP7 cosmology at the same redshifts as those indicated in the left panel.

halo concentration parameter $c \equiv r_{180}/r_s$ as

$$\bar{\delta} = \frac{180}{3} \frac{c^3}{\ln(1+c) - c/(1+c)} . \qquad (5)$$

Numerical simulations have shown that c is correlated with halo mass (e.g., NFW; Eke et al. 2001; Jing & Suto 2000; Bullock et al. 2001; Zhao et al. 2003; 2009; Macciò et al. 2007). Throughout this paper we use the concentration-mass relation of Zhao et al. (2009), properly corrected for our definition of halo mass.

2.3. Halo Bias

Dark matter halos are biased tracers of the dark matter mass distribution. The amplitude of this bias depends on halo mass and is expressed via the halo bias function, $b_h(M)$ (e.g., Mo & White 1996, 2002). This allows one to write the two point correlation function between halos of masses M_1 and M_2 on large scales as

$$\xi_{hh}(r|M_1, M_2) = b_h(M_1)\, b_h(M_2)\, \xi_{dm}(r)\,, \qquad (6)$$

where $\xi_{dm}(r)$ is the two-point correlation function of the (non-linear) dark matter mass distribution. Throughout this paper we adopt the halo bias function of (Sheth, Mo & Tormen 2001), which is given by

$$b_h(M) = 1 + \frac{1}{\sqrt{a}\delta_c} \left[\sqrt{a}\,(a\nu^2) + \sqrt{a}\,b\,(a\nu^2)^{1-c} - \frac{(a\nu^2)^c}{(a\nu^2)^c + b\,(1-c)(1-c/2)} \right], \qquad (7)$$

with $a = 0.707$, $b = 0.5$, $c = 0.6$ and $\nu = \delta_c/\sigma(M)$. Note that our halo mass function (3) and halo bias function (7) obey the normalization condition

$$\int b_h(\nu)\, f(\nu)\, d\nu = 1 \qquad (8)$$

which expresses that the distribution of dark matter is, by definition, unbiased with respect to itself. As an illustration, the right-hand panel of Fig. 1 shows the halo

bias factor, $b_h(M)$ at several redshifts for the WMAP7 cosmology, predicted using Eq. (7).

2.4. The Subhalo Population

An important ingredient of our model describing the link between galaxies and dark matter halos is a statistical description for the population of dark matter subhalos. In particular, we need to know the distribution of accretion masses, m_a, and accretion redshifts, z_a, for the population of subhalos, as a function of the mass of its host halo. Let $n_{sub}(m_a, z_a|M, z)\, dm_a\, d\ln(1 + z_a)$ denote the number of subhalos in a host halo of mass M at redshift z, as a function of their accretion masses, m_a, and accretion redshifts, z_a. We will refer to n_{sub} as the subhalo mass function (SHMF). In the past, the subhalo mass function has typically been studied using N-body simulations or Monte-Carlo realizations of the extended Press-Schechter formalism (e.g., Sheth & Lemson 1999; Somerville & Kolatt 1999; Cole et al. 2000; van den Bosch et al. 2005a; Giocoli et al. 2008a; Cole et al. 2008; Parkinson et al. 2008; Fakhouri & Ma 2008; Fakhouri et al. 2010). Recently, however, Yang et al. (2011; hereafter Y11) presented a fully analytical model for $n_{sub}(m_a, z_a|M, z)$ which is the one we will adopt here. Following their notation we have that

$$n_{sub,0}(m_a, z_a|M, z) = m_a^{-1} \mathcal{N}_a(s_a, \delta_a|S, \delta)\,, \qquad (9)$$

where $s_a = \sigma^2(m_a)$, $S = \sigma^2(M)$, $\delta_a = \delta_c(z_a)$, $\delta = \delta_c(z)$, and the subscript '0' on the SHMF indicates that this function ignores higher order subhalos (subhalos of subhalos, etc; see below). Y11 considered three different models for $\mathcal{N}_a(s_a, \delta_a|S, \delta)$, and we adopt their Model III which is the most accurate. For host halos of given (M, z), this model uses the mean halo assembly history given by the fitting formula of Zhao et al. (2009) and a log-normal model to describe the scatter among different halos (see Section 3 of Y11 for details). Note that this SHMF only includes subhalos that are *directly* accreted onto the main branch of the host halo (hence the subscript '0'). However, since the SHMF given by Eq. (9)

also applies to subhalos before their accretion (when they themselves were host halos), we can in principle calculate the SHMF including higher level sub-halos, i.e., subhalos within sub-halos, etc. For example, the SHMF of sub^i-subhalos (ith level subhalos) can be written as

$$n_{\mathrm{sub},i}(m_a, z_a|M, z) = \int \int n_{\mathrm{sub},i-1}(m_a, z_a|m_{i-1}, z_{i-1})$$
$$\times n_{\mathrm{sub},0}(m_{i-1}, z_{i-1}|M, z)\, \mathrm{d}m_{i-1}\, \mathrm{d}\ln(1 + z_{i-1}). \quad (10)$$

Thus the total subhalo population can be described using

$$n_{\mathrm{sub}}(m_a, z_a|M, z) = \sum_{i=0}^{N_{\max}} n_{\mathrm{sub},i}(m_a, z_a|M, z). \quad (11)$$

In practice, we find that the sub^i-subhalos for $i \geq 2$ contribute less that 5% to $n_{\mathrm{sub}}(m_a, z_a|M, z)$ in the mass range of interest here ($\gtrsim 10^{10}\, h^{-1}\mathrm{M}_\odot$), and we therefore adopt $N_{\max} = 1$ in what follows (see also Yang, Mo & van den Bosch 2009a).

3. MODELING MASS FUNCTIONS AND CORRELATION FUNCTIONS

3.1. The Stellar Mass Functions

In the conditional luminosity (stellar mass) function model developed by Yang et al. (2003), the stellar mass function of galaxies at a given redshift z can be written as

$$\Phi(M_*, z) = \int_0^\infty \Phi(M_*|M, z)\, n_{\mathrm{h}}(M, z)\, \mathrm{d}M, \quad (12)$$

where $\Phi(M_*|M, z)$ is the conditional stellar mass function (CSMF), which gives the mean number of galaxies with stellar masses in the range $M_* \pm \mathrm{d}M_*/2$ hosted by halos of mass M at z. In general, we split the CSMF in two parts,

$$\Phi(M_*|M, z) = \Phi_{\mathrm{c}}(M_*|M, z) + \Phi_{\mathrm{s}}(m_*|M, z). \quad (13)$$

where $\Phi_{\mathrm{c}}(M_*|M, z)$ and $\Phi_{\mathrm{s}}(m_*|M, z)$ are the contributions from the central and satellite galaxies, respectively. Once $\Phi(M_*|M, z)$ is known, the average halo occupation number (HON) of galaxies within a given stellar mass range, $M_{*,1} < M_* < M_{*,2}$ can be written as

$$\langle N|M, z \rangle = \int_{M_{*,1}}^{M_{*,2}} \Phi(M_*|M, z)\, \mathrm{d}M_*. \quad (14)$$

Using Eq. (13) we write

$$\langle N|M, z \rangle = \langle N_{\mathrm{c}}|M, z \rangle + \langle N_{\mathrm{s}}|M, z \rangle, \quad (15)$$

where N_{c} and N_{s} are the occupation numbers of central and satellite galaxies, respectively.

3.1.1. The Conditional Stellar Mass Function of Central Galaxies

Based on the results of Yang et al. (2009b, hereafter Y09b), we assume that the CSMF of central galaxies is given by a lognormal distribution:

$$\Phi_{\mathrm{c}}(M_*|M, z) = \frac{1}{\sqrt{2\pi}\sigma_c} \exp\left[-\frac{(\log M_*/M_{*,c})^2}{2\sigma_c^2} \right], \quad (16)$$

where $\log M_{*,c}$ is the expectation value of the (10-based) logarithm of the stellar mass of the central galaxy and σ_c

is the dispersion. For simplicity, throughout the paper, we assume σ_c to be independent of halo mass.

Numerous studies have attempted to constrain the relation between $M_{*,c}$ and M and its evolution with redshift (see Section 1). Following Y09b, we assume that this relation has the form of a broken power-law:

$$M_{*,c} = M_{*,0} \frac{(M/M_1)^{\alpha+\beta}}{(1 + M/M_1)^\beta}, \quad (17)$$

so that $M_{*,c} \propto M^{\alpha+\beta}$ ($M_{*,c} \propto M^\alpha$) for $M \ll M_1$ ($M \gg M_1$). This model contains four free parameters: an amplitude $M_{*,0}$, a characteristic halo mass, M_1, and two power-law slopes, α and β. Note that all four parameters may depend on redshift, which we will parameterize accordingly in Section 4.3 below.

3.1.2. The Conditional Stellar Mass Function of Satellite Galaxies

The conditional stellar mass function for satellite galaxies can formally be written as,

$$\Phi_{\mathrm{s}}(m_*|M, z)$$
$$= \int_0^\infty \mathrm{d}\log m_*' \int_0^\infty \mathrm{d}m_a \int_z^\infty \frac{\mathrm{d}z_a}{1 + z_a} \int_0^M \mathrm{d}M_a \int_0^1 \mathrm{d}\eta$$
$$P(m_*|m_*', m_a; z_a; M_a; \eta, z)$$
$$\Phi_{\mathrm{e}}(m_*'|m_a, z_a, z)\, n_{\mathrm{sub}}(m_a, z_a|M, z)$$
$$P(M_a, z_a|M, z)\, P(\eta). \quad (18)$$

Here $n_{\mathrm{sub}}(m_a, z_a|M, z)$ is the SHMF described in Section 2.4; $\Phi_{\mathrm{e}}(m_*'|m_a, z_a, z)$ is the CSMF of galaxies that were accreted at redshift z_a, taking into account their subsequent mass evolution to the redshift z in question due to star formation and stellar evolution; $P(m_*|m_*', z_a; M_a; m_a; \eta, z)$ is the probability that a satellite galaxy whose stellar mass would be m_*' in the absence of stripping or disruption ends up with a stellar mass m_* at redshift z due to such environmwental effects. This last probability is written in a form that depends explicitly on the masses of the subhalo and host halo at the accretion epoch (m_a and M_a, respectively) as well as on the orbital circularity of the subhalo, η (to be defined below). Note that the integrand includes the probability distributions $P(\eta)$ and $P(M_a, z_a|M, z)$. The latter describes the probability that the main progenitor of a halo of mass M at redshift z has a mass M_a at redshift $z_a \geq z$; hence $P(M_a, z_a|M, z)$ describes the mass assembly history of the host halo. Note also that the integration over z_a implies that the CSMF of satellite galaxies at redshift z depends on the CSMF of centrals at all redshifts $z_a \geq z$. The orbital circularity is defined as $\eta \equiv j/j_{\mathrm{c}}(E)$ ($0 \leq \eta \leq 1$). Here j is the orbital specific angular momentum and $j_{\mathrm{c}}(E)$ is the specific angular momentum of a circular orbit that has the same orbital energy, E, as the orbit in question. Numerical simulations have show that the probability distribution of η of dark matter subhaloes is well approximated by

$$P(\eta) \propto \eta^{1.2}(1 - \eta)^{1.2}, \quad (19)$$

independent of redshift or halo mass (e.g., Zentner et al. 2005).

An important quantity that must somehow enter in a description of $P(m_*|m_*', m_a; z_a; M_a; \eta, z)$ is the dynamical friction time scale, t_{df}, defined as the time interval between the accretion of a subhalo and the epoch at which it is either tidally disrupted or cannibalized by the central galaxy. Using N-body simulations, Boylan-Kolchin et al. (2008) have shown that

$$\frac{t_{df}}{\tau_{dyn}} = 0.216 \frac{(M_a/m_a)^{1.3}}{\ln(1 + M_a/m_a)} \left[\frac{r_c(E)}{r_{vir}(z_a)} \right] e^{1.9\eta}, \quad (20)$$

which is the functional form we adopt throughout. Here $r_{vir}(z_a)$ is the virial radius of the host halo at z_a, and $\tau_{dyn} \approx 0.1 H^{-1}(z_a)$ is the dynamical time of the halo at z_a. As an approximation, we assume

$$r_c(E) = r_{vir}(z_a), \quad (21)$$

so that $t_{df} = t_{df}(m_a/M_a, z_a, \eta)$, and can thus be evaluated for the integrand in Eq. (18).

In this paper we assume that a galaxy after becoming a satellite can gain stellar mass due to star formation and suffer mass loss due to passive evolution. As a simple model, we assume the overall evolutionary effect can be modeled as a function of the masses $m_{*,z}$ and $m_{*,a}$, where $m_{*,z}$ is the expected median stellar mass of central galaxies in halos of mass m_a at redshift z. Specifically, we write the evolution of the median stellar mass of a satellite galaxy as

$$\overline{m}_*' = (1 - c)m_{*,a} + c m_{*,z}, \quad (22)$$

where c is a parameter which may depend on z. Thus, if $c = 0$, then $\overline{m}_*' = m_{*,a}$ so that the stellar mass of a satellite is equal to its original mass at accretion. On the other hand if $c = 1$, then $\overline{m}_*' = m_{*,z}$ so that the stellar mass of a satellite is the same as that of central galaxy of the same halo mass at the redshift, z, in question. The $c = 1$ case corresponds to the assumption adopted in the conventional abundance matching represented by equation (1). By treating c as a free parameter, we can examine how the evolution may deviate from the simplified assumptions. Given this assumption, we write

$$\Phi_e(m_*'|m_a, z_a, z) = \frac{1}{\sqrt{2\pi}\sigma_c'} \exp\left[-\frac{(\log m_*'/\overline{m}_*')^2}{2\sigma_c'^2} \right]. \quad (23)$$

As a simple model, we assume σ_c' to be the same as σ_c that specifies the CSMF of central galaxies (see Section 3.3). Thus, in the special case of $c = 0$, $\Phi_e(m_*'|m_a, z_a, z)$ has the same form as the CSMF of central galaxies at the accretion redshift z_a. In general, Φ_e is a lognormal distribution with a median $\overline{m}_*'$ and a dispersion given by σ_c.

For the stripping and disruption of the satellite galaxies, we adopt a simple form for $P(m_*|m_{*,evo}, z_a; m_a; M_a; \eta, z)$, assuming that significant tidal stripping occurs only for the dark matter subhalo, but not for the stellar component that represents the satellite galaxy, at least not until it is either destroyed by the tidal forces of, or cannibalized by, the central galaxy. In this case, we have that

$$P(m_*|m_*', z_a; m_a; M_a; \eta, z) =$$
$$\begin{cases} \delta^D(m_* - m_*') & \text{if } \Delta t < p_t \, t_{df} \\ 0 & \text{otherwise}. \end{cases} \quad (24)$$

Here

$$\Delta t \equiv t(z) - t(z_a), \quad (25)$$

is the time interval between z and z_a (i.e., the time since accretion). Thus we have two free parameters c and p_t that we seek to constrain using the observed satellite population. The parameter p_t is intended to account for the tidal stripping effect. The extreme case of $p_t = \infty$ corresponds to no tidal stripping/disruption of satellite galaxies, while the case of $p_t = 0$ corresponds to instantaneous disruption of all the satellite galaxies. Under the above assumptions, Eq. (18) reduces to

$$\Phi_s(m_*|M, z) = \int_0^M dm_a \int_z^\infty \frac{dz_a}{1 + z_a} \int_0^M dM_a \int_0^1 d\eta$$
$$\Phi_e(m_*|m_a, z_a, z) \, n_{sub}(m_a, z_a|M, z)$$
$$P(M_a, z_a|M, z) \, P(\eta) \, \Theta(p_t \, t_{df} - \Delta t), \quad (26)$$

with $\Theta(x)$ the Heaviside step function, which is straightforward to compute numerically.

For the ith-order sub-subhalos (note that we only consider $i = 1$), we assume that the dynamical friction time is also given by equation (20), but with M_a referring to the mass of the main branch of the (m_{i-1}, z_{i-1}) halo at the accretion time $z_a = z_i$. This dynamical friction time has to be compared with $\Delta t \equiv t(z_{i-1}) - t(z_i)$ to decide if the (m_i, z_i) halo and its central galaxy were disrupted already in the $(i-1)$th-order subhalo. Their subsequent disruption then follows that of the $(i-1)$th-order (here 0th-order) subhalos.

3.2. The Two-Point Correlation Function of Galaxies

In modeling the two-point correlation function (2PCF) of galaxies we follow the procedures outlined in Wang et al. (2004). In particular, we write the 2PCF as

$$\xi(r, z) = \xi_{1h}(r, z) + \xi_{2h}(r, z), \quad (27)$$

where ξ_{1h} represents the correlation due to pairs of galaxies within the same halo (the "1-halo" term), and ξ_{2h} describes the correlation due to galaxies that occupy different halos (the "2-halo" term).

In our model, we assume that the radial number density distribution of the satellite galaxies, $n_s(r|M, z)$ follows the same NFW profile as a dark matter halo of mass M at redshift z out to the virial radius, r_{vir}, defined as the radius inside of which the average density is Δ_{vir} times the critical density. To good approximation

$$\Delta_{vir} = 18\pi^2 + 60x - 32x^2 \quad (28)$$

with $x = \Omega_m(z) - 1$ (Bryan & Norman, 1998). Note that in reality, the distribution of satellite galaxies may not follow an exact NFW profile. However, as tested in Yang et al. (2004) by populating satellite galaxies according to the real mass distributions in dark matter halos, the change produced in the 2PCFs is quite small, less 20% on small scale in real space. For the *projected* 2PCFs which will be used in this work, the impact is even smaller, less tha 10%. Furthermore, our *projected* 2PCFs are to be estimated on scales larger than $0.1 \, h^{-1}$Mpc, where the results are not sensitive to the assumption on the concentration of galaxy distribution in dark matter halos (see

Yang et al. 2005). Thus the foible of using NFW profile is negligible in comparison to the uncertainties in the observational data and in the halo model itself. For convenience, in what follows we use the *normalized* number density distribution, $u_s(r|M,z) = n_s(r|M,z)/\langle N_s|M,z \rangle$, so that

$$4\pi \int_0^{r_{\rm vir}} u_s(r|M,z)\, r^2\, {\rm d}r = 1\,, \qquad (29)$$

where $r_{\rm vir} = r_{\rm vir}(M,z)$ is the virial radius of the halo of mass M at redshift z. The 1-halo term of the galaxy correlation function can then be written as

$$\xi_{1h}(r,z) = \frac{2}{\overline{n}_g^2(z)} \int_0^\infty n_h(M,z)\, \langle N_{\rm pair}|M,z \rangle$$
$$f(r|M,z)\, {\rm d}M\,, \qquad (30)$$

where $\langle N_{\rm pair}|M,z \rangle$ is the mean number of distinctive galaxy pairs in a halo of mass M at redshift z, $f(r|M,z)4\pi r^2 \Delta r$ is the fraction of those pairs that have separations in the range $r \pm \Delta r/2$, and $\overline{n}_g(z)$ is the mean number density of galaxies at redshift z, given by

$$\overline{n}_g(z) = \int_0^\infty n_h(M,z)\, \langle N|M,z \rangle\, {\rm d}M\,. \qquad (31)$$

For a given (M,z), the mean number of pairs as function of separation, $\langle N_{\rm pair}\rangle f(r)$, can be divided into contributions from central-satellite pairs and satellite-satellite pairs:

$$\langle N_{\rm pair}\rangle f(r) = \langle N_{\rm cs}\rangle u_s(r) + \langle N_{\rm ss}\rangle f_s(r)\,, \qquad (32)$$

where $f_s(r)$ is the satellite galaxy pair distribution function within a dark matter halo of mass M at redshift z:

$$f_s(r) = 2\pi \int_0^{r_{\rm vir}} u_s(s)\, s^2 ds \int_0^\pi u_s(|\mathbf{s}+\mathbf{r}|)\sin\theta\, d\theta\,, \quad (33)$$

with $|\mathbf{s}+\mathbf{r}| = (s^2 + r^2 + 2sr\cos\theta)^{1/2}$. The number of central-satellite pairs is

$$\langle N_{\rm cs}|M,z \rangle = \langle N_c|M,z \rangle\, \langle N_s|M,z \rangle\,. \qquad (34)$$

For the number of satellite-satellite pairs we assume that N_s follows Poisson statistics so that

$$\langle N_{\rm ss}|M,z \rangle = \langle N_s|M,z \rangle^2\,. \qquad (35)$$

The 2-halo term of the 2PCF for galaxies can be written as,

$$\xi_{2h}(r,z) = [f_{\rm exc}(r,z)]^2\, \xi_{\rm dm}(r,z)\,, \qquad (36)$$

where $\xi_{\rm dm}(r,z)$ is the non-linear 2PCF of dark matter particles at redshift z, which we obtain by Fourier Transforming the non-linear power spectrum of Smith et al. (2003), and

$$f_{\rm exc}(r,z) = \frac{1}{\overline{n}_g(z)} \int_0^\infty n_h(M,z)\, \langle N|M,z \rangle$$
$$b_h(M,z)\, U(r|M,z)\, {\rm d}M\,. \qquad (37)$$

Here we have taken into account the halo-halo exclusion effect, in that the 2-halo galaxy pair can not have an average distance smaller than $r_{\rm exc}(M,z)$:

$$U(r|M,z) = \begin{cases} 0 & \text{if } r < r_{\rm exc}(M,z) \\ 1 & \text{else}\,. \end{cases} \qquad (38)$$

As shown in Wang et al. (2004), this method of computing the 2PCFs is accurate at the few percent level as long as $r_{\rm exc}(M,z) = 2r_{\rm vir}(M,z)$, which is the value we adopt throughout.

Observationally, the direct measurement is not the real-space 2PCF because of redshift space distortions. Instead one measures the projected 2PCF, $w_p(r_p)$, which is related to the real space 2PCF as

$$w_p(r_p) = 2 \int_0^\infty \xi\left(\sqrt{r_\pi^2 + r_p^2}\right)\, {\rm d}r_\pi\,, \qquad (39)$$

where the comoving distance has been decomposed into components parallel (r_π) and perpendicular (r_p) to the line of sight. In practice, the integration is only performed over a finite range of r_π. Following Wang et al. (2007), we use a maximum integration limit of $r_{\pi,\max} = 40\, h^{-1}{\rm Mpc}$ (see Appendix A).

3.3. *Redshift Dependence*

The formalism described above allows us to model the stellar mass functions and correlation function of galaxies once a set of parameters is adopted to specify the CSMF, $\Phi_c(M_*|M,z)$, and the dynamical evolution function, $P(m_*|m_{*,a}, z_a; m_a; M_a; \eta, z)$. At any particular redshift, our model for these quantities is fully described by the following seven free parameters: $M_{*,0}$, M_1, α, β, σ_c, p_t and c. In order to describe the evolution of the galaxy distribution over cosmic time, we need to specify how each of these parameters changes with redshift.

Throughout this paper we assume the following redshift dependence for our model parameters:

$$\begin{aligned} \log[M_{*,0}(z)] &= \log(M_{*,0}) + \gamma_1 z \\ \log[M_1(z)] &= \log(M_1) + \gamma_2 z \\ \alpha(z) &= \alpha + \gamma_3 z \\ \log[\beta(z)] &= \min[\log(\beta) + \gamma_4 z + \gamma_5 z^2, 2] \quad (40) \\ \sigma_c(z) &= \max[0.173, 0.2z] \\ p_t(z) &= p_t \\ c(z) &= c\,. \end{aligned}$$

These functional forms have been obtained using trial-and-error whereby we tried to minimize the number of parameters while achieving a good fit to the overall data (see Section 4 below). As we have tested and as pointed out in Moster et al. (2010), $\sigma_c(z)$ cannot be well constrained by the SMFs alone. The form adopted above for $\sigma_c(z)$ is based on the amount of true scatter at low redshift obtained by Y09 and the uncertainty in the stellar mass measurements at high redshifts (e.g., D05; see also Conroy et al. 2009). Note that the redshift dependence is relevant only at high redshift when σ_c is dominated by the uncertainty in the stellar mass measurements, and so we use $\sigma_c(z)$, instead of $\sigma_c(z_a)$, for σ_c in Eq. 26. The model is thus specified by a total of 11 free parameters, four to describe the CSMF at $z = 0$, five to describe their evolution with redshift, and two (c and p_t) to describe the evolution of satellite galaxies. Note that we assume that both c and p_t are independent of redshift. As we demonstrate below, this assumption is perfectly compatible with current data. However, it is very simplified and needs to be re-evaluated once better data becomes available.

4. OBSERVATIONAL CONSTRAINTS

The goal of this paper is to constrain the CSMF, $\Phi_c(M_*|M, z)$, and the dynamical evolution function, $P(m_*|m_{*,a}, z_a; m_a; M_a; \eta, z)$, and in particular their evolution with redshift, using observational data. In this section we summarize the observational data to be used to constrain our model. All our low redshift data are obtained from the SDSS DR7 (Abazajian et al. 2009).

4.1. Low-Redshift Data
4.1.1. The Total Stellar Mass Function

For the low redshift stellar mass function (SMF) we use the results that are obtained using the same method outlined in Y09b, but here updated to the SDSS DR7 (Abazajian et al. 2009). Note that in these measurements the galaxy stellar masses are estimated using the model of Bell et al. (2003) in which a Kroupa (2001) IMF was adopted (Borch et al. 2006). The resulting SMFs, for galaxies of different colors and of different group member types, are provided in Appendix B for reference. Here for our purpose, we only use the SMF of all galaxies, which is shown in the upper panel of Fig. 2 as open circles with error bars. For comparison, the solid and dashed lines show the best Schechter fits for the SMFs of our measurements and the one obtained by Panter et al. (2007) from the SDSS DR3 (Abazajian et al. 2005), respectively. The open squares correspond to the SMF obtained by Li & White (2009) from the SDSS DR7 as well but for stellar masses obtained by Blanton & Roweis (2007). To have a clearer vision of the difference between these measurements, we show in the lower panel of Fig. 2 the ratio of the SMFs which are normalized by our best fit Schechter form SMF. There are $\sim$ 50% and $\sim$ 20% difference at the high and low mass ends between these three SMFs, which most likely arise from differences in (i) the methods used to derive the stellar masses and (ii) the different data releases used. As pointed out in Li & White (2009), srarting from similar IMF, the systematic difference of stellar masses obtained by different approaches are at 0.1dex to 0.3dex at high to low mass ends. For the systematic errors, it is very difficult to come up with a realistic covariance model for the stellar mass function, as it is not clear the uncertainties in the assumed IMF and spectral synthesis model. In the simplest assumption, the covariance can be a constant shift in the stellar mass, where our results can be scaled to other IMFs and spectral synthesis models. Here, for simplicity, to mimic such kind of systematics, we assume there is at least 20% error on each data point of our SMF.

4.1.2. The conditional stellar mass function

In addition to the (global) SMF, we also use the conditional stellar mass function (CSMF) to constrain our model. The CSMFs have been obtained by Y09b from the SDSS DR4 group catalogues constructed by Yang et al. (2007) using the halo-based group finder of Yang et al. (2005a). Here we update the CSMFs using the latest SDSS DR7 group catalogues[4]. The halo masses provided in the group catalogues are obtained using the halo-abundance matching method (see Section 4.1 in Yang et

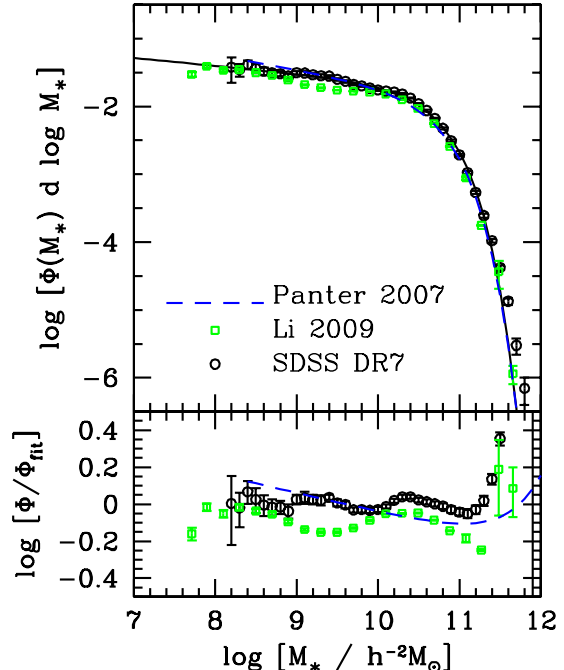[4] see *http://gax.shao.ac.cn/data/Group.html*

FIG. 2.— Upper panel: the stellar mass function (SMF) of galaxies at low redshifts ($z \sim 0.1$). Open circles with errorbars are the results we obtained from the SDSS DR7, and the solid line is the corresponding best-fit Schechter form. For comparison, the dashed line shows the best-fit of the SMF obtained by Panter et al. (2007), and the squares with errorbars are the results obtained by Li & White (2009). Lower panel: similar to the upper panel, but here for the ratios between the SMFs and our best-fit Schechter form.

al. 2007) where halo mass function for the WMAP7 cosmology is used. The results of the CSMFs are provided in Appendix B for reference.

4.1.3. The two-point correlation function

We have measured the projected 2PCFs for SDSS DR7 galaxies of different stellar masses, estimated using the model of Bell et al. (2003), i.e., these are the same stellar mass estimates as used for our SMF and CSMF. A detailed description of how we obtained these 2PCFs can be found in Appendix A. We note that similar measurements have already been carried out by Li et al. (2006) using data from the SDSS DR2 with stellar masses as given by Kauffmann et al. (2003). As we have tested, our results agree with those obtained by Li et al. (2006) at 1-σ level. Here we make use of our own measurements with full covariance matrixes to constrain the CSMFs.

4.2. High-Redshift Data

In addition to the low-redshift data discussed above, we also use data at high redshifts. Numerous studies have measured SMFs at high redshifts using different data sets. Unfortunately, differences among the SMFs obtained by different authors are still quite large. In this paper we therefore use two different sets of data, and use the differences in the resulting models as a method to gauge the model uncertainties arising from the uncertainties in the data.

The first data set that we use are the SMFs of Perez-Gonzalez et al. (2008, hereafter PG08) obtained from Spitzer data for galaxies in the redshift range from
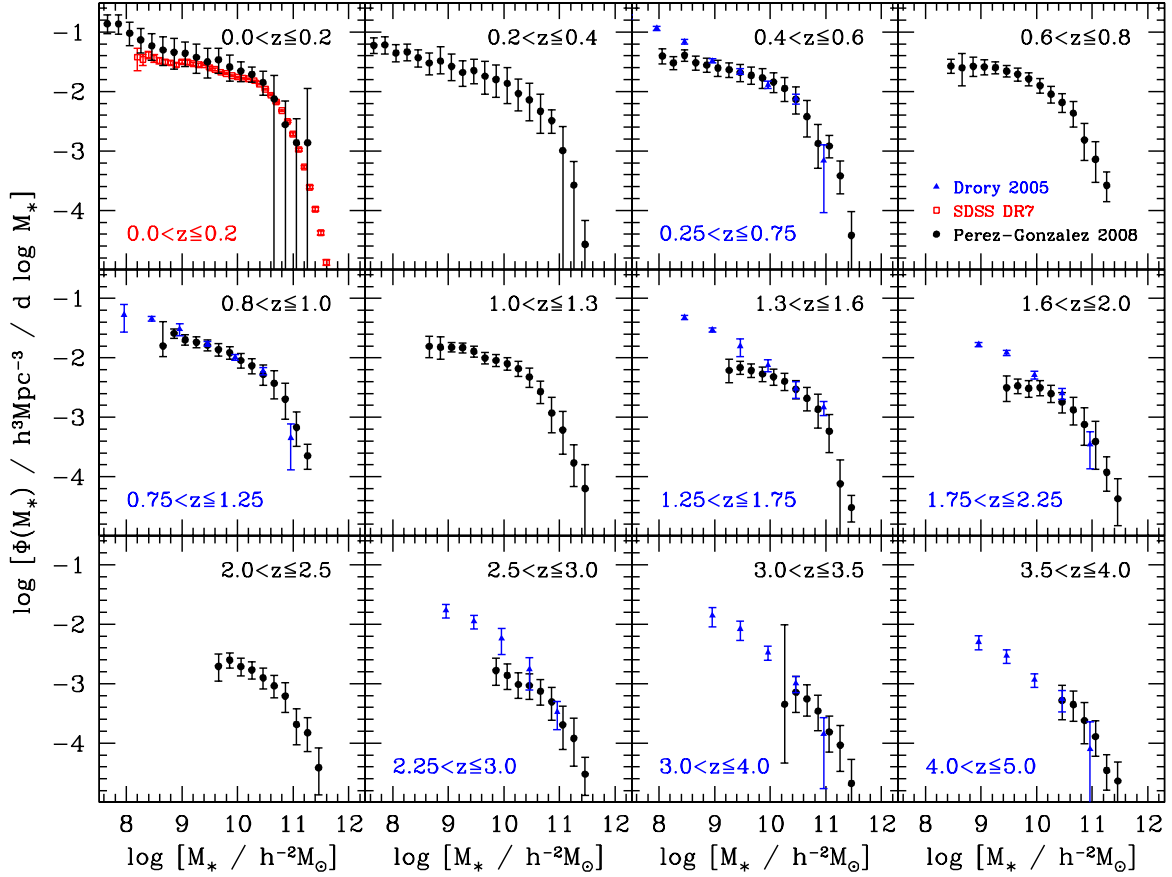
FIG. 3.— The stellar mass functions of galaxies in different redshift bins as indicated in each panel. The filled circles with error-bars are results obtained from the Spitzer observation by Perez-Gonzalez et al. (2008, PG08). The open squares with error-bars are results obtained in this work from the SDSS DR7. The filled triangles with error-bars are results obtained by Drory et al. (2005, D05), for which we have combined their data for FORS Deep and the GOODS/CDF-S Fields. The redshift range labeled in the upper right-hand corner of each panel is for the results of PG08, while the range labeled in the lower left-hand corner is for the results obtained from SDSS DR7 (first panel) and D05 (other panels). Here the stellar masses of PG08 and D05 are divided by a factor of 1.7 to take account the systematic differences of using different IMFs.

$0 \lesssim z \lesssim 4$. Note that in their study, PG08 assumed a Salpeter (1955) IMF which is different from the Kroupa IMF used in the local universe for the SDSS stellar masses. As suggested in PG08, the stellar masses based on the Salpeter (1955) IMF are systematically larger by a factor of ~ 1.7 than that based on the Kroupa IMF. For consistency, we therefore devide all the stellar masses provided in PG08 by this factor. The resulting data are shown as solid dots with errorbars in Fig. 3. For comparison, the open squares in the upper left-hand panel correspond to the local SMF obtained from the SDSS DR7 in this study. Note that the latter is in general consistent with that of PG08 except at low mass end, which we believe to be a result of cosmic variance and/or the stellar mass estimator. In what follows we therefore ignore the SMF of PG08 for the $0 < z \leq 0.2$ redshift bin.

The second data set for high redshift SMFs is that of Drory et al. (2005; hereafter D05), which is based on deep multicolor data in the FORS Deep Field and the Great Observatories Origins Deep Survey-South/Chandra Deep Field-South (GOODS/CDF-S) region. For our investigation, we combine the two separate measurements of these two regions, taking their average and using the maximum of their original error and the difference between the two as the new error. For the few data points for which only FORS Deep Field data is available, we update their errors using the percentage errors of the nearest data points to partly take account of systematic errors. Again, the stellar masses obtained in D05 assumed a Salpeter (1955) IMF, and we divide the stellar masses by a factor of ~ 1.7 to correct them to the Kroupa IMF. The resulting data are shown in Fig. 3 as filled triangles with errorbars. Note that there is large discrepancy between the PG08 and the D05 results, especially at high redshift. Since it is difficult to decide which result is more reliable, we will perform two separate analyses using either of these data sets. Finally, as we did for the low-redshift data, we also assume a minimum of 20% error for each data point of the SMFs to account for other possible uncertainties in the data.

Two-point correlation functions for galaxies of different stellar mass bins are available at intermediate redshifts (e.g., Meneux et al. 2008 using VVDS; Meneux et al. 2009 using zCOSMOS). However, as pointed out in Meneux et al. (2009), because of the small sky coverage of the surveys, these measurements suffer significantly from cosmic variance. We therefore decided not to use these measurements to constrain our model. Instead we shall only use them for comparison with our model predictions.

Model	Data constraint	c	p_t
FIT0	SMF	-	0
FIT1	SMF	1	∞
FIT-2PCF	SMF+2PCF	free	free
FIT-CSMF	SMF+CSMF	free	free
SMF1	SMF=SDSS DR7+PG08		
SMF2	SMF=SDSS DR7+D05		

NOTE. — SDSS DR7: the stellar mass function at $z = 0.1$ we obtained from SDSS DR7 using the method of Yang et al. (2009b); PG08: the stellar mass functions obtained by Perez-Gonzalez et al. (2008) from Spitzer, excluding the data at $z = 0.1$; D05: the combined stellar mass functions obtained by Drory et al. (2005) using deep multicolor data in the FORS Deep Field and the GOODS/CDF-S region.

4.3. The Fitting Method

To constrain model parameters using observational data, we use a Monte-Carlo Markov Chain (hereafter MCMC) to explore the likelihood function in the multi-dimensional parameter space (see Yan, Madgwick & White 2003 and van den Bosch et al. 2005b for similar analyses). In order to check whether different data sets are mutually compatible, we carry out two different analyses. The first one, referred to as FIT-2PCF, uses the SMFs together with the 2PCFs $[w_p(r_p)]$ of galaxies at low-z. The second, referred to as FIT-CSMF, uses the SMFs at different redshifts together with the CSMFs at low z as constraints. The corresponding χ^2 are defined as

$$\chi^2_{2PCF} = \chi^2(\Phi) + \chi^2(w_p),\qquad(41)$$

and

$$\chi^2_{CSMF} = \chi^2(\Phi) + \chi^2(\Phi_{CSMF}),\qquad(42)$$

respectively. Here $\chi^2(\Phi)$, $\chi^2(w_p)$, $\chi^2(\Phi_{CSMF})$ are given by

$$\chi^2(\Phi) = \sum_{i=1}^{N_z}\sum_j \left[\frac{\Phi_{mod}(M_{*,j},z_i) - \Phi_{obs}(M_{*,j},z_i)}{\sigma_\Phi(M_{*,j},z_i)}\right]^2,\qquad(43)$$

and

$$\chi^2(w_p) = \sum_{i=1}^{N_w}\sum_{j,k} \Delta w_{p,j}(\mathbf{C}^{-1})_{j,k}\Delta w_{p,k},\qquad(44)$$

with

$$\Delta w_{p,j} = w_{p,mod}(r_{p,j}|M_{*,i}) - w_{p,obs}(r_{p,j}|M_{*,i}),\qquad(45)$$

and

$$\chi^2(\Phi_{CSMF}) =\qquad(46)$$
$$\frac{1}{N_C}\sum_{i=1}^{N_C}\sum_j \left[\frac{\Phi_{mod}(M_{*,j}|M_i) - \Phi_{obs}(M_{*,j}|M_i)}{\sigma_{CSMF}(M_{*,j}|M_i)}\right]^2.$$

In the above expressions, $\sigma_\Phi(M_{*,j},z_i)$, and $\sigma_{CSMF}(M_{*,j}|M_i)$ are, respectively, the observational errors for the SMF and CSMF, while $(\mathbf{C}^{-1})_{j,k}$ is the inverse of the covariance matrix of the observed projected 2PCF. The integers N_z, N_w and N_C are the number of SMFs (for different redshifts), the number of projected 2PCFs (for different stellar mass bins), and the number of CSMFs (for different halo mass bins), respectively. The factor $1/N_C$ in Eq. (46) is somewhat arbitrary, which is included to reduce the weight of the CSMFs, as both the CSMFs and the low-z SMF are based on the same data and thus not completely independent.

In addition to FIT-2PCF and FIT-CSMF, in which all eleven parameters are included in the fitting, and both the SMFs and 2PCFs (or CSMFs) are used as constraints, we also consider two extreme cases where p_t is assumed to be either 0 or ∞. The first case (referred to as FIT0 in the following) with $p_t = 0$ effectively assumes that all satellite galaxies are stripped as soon as they are accreted (i.e., there are no satellite galaxies). The second case (referred to as FIT1) assumes $p_t = \infty$ and $c = 1$, so that a satellite is never disrupted and evolves in such a way that, at the redshift z in question, it has the same stellar mass as a central galaxy in a host halo with mass equal to the halo mass of the satellite at its accretion time. In these two extreme cases we only use the SMFs at different redshifts as constraints. These extreme cases are used to gauge the importance of the satellite population in our modeling (see also Yang et al. 2009a; Wang & Jing 2010).

As mentioned above, there are large differences between the SMFs obtained by PG08 and D05 at high redshifts, and we therefore will use them separately to constrain our model. More specifically, we consider two sets of models. The first uses the high-z SMFs of PG08 and is refered to as SMF1; the second uses the high-z SMFs of D05 and referred to as SMF2. For reference, Table 2 lists all our different models, including the abbreviations that we use to refer to them.

We start our MCMC from an initial guess and allow a 'burn-in' of 1,000 steps for the chain to equilibrate in the likelihood space. At any point in the chain we generate a new set of model parameters by drawing the shifts in the eleven free parameters from eleven independent Gaussian distributions. The Gaussian widths are tuned so that the average accepting rate for the new trial model is about 0.25. The probability of accepting the trial model is

$$P_{accept} = \begin{cases} 1.0 & \text{if } \chi^2_{new} < \chi^2_{old} \\ \exp[-(\chi^2_{new} - \chi^2_{old})/2] & \text{if } \chi^2_{new} \geq \chi^2_{old} \end{cases}\qquad(47)$$

with the χ^2 defined in Eq. (41) or in Eq. (42).

We construct a MCMC of 500,000 steps after 'burn-in', with an average acceptance rate of ~ 25 percent. Before the further treatment of the MCMC, we have tested its convergence using the 'convergence ratio' r as defined in Dunkley et al. (2005). In all cases in consideration, we observe $r < 0.01$ is achieved for each parameter. In order to suppress the correlation between neighboring models in the chain, we thin the chain by a factor 50. This results in a final MCMC consisting of 10,000 independent models that sample the posterior distribution. As an illustration, we show in Fig. 4 the flowchart of our fiting process. Based on these 10,000 independent models, we obtain the best parameter set that has the smallest χ^2. The 68% confidence level (CL) around this set of model is obtained by simply sorting the models according to their χ^2, and finding models that have χ^2 values smaller than that corresponding to the 68% CL. As an illustration, the outer to inner contours in Fig. 5 plot the projected
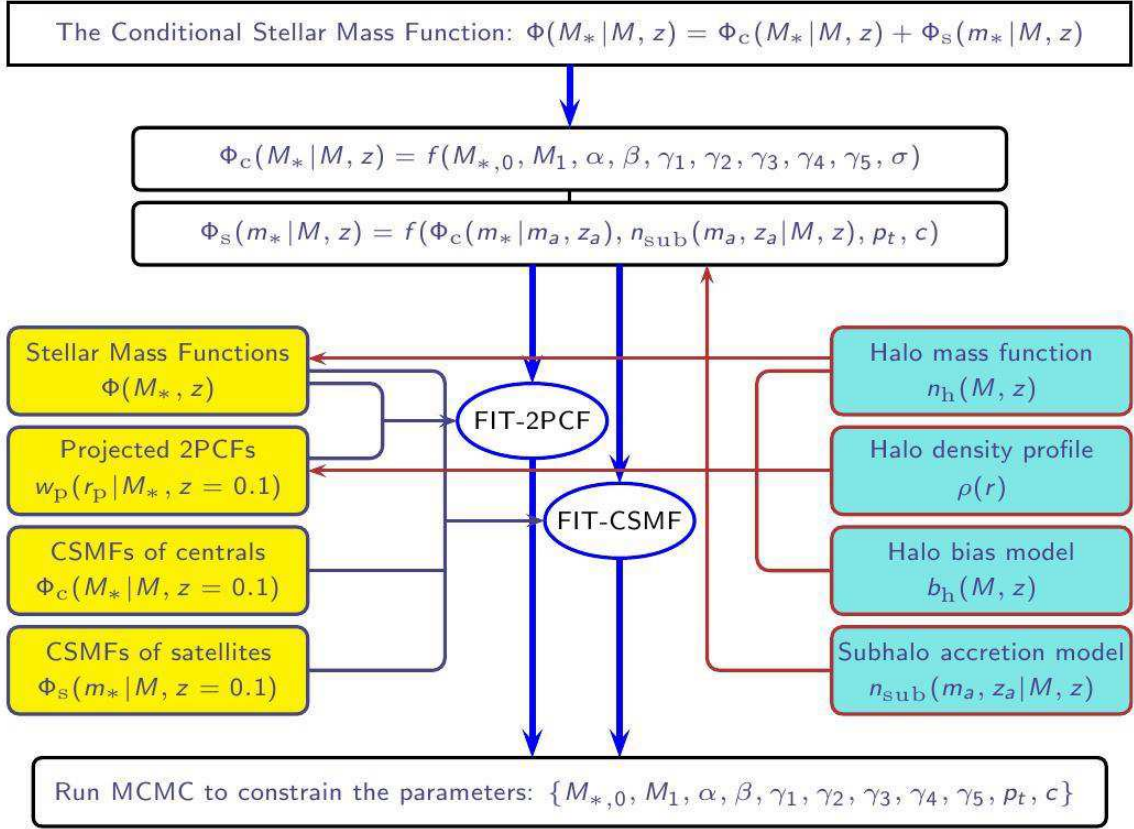
The Conditional Stellar Mass Function: $\Phi(M_*|M, z) = \Phi_c(M_*|M, z) + \Phi_s(m_*|M, z)$

$\Phi_c(M_*|M, z) = f(M_{*,0}, M_1, \alpha, \beta, \gamma_1, \gamma_2, \gamma_3, \gamma_4, \gamma_5, \sigma)$

$\Phi_s(m_*|M, z) = f(\Phi_c(m_*|m_a, z_a), n_{\rm sub}(m_a, z_a|M, z), p_t, c)$

Stellar Mass Functions $\Phi(M_*, z)$

Projected 2PCFs $w_{\rm p}(r_{\rm p}|M_*, z = 0.1)$

CSMFs of centrals $\Phi_c(M_*|M, z = 0.1)$

CSMFs of satellites $\Phi_s(m_*|M, z = 0.1)$

FIT-2PCF

FIT-CSMF

Halo mass function $n_{\rm h}(M, z)$

Halo density profile $\rho(r)$

Halo bias model $b_{\rm h}(M, z)$

Subhalo accretion model $n_{\rm sub}(m_a, z_a|M, z)$

Run MCMC to constrain the parameters: $\{M_{*,0}, M_1, \alpha, \beta, \gamma_1, \gamma_2, \gamma_3, \gamma_4, \gamma_5, p_t, c\}$

FIG. 4.— A flowchart showing how we constrain the paramenters of CSMFs. The filled bars on the left-hand side list the observational quantities used as constraints, while those on the right-hand side list the ingredients to model these quantities. We use MCMC to obtain both the best fit parameters and their confidence ranges. The MCMC analysis is performed separately for both FIT-2PCF and FIT-CSMF.

2-D boundaries in the parameter space that enclose 95%, 68%, 30%, 10% and 1% of the models with the smallest χ^2 values, with the best-fit values indicated by a cross. The marginalized 1-D distribution of each parameter obtained from all the 10,000 models is also shown in the plot. As one can see, strong covariance exists in some parameter pairs, such as β and M_1, γ_1 and γ_3, and γ_4 and γ_5. Overall, most parameters are well constrained, with their mean values much larger than the corresponding dispersions. For reference we list in Tables 3 and 4 the best-fit parameters together with their 68% CLs. IDs 1 to 4 correspond to FIT0, FIT1, FIT-2PCF and FIT-CSMF, respectively, all assuming WMAP7 cosmology. Results are listed separately for cases using SMF1 and SMF2. For the other four cosmological models listed in Table 1 we only give the best-fit parameters and their 68% CLs for FIT-CSMF and FIT-2PCF models (IDs 5-12). The details of all these models are discussed in the following section.

5. RESULTS

The upper left-hand panels of Figs. 6 and 7 show the fits to the observed SMFs at low-z using SMF1 and SMF2, respectively. In both cases we adopted the fiducial WMAP7 cosmology. The long-dashed and dotted lines show the results for the two extreme models, FIT0 and FIT1, respectively. Clearly, even these two extreme models can accurately match the observed SMFs (as judged by their reduced χ^2 values), indicating that the SMFs alone cannot constrain the values of p_t and c. This is ex-

pected from the fact that, as mentioned above, the SMFs are dominated by central galaxies. Note that for SMF2, the $\chi^2(\Phi)$ values are significantly larger than those for SMF1. The main reason for this is the much smaller error bars in SMF2 and the large difference between model and data at the low mass end for the $0.25 < z < 0.75$ redshift bin (see the second panel of Fig. 7).

The best fit parameters of the FIT0 and FIT1 models are used to make predictions for the projected two-point correlation functions, $w_{\rm p}(r_{\rm p})$, in different stellar mass bins, and the results are shown in Fig. 8 (for SMF1) and Fig. 9 (for SMF2), again as long-dashed and dotted lines, respectively. Clearly, the model predictions for FIT0 and FIT1 are very different, especially on small scales where the correlation function is dominated by the 1-halo term. Since FIT0 and FIT1 represent the minimum and maximum contributions of satellite galaxies, respectively, the correlation functions predicted by these two models should bracket the predictions of more realistic models. The large difference between FIT0 and FIT1 clearly demonstrates that the observed $w_{\rm p}(r_{\rm p})$, *especially for* $r_{\rm p} \lesssim 1\,h^{-1}{\rm Mpc}$, can provide useful constraints on the satellite population, which in our model is characterized by the parameters p_t and c. Note that the observed $w_{\rm p}(r_{\rm p})$ falls nicely between the predictions for our two extreme models, suggesting that a more realistic treatment of satellite galaxies should be able to fit the data.

When separated into central and satellite components, the CSMF, $\Phi(M_*|M)$, provides direct information re-

TABLE 3
THE BEST FIT PARAMETERS OF THE CSMF BASED ON SMF1.

ID	cosmology	$\log M_{*,0}$	$\log M_1$	α	β	γ_1	γ_2	γ_3	γ_4	γ_5	p_t	c	χ^2	FIT-type
(1)	(2)	(3)	(4)	(5)	(6)	(7)	(8)	(9)	(10)	(11)	(12)	(13)	(14)	(15)
1	WMAP7	$10.21^{+0.09}_{-0.10}$	$10.73^{+0.15}_{-0.19}$	$0.30^{+0.02}_{-0.02}$	$5.54^{+1.95}_{-1.10}$	$-0.67^{+0.22}_{-0.20}$	$-0.27^{+0.07}_{-0.06}$	$0.19^{+0.07}_{-0.08}$	$0.14^{+0.13}_{-0.15}$	$0.25^{+0.10}_{-0.08}$	0	$-$	35.10	FIT0
2		$10.12^{+0.10}_{-0.11}$	$10.82^{+0.16}_{-0.16}$	$0.33^{+0.02}_{-0.02}$	$9.40^{+2.66}_{-2.31}$	$-0.51^{+0.18}_{-0.26}$	$-0.27^{+0.06}_{-0.06}$	$0.15^{+0.10}_{-0.07}$	$-0.03^{+0.12}_{-0.14}$	$0.28^{+0.08}_{-0.08}$	∞	1.00	38.91	FIT1
3		$10.25^{+0.03}_{-0.05}$	$10.73^{+0.06}_{-0.05}$	$0.28^{+0.02}_{-0.01}$	$8.19^{+0.49}_{-0.59}$	$-0.65^{+0.15}_{-0.18}$	$-0.26^{+0.03}_{-0.05}$	$0.19^{+0.07}_{-0.05}$	$-0.09^{+0.09}_{-0.13}$	$0.33^{+0.09}_{-0.06}$	$1.31^{+0.23}_{-0.15}$	$0.64^{+0.24}_{-0.58}$	113.33	FIT-2PCF
4		$10.19^{+0.08}_{-0.06}$	$10.69^{+0.20}_{-0.11}$	$0.29^{+0.01}_{-0.02}$	$8.15^{+1.91}_{-2.33}$	$-0.62^{+0.20}_{-0.19}$	$-0.24^{+0.05}_{-0.07}$	$0.18^{+0.07}_{-0.08}$	$-0.07^{+0.15}_{-0.12}$	$0.33^{+0.10}_{-0.09}$	$0.82^{+0.10}_{-0.08}$	$0.73^{+0.23}_{-0.24}$	102.09	FIT-CSMF
5	WMAP1	$10.23^{+0.04}_{-0.07}$	$10.84^{+0.02}_{-0.14}$	$0.29^{+0.01}_{-0.01}$	$7.11^{+1.64}_{-0.25}$	$-0.62^{+0.16}_{-0.16}$	$-0.23^{+0.05}_{-0.04}$	$0.18^{+0.06}_{-0.06}$	$-0.12^{+0.10}_{-0.12}$	$0.35^{+0.07}_{-0.07}$	$1.12^{+0.16}_{-0.29}$	$0.47^{+0.53}_{-0.23}$	107.07	FIT-2PCF
6		$10.22^{+0.03}_{-0.07}$	$10.78^{+0.03}_{-0.10}$	$0.28^{+0.01}_{-0.01}$	$7.66^{+1.51}_{-0.11}$	$-0.59^{+0.14}_{-0.16}$	$-0.22^{+0.06}_{-0.05}$	$0.17^{+0.07}_{-0.05}$	$-0.14^{+0.14}_{-0.08}$	$0.38^{+0.06}_{-0.10}$	$0.95^{+0.10}_{-0.10}$	$0.29^{+0.19}_{-0.15}$	103.77	FIT-CSMF
7	WMAP3	$10.27^{+0.06}_{-0.03}$	$10.72^{+0.09}_{-0.09}$	$0.29^{+0.02}_{-0.01}$	$7.39^{+1.20}_{-0.81}$	$-0.63^{+0.18}_{-0.13}$	$-0.29^{+0.05}_{-0.04}$	$0.19^{+0.07}_{-0.07}$	$0.05^{+0.10}_{-0.11}$	$0.27^{+0.07}_{-0.06}$	$1.27^{+0.44}_{-0.20}$	$0.94^{+0.06}_{-0.38}$	151.37	FIT-2PCF
8		$10.21^{+0.04}_{-0.04}$	$10.64^{+0.08}_{-0.05}$	$0.29^{+0.01}_{-0.01}$	$7.60^{+0.59}_{-0.88}$	$-0.62^{+0.20}_{-0.15}$	$-0.27^{+0.04}_{-0.04}$	$0.19^{+0.04}_{-0.08}$	$0.10^{+0.11}_{-0.08}$	$0.25^{+0.06}_{-0.07}$	$0.77^{+0.08}_{-0.06}$	$0.97^{+0.03}_{-0.13}$	100.64	FIT-CSMF
9	WMAP5	$10.22^{+0.05}_{-0.06}$	$10.70^{+0.06}_{-0.09}$	$0.29^{+0.01}_{-0.01}$	$8.18^{+1.04}_{-0.68}$	$-0.59^{+0.14}_{-0.18}$	$-0.25^{+0.04}_{-0.05}$	$0.18^{+0.06}_{-0.06}$	$-0.01^{+0.11}_{-0.10}$	$0.29^{+0.07}_{-0.07}$	$1.16^{+0.20}_{-0.12}$	$0.95^{+0.05}_{-0.51}$	120.92	FIT-2PCF
10		$10.22^{+0.03}_{-0.06}$	$10.73^{+0.05}_{-0.07}$	$0.29^{+0.02}_{-0.01}$	$7.05^{+0.89}_{-0.57}$	$-0.60^{+0.20}_{-0.16}$	$-0.26^{+0.05}_{-0.04}$	$0.18^{+0.06}_{-0.08}$	$0.03^{+0.08}_{-0.11}$	$0.28^{+0.07}_{-0.06}$	$0.83^{+0.08}_{-0.08}$	$0.60^{+0.18}_{-0.21}$	106.20	FIT-CSMF
11	Millennium	$10.27^{+0.04}_{-0.05}$	$10.74^{+0.08}_{-0.10}$	$0.27^{+0.02}_{-0.01}$	$7.16^{+1.31}_{-0.80}$	$-0.67^{+0.22}_{-0.11}$	$-0.23^{+0.06}_{-0.05}$	$0.20^{+0.04}_{-0.08}$	$-0.02^{+0.13}_{-0.10}$	$0.31^{+0.06}_{-0.08}$	$0.94^{+0.43}_{-0.07}$	$0.97^{+0.03}_{-0.74}$	98.43	FIT-2PCF
12		$10.22^{+0.05}_{-0.06}$	$10.70^{+0.10}_{-0.08}$	$0.28^{+0.02}_{-0.01}$	$7.25^{+0.94}_{-1.14}$	$-0.57^{+0.16}_{-0.18}$	$-0.21^{+0.04}_{-0.06}$	$0.16^{+0.06}_{-0.06}$	$0.01^{+0.13}_{-0.08}$	$0.30^{+0.05}_{-0.07}$	$1.00^{+0.10}_{-0.08}$	$0.35^{+0.16}_{-0.13}$	98.28	FIT-CSMF

NOTE. — Column (1): model ID. Column (2): cosmology used for fitting. Column (3-13): the best fit parameters for the CSMF. Note that $M_{*,0}$ is in units of $h^{-2}M_\odot$ and M_1 in units of $h^{-1}M_\odot$, and log is the 10 based logarithm. Column (14): the χ^2 defined in Eq.(41) or (42). Column (15): the type of FIT used to constrain the models. Here results are obtained by using SMF1 .
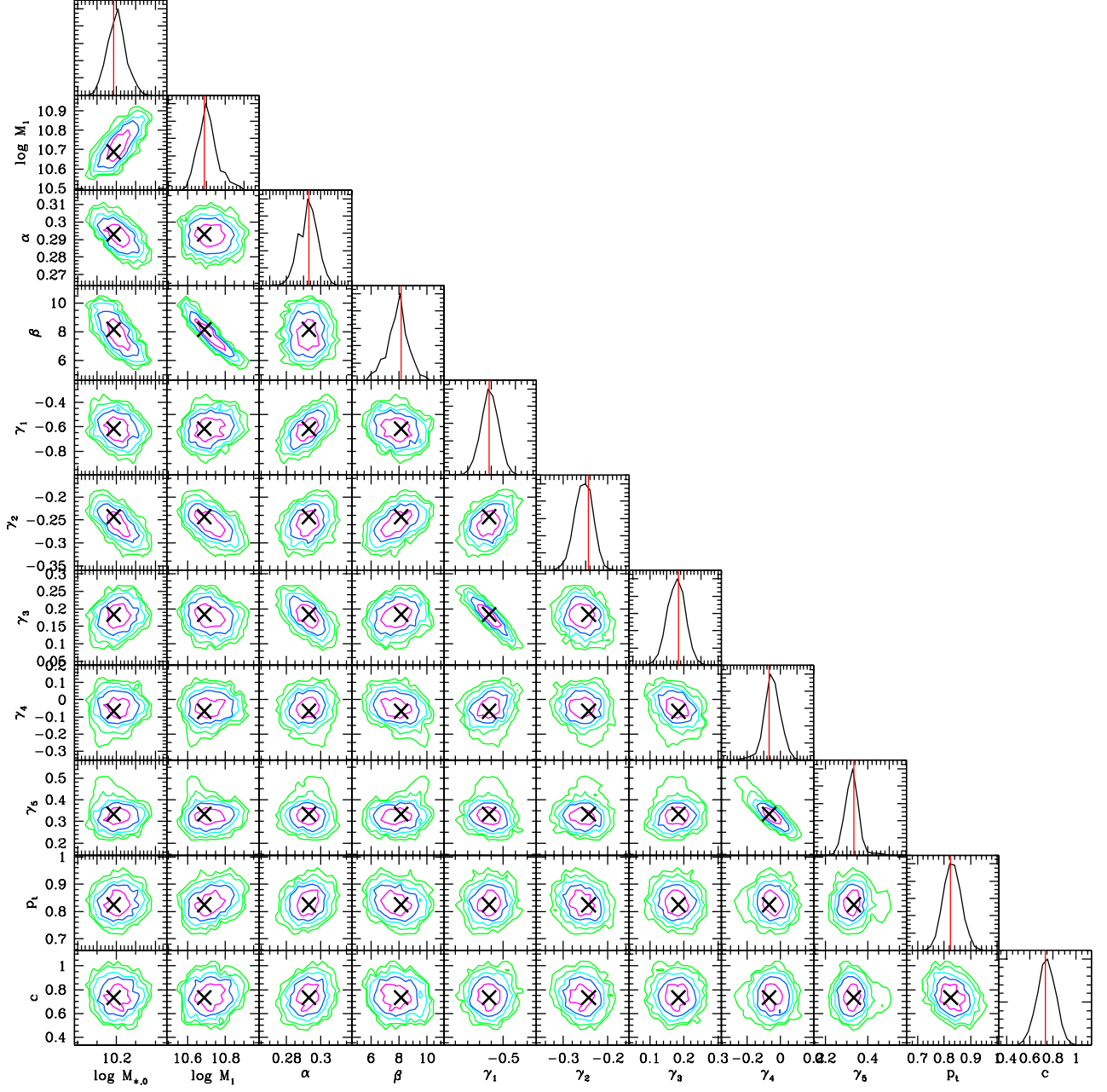
FIG. 5.— The best fit (cross or vertical line) and the projected distribution of the parameters in 2-D or 1-D space. The outer to inner contours in the 2-D plane correspond to the boundaries that enclose 95%, 68%, 30%, 10% and 1% models with the smallest χ^2 values, respectively. The 1-D distributions are the marginalized distributions of individual parameters obtained from all $10,000$ models.

TABLE 4
THE BEST FIT PARAMETERS FOR THE CSMFs BASED ON SMF2.

ID	cosmology	$\log M_{*,0}$	$\log M_1$	α	β	γ_1	γ_2	γ_3	γ_4	γ_5	p_t	c	χ^2	FIT-type
(1)	(2)	(3)	(4)	(5)	(6)	(7)	(8)	(9)	(10)	(11)	(12)	(13)	(14)	(15)
1	WMAP7	$10.45^{+0.07}_{-0.11}$	$11.17^{+0.11}_{-0.19}$	$0.25^{+0.03}_{-0.02}$	$3.23^{+0.78}_{-0.37}$	$-0.98^{+0.22}_{-0.18}$	$-0.25^{+0.07}_{-0.05}$	$0.42^{+0.09}_{-0.11}$	$-0.07^{+0.13}_{-0.09}$	$0.01^{+0.05}_{-0.01}$	0	$-$	56.03	FIT0
2		$10.45^{+0.08}_{-0.11}$	$11.43^{+0.15}_{-0.18}$	$0.27^{+0.03}_{-0.02}$	$3.85^{+0.92}_{-0.65}$	$-0.79^{+0.23}_{-0.19}$	$-0.24^{+0.10}_{-0.08}$	$0.38^{+0.10}_{-0.12}$	$-0.16^{+0.09}_{-0.09}$	$0.02^{+0.04}_{-0.02}$	∞	1.00	52.91	FIT1
3		$10.46^{+0.08}_{-0.04}$	$11.21^{+0.14}_{-0.09}$	$0.25^{+0.01}_{-0.03}$	$4.00^{+0.54}_{-0.64}$	$-0.93^{+0.14}_{-0.18}$	$-0.26^{+0.07}_{-0.03}$	$0.39^{+0.11}_{-0.05}$	$-0.15^{+0.07}_{-0.12}$	$0.04^{+0.02}_{-0.07}$	$1.18^{+0.21}_{-0.23}$	$0.91^{+0.09}_{-0.48}$	128.54	FIT-2PCF
4		$10.36^{+0.05}_{-0.06}$	$11.06^{+0.08}_{-0.15}$	$0.27^{+0.01}_{-0.01}$	$4.34^{+0.96}_{-0.52}$	$-0.96^{+0.13}_{-0.19}$	$-0.23^{+0.05}_{-0.06}$	$0.41^{+0.07}_{-0.08}$	$-0.11^{+0.11}_{-0.08}$	$0.01^{+0.05}_{-0.07}$	$0.88^{+0.07}_{-0.10}$	$0.98^{+0.02}_{-0.26}$	131.21	FIT-CSMF
5	WMAP1	$10.46^{+0.06}_{-0.09}$	$11.30^{+0.09}_{-0.18}$	$0.25^{+0.02}_{-0.02}$	$3.69^{+0.85}_{-0.46}$	$-0.87^{+0.10}_{-0.14}$	$-0.20^{+0.06}_{-0.06}$	$0.37^{+0.09}_{-0.05}$	$-0.18^{+0.08}_{-0.09}$	$0.04^{+0.03}_{-0.05}$	$0.97^{+0.23}_{-0.14}$	$0.94^{+0.06}_{-0.50}$	123.92	FIT-2PCF
6		$10.39^{+0.04}_{-0.06}$	$11.17^{+0.09}_{-0.10}$	$0.26^{+0.02}_{-0.01}$	$4.34^{+0.62}_{-0.54}$	$-0.93^{+0.16}_{-0.12}$	$-0.21^{+0.05}_{-0.09}$	$0.38^{+0.06}_{-0.08}$	$-0.17^{+0.10}_{-0.09}$	$0.03^{+0.05}_{-0.04}$	$1.03^{+0.13}_{-0.09}$	$0.69^{+0.18}_{-0.21}$	131.82	FIT-CSMF
7	WMAP3	$10.49^{+0.03}_{-0.05}$	$11.16^{+0.05}_{-0.08}$	$0.24^{+0.02}_{-0.02}$	$3.91^{+0.45}_{-0.37}$	$-0.93^{+0.13}_{-0.12}$	$-0.28^{+0.07}_{-0.04}$	$0.41^{+0.07}_{-0.06}$	$-0.11^{+0.10}_{-0.08}$	$0.03^{+0.02}_{-0.08}$	$1.30^{+0.25}_{-0.17}$	$0.99^{+0.01}_{-0.99}$	167.19	FIT-2PCF
8		$10.37^{+0.04}_{-0.06}$	$10.94^{+0.13}_{-0.08}$	$0.26^{+0.02}_{-0.01}$	$4.82^{+0.61}_{-0.76}$	$-1.03^{+0.19}_{-0.10}$	$-0.26^{+0.06}_{-0.04}$	$0.43^{+0.06}_{-0.09}$	$-0.04^{+0.11}_{-0.07}$	$0.00^{+0.03}_{-0.07}$	$0.85^{+0.10}_{-0.06}$	$1.00^{+0.00}_{-0.09}$	126.71	FIT-CSMF
9	WMAP5	$10.56^{+0.03}_{-0.14}$	$11.31^{+0.07}_{-0.19}$	$0.22^{+0.05}_{-0.01}$	$3.54^{+0.75}_{-0.33}$	$-0.90^{+0.10}_{-0.16}$	$-0.25^{+0.06}_{-0.05}$	$0.42^{+0.07}_{-0.07}$	$-0.16^{+0.10}_{-0.08}$	$0.03^{+0.03}_{-0.06}$	$1.25^{+0.21}_{-0.17}$	$0.98^{+0.02}_{-0.72}$	135.77	FIT-2PCF
10		$10.36^{+0.05}_{-0.06}$	$11.06^{+0.08}_{-0.15}$	$0.27^{+0.01}_{-0.01}$	$4.34^{+0.96}_{-0.52}$	$-0.96^{+0.13}_{-0.19}$	$-0.23^{+0.05}_{-0.06}$	$0.41^{+0.07}_{-0.08}$	$-0.11^{+0.11}_{-0.08}$	$0.01^{+0.05}_{-0.07}$	$0.88^{+0.07}_{-0.10}$	$0.98^{+0.02}_{-0.26}$	131.21	FIT-CSMF
11	Millennium	$10.47^{+0.07}_{-0.03}$	$11.19^{+0.12}_{-0.05}$	$0.24^{+0.01}_{-0.02}$	$3.73^{+0.33}_{-0.44}$	$-0.86^{+0.21}_{-0.18}$	$-0.19^{+0.06}_{-0.07}$	$0.36^{+0.09}_{-0.09}$	$-0.10^{+0.05}_{-0.10}$	$0.02^{+0.03}_{-0.05}$	$0.97^{+0.19}_{-0.12}$	$0.99^{+0.01}_{-0.36}$	114.40	FIT-2PCF
12		$10.37^{+0.05}_{-0.06}$	$11.01^{+0.13}_{-0.10}$	$0.26^{+0.02}_{-0.01}$	$4.61^{+0.69}_{-0.66}$	$-0.84^{+0.19}_{-0.20}$	$-0.21^{+0.09}_{-0.09}$	$0.29^{+0.11}_{-0.07}$	$-0.04^{+0.10}_{-0.10}$	$0.03^{+0.03}_{-0.05}$	$1.06^{+0.13}_{-0.11}$	$0.48^{+0.23}_{-0.10}$	130.37	FIT-CSMF

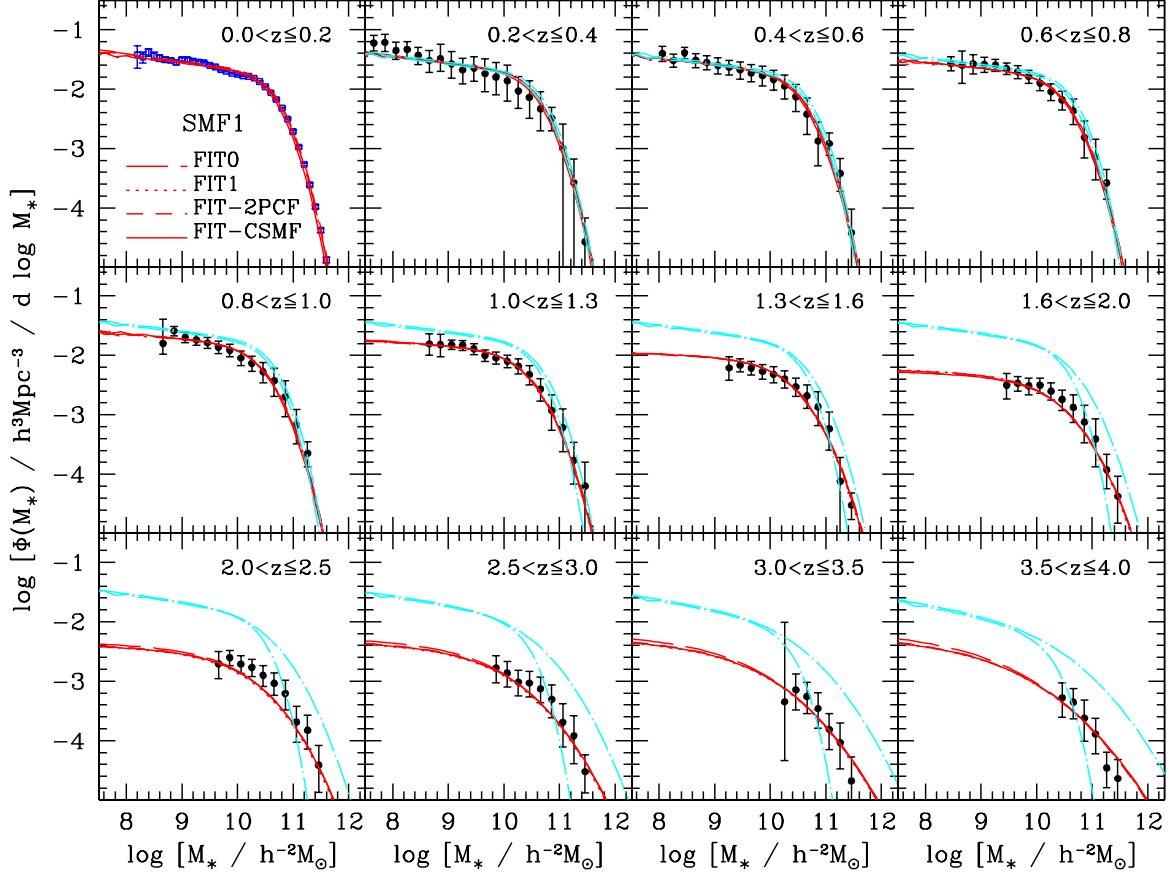NOTE. — The same as Table 3, but here SMF2 is used instead of SMF1.

FIG. 6.— The predicted stellar mass functions (SMFs) of galaxies in different redshift bins compared with the observed SMF of SDSS DR7 and those of PG08 (other panels). In each panel, the long-dashed, dotted, dashed and solid lines, which are quite similar, show the predictions of models FIT0, FIT1, FIT-2PCF and FIT-CSMF, respectively, for the case of SMF1 and assuming the WMAP7 cosmology. In each panel, the dot-long-dashed lines are the predictions for the "no-evolution model" in which we have assumed that the central galaxy - halo relation does not evolve and is the same as that at $z = 0.1$. Here results for $\sigma_c(z) = 0.173$ (smaller at massive end and at high redshift) and $\sigma_c(z) = \max[0.173, 0.2z]$ are plotted together for comparison.
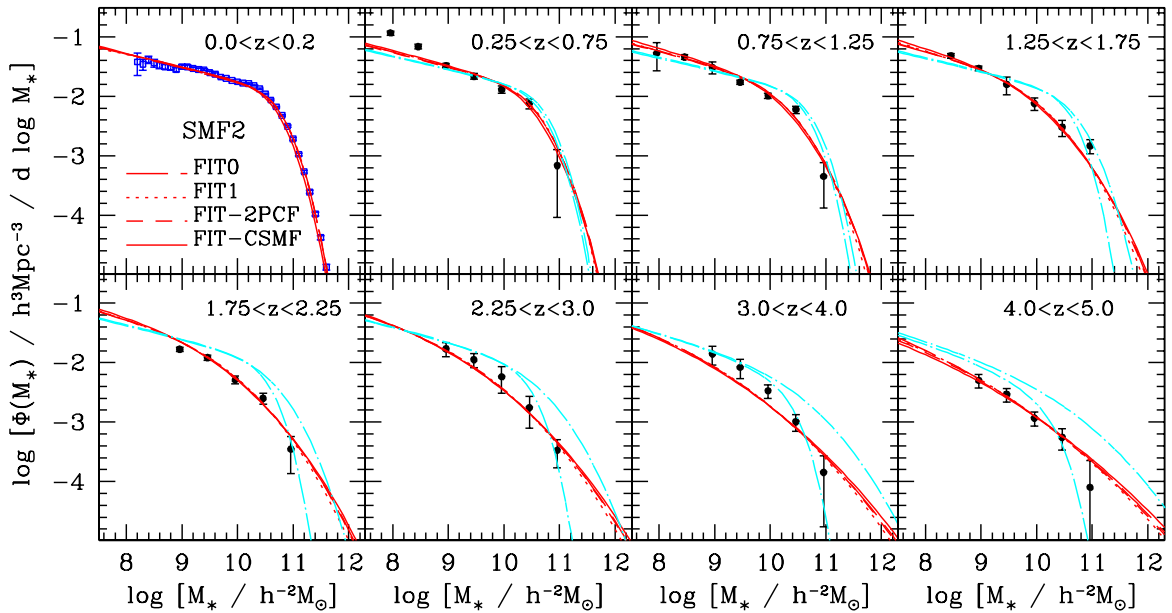
FIG. 7.— Similar to Fig. 6, but here SMF2 has been used as constraints. The data shown (symbols) are the stellar mass functions of SDSS DR7 (first panel) and D05 (other panels).
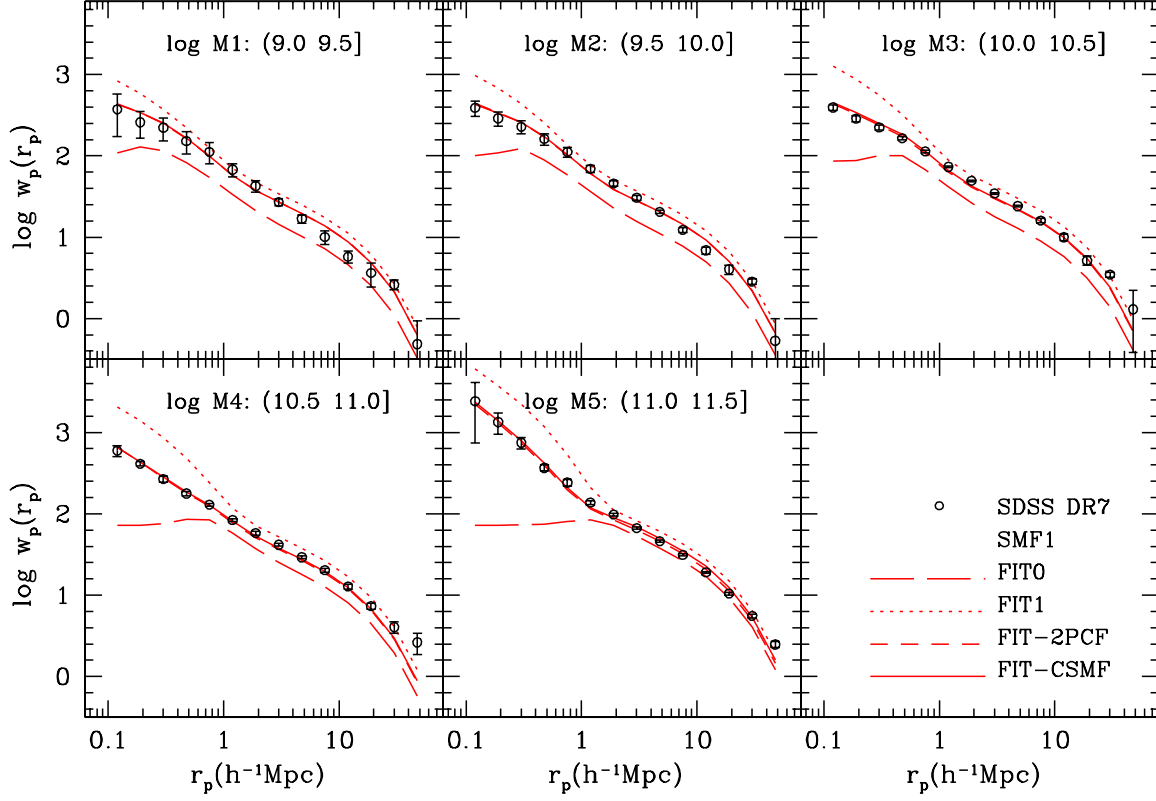
FIG. 8.— The projected 2PCFs of galaxies in different stellar mass bins as indicated by the $\log[M_*/(h^{-2}\,M_\odot)]$-values in brackets. Open circles with error bars are the observational measurements from the SDSS DR7 described in Appendix A. The solid, dashed, dotted and long dashed lines show the predictions for models FIT-CSMF, FIT-2PCF, FIT1 and FIT0, respectively, where SMF1 has been used as constraints for the stellar mass functions.
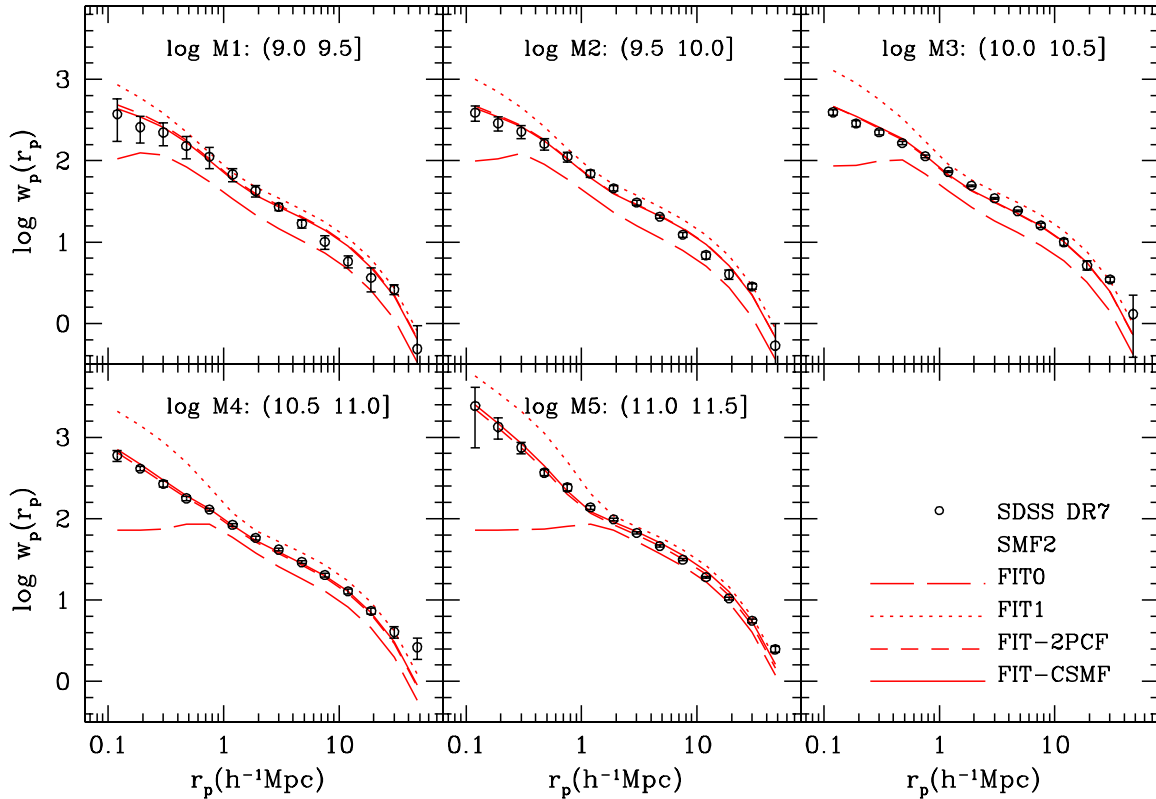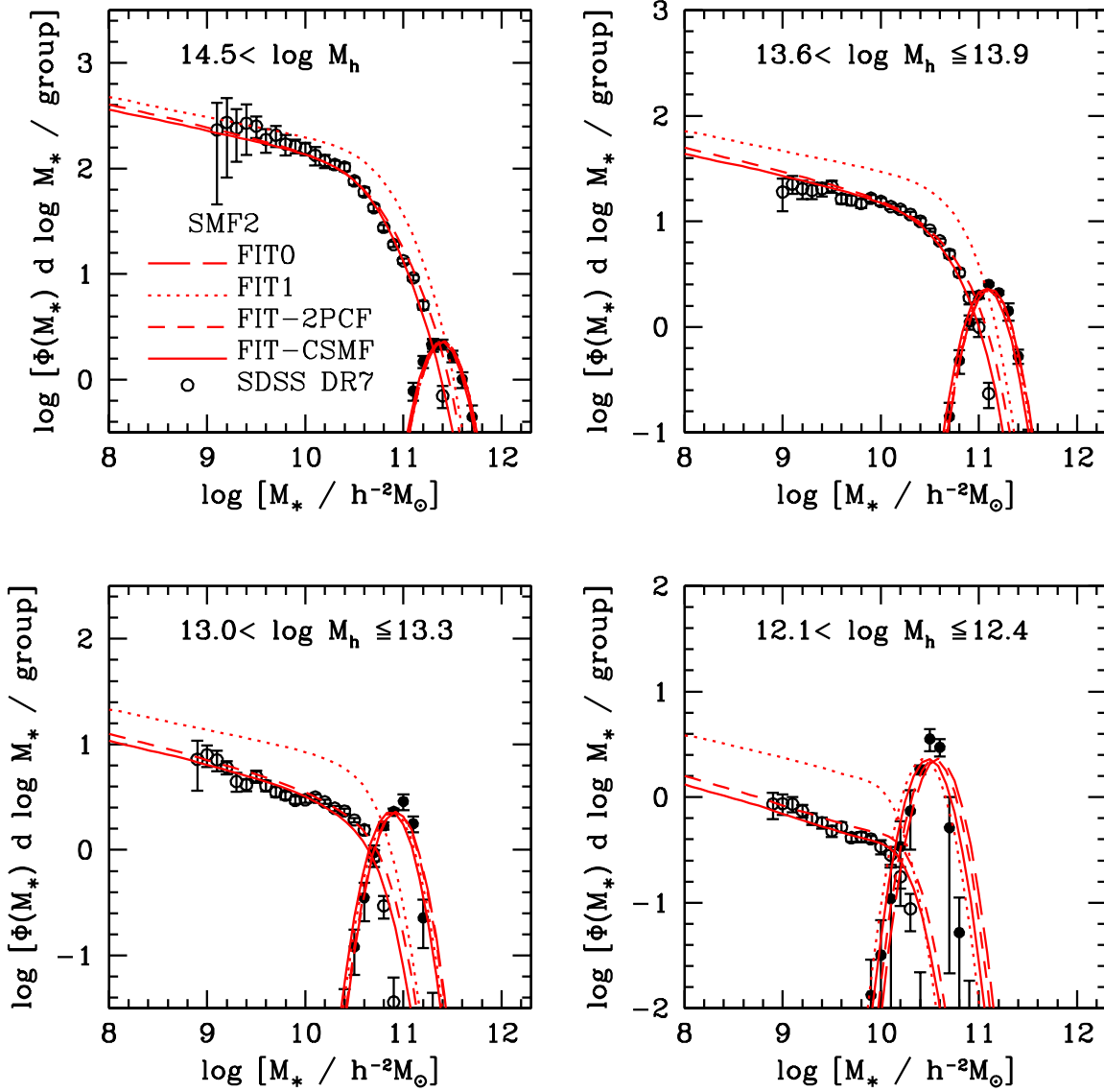

FIG. 9.— Same as Fig. 8, except that here SMF2 has been used as constraints for the stellar mass functions.
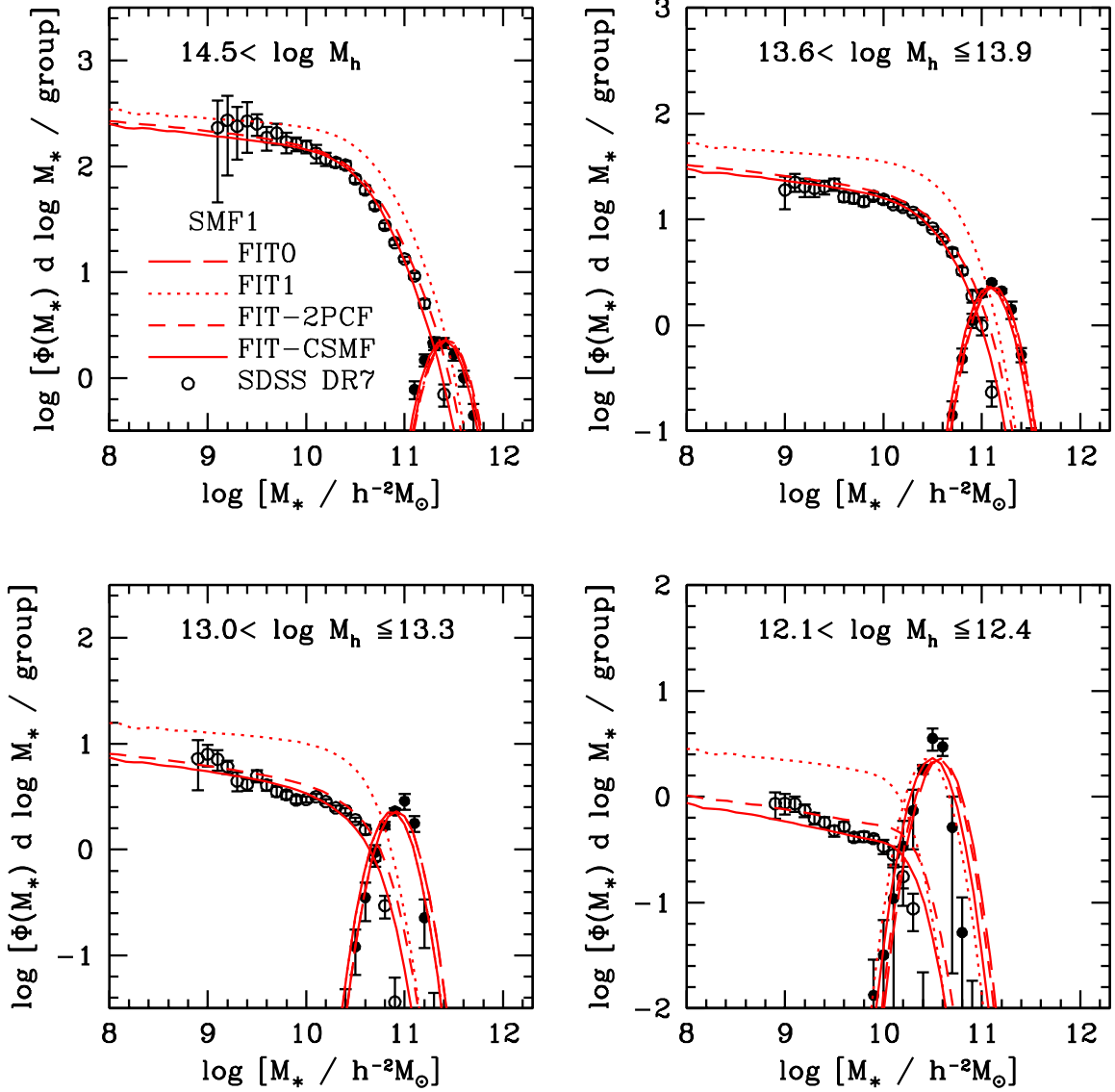
FIG. 10.— The conditional stellar mass functions for central and satellite galaxies in halos of different masses as indicated in each panel (the unit of M_h used is $h^{-1}M_\odot$). The filled dots and open circles are the measurements from the SDSS DR7 group catalogue for central and satellite galaxies (see Appendix B), respectively. The error bars represent scatter among different bootstrap samples. The long-dashed, dotted, dashed and solid lines in each panel show the predictions for models FIT0, FIT1, FIT-2PCF and FIT-CSMF, respectively. Note that the satellite component is absent in FIT0. Here we have adopted the WMAP7 cosmology and used SMF1 as constraints for the stellar mass functions.

FIG. 11.— Same as Fig. 10, except that here SMF2 has been used as constraints for the stellar mass functions.

garding the satellite fractions, and so it is also interesting to look at the model predictions for $\Phi(M_*|M)$. The long-dashed and dotted lines in Fig. 10 (for SMF1) and Fig. 11 (for SMF2) show the $z = 0.1$ predictions of models FIT0 and FIT1, respectively. Note that by definition there are no satellite galaxies in FIT0, so that there are no long-dashed lines present for the satellite components. For comparison, the solid dots and open circles are observational measurements obtained from SDSS DR7 (see Section 4.1.2). Note how FIT0 and FIT1 predict CSMFs for centrals that are very similar, and in good agreement with the data. However, model FIT1 clearly, and significantly, over-predicts the CSMFs of satellites, while FIT0 also clearly fails to match the data since it predicts zero satellites. Once again, the observed CSMFs of satellites falls in between the predictions of these two extreme models, suggesting that the actual CSMF data can be used to constrain model parameters, especially p_t and c.

Finally, Fig. 12 shows the $z = 0.1$ relation between halo mass, M, and the stellar mass of the central galaxy, $M_{*,c}$ (upper panels), and the ratio $M_{*,c}/M$ (lower panels). Here results for SMF1 and SMF2 are shown in the left- and right-hand panels, respectively, while long-dashed and dotted lines once again correspond to the extreme models FIT0 and FIT1. Note how both models are virtually indistinguishable at the high mass end, and in good agreement with the results of Yang et al. (2008) obtained directly from the SDSS group catalog (open circles with errorbars), here updated according to the latest SDSS DR7. At the low mass end, however, FIT0 predicts $M_{*,c}$ that are significantly higher than FIT1. The reason is simple: having no satellites forces model FIT0 to assign a larger number of massive galaxies, which otherwise would have been assigned to massive halos as satellites, to relatively low-mass halos as centrals. Thus a self-consistent modelling that takes into account the subhalo accretion times and the evolution of satellite galaxies after accretion mainly impacts the $M_{*,c}$ - M relation at the low-mass end. Such behavior has also been noticed, e.g., in Moster et al. (2010) and Behroozi et al. (2010). Note also that the $M_{*,c}$ - M relations obtained from SMF1 and
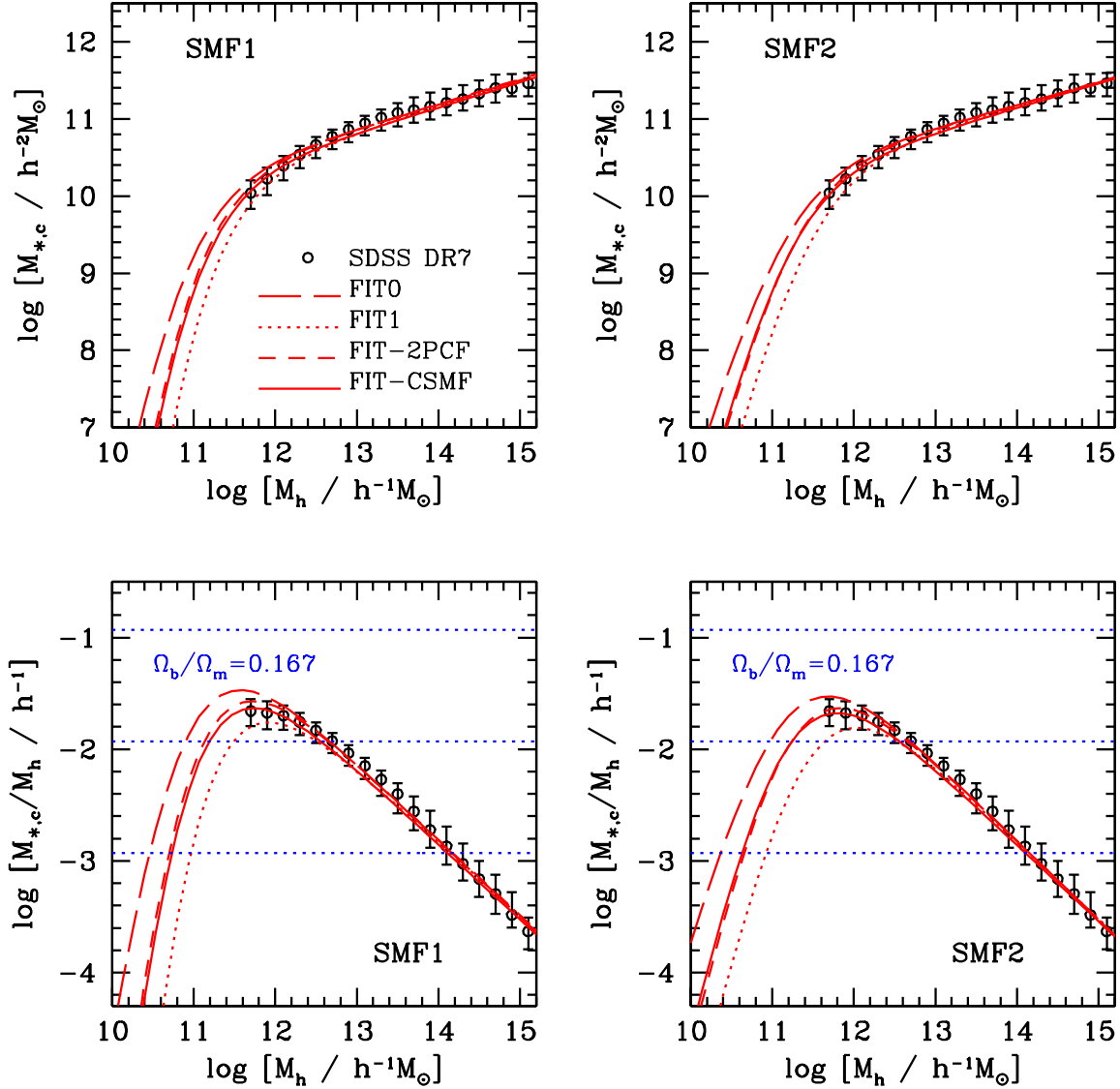
FIG. 12.— The $M_{*,c}$ - M relations (upper panels) and the $M_{*,c}/M$ ratios (lower panels) as function of halo mass. Results are shown separately for SMF1 (left panels) and SMF2 (right panels), assuming WMAP7 cosmology. Here the results are for galaxies at redshift $z = 0.1$. The long-dashed, dotted, dashed and solid lines are the predictions for models FIT0, FIT1, FIT-2PCF and FIT-CSMF, respectively. The open circles with error-bars are the direct measurements obtained from the SDSS group catalogue (e.g., Yang et al. 2008), here updated to the latest DR7. As an illustration, the horizontal dotted lines in the lower panels indicate the mass ratios corresponding to 100%, 10% and 1% of the universal mass ratio between baryonic and total matter; $\Omega_{\rm b}/\Omega_{\rm m} = 0.167$.

SMF2 are quite similar over the entire halo mass range.

Next we focus on the results obtained from FIT-2PCF and FIT-CSMF, in which all 11 parameters are kept free, and the observed SMFs are combined either with the 2PCFs (in FIT-2PCF) or the CSMFs (in FIT-CSMF) to constrain the model parameters. The fitting results are shown in Fig. 6 through 12 as the dashed and solid lines, respectively. The best fit values for each of the 11 model parameters are listed under IDs 3 and 4 in Tables 3 (for SMF1) and 4 (for SMF2). There are a number of points worth noting:

- For a given set of SMFs (SMF1 or SMF2), the results obtained from FIT-2PCF and FIT-CSMF are quite similar, showing that the 2PCFs and CSMFs constrain the model in a similar way.

- The best-fit values for p_t fall between about 0.8 and

1.3, which is roughly consistent with the canonical value, $p_t = 1.0$, expected from the dynamical friction time of subhalos in numerical simulations. The value of parameter c, which is much larger than 0 in most cases, indicates that there is evolution in the mass of satellite galaxies. The mass growth for low-mass satellites after their accretion into the host halo is particularly significant, as indicated by the redshift dependent $M_{*,c} - M_h$ relations shown in Fig. 13. For a given set of SMFs (SMF1 or SMF2), FIT-2PCF yields larger p_t (or c) (by $\sim 30\%$) than FIT-CSMF, because FIT-2PCF slightly over-predicts the CSMFs, as shown in Figs. 10 and 11.

- Using SMF1 or SMF2 leads to very similar predictions for the CSMF of central galaxies, but SMF2 yields larger satellite fractions at the low mass end

(Figs. 10 and 11).

- Models FIT-2PCF and FIT-CSMF predict $M_{*,c}$ - M and $M_{*,c}/M$ - M relations at low-z that are very similar, and that lie between the predictions of FIT0 and FIT1 (see Fig.12). They are also in good agreement with the results obtained directly from the SDSS DR7 galaxy group catalogs. These two models predict a maximum for the $M_{*,c}/M$ ratio of $\sim 0.02h^{-1}$ at a halo mass $M \simeq 10^{11.8} \, h^{-1}\mathrm{M_\odot}$, indicating that galaxy formation is most efficient on this mass scale (at least at low-z). Note that a value of $M_{*,c}/M = 0.02h^{-1} \simeq 0.03$ is about a factor of six lower than the average baryonic to total mass ratio $\Omega_b/\Omega_m \simeq 0.167$ (e.g., Komatsu et al. 2011) of the Universe (indicated by the upper horizontal dotted lines in the lower panels of Fig. 12). This indicates that the overall star formation efficiency is low. Furthermore, since atomic and/or molecular gas typically contribute only a small fraction of the total baryonic mass of (massive) galaxies, this furthermore underscores that the process of galaxy formation has either prevented most of the baryons from cooling, or has somehow managed to eject them from the galaxy.

- The central stellar mass increases with halo mass roughly as $M^{0.3}$ at the massive end and as M^8 for SMF1 (M^4 for SMF2) at the low-mass end. In low-mass halos, the use of SMF2 leads to more massive central galaxies than the use of SMF1 (Fig.12). This arises because the stellar mass functions in SMF2 are steeper at the low-mass end.

- Although the parameters in $\sigma_c(z)$ are not treated as free parameter in our model constraints, its impact is quite significant, especially at high redshift where the scatter is large. This is demonstrated by the predictions of the 'no-evolution' models shown in Figs. 6 and 7. Here the $M_{*,c}$ - M relations at high-z are assumed to be the same as that at $z = 0.1$. Two cases are considered, one assuming $\sigma_c(z) = 0.173$ and the other $\sigma_c(z) = \max[0.173, 0.2z]$. Note that these two assumptions give very different predictions for the high-z SMFs at the massive end, demonstrating that $\sigma_c(z)$ needs to be treated properly in order to obtain reliable predictions for the high-z SMFs at the massive end.

- Finally, as demonstrated by the similar χ^2 values for different ΛCDM models, we note that the clustering of galaxies alone can not put stringent constraints on cosmological parameters.

These results clearly demonstrate that the observed SMFs at different redshifts, and the CSMFs and 2PCFs at low-z can all be accommodated self-consistently within the current ΛCDM model, which specifies the mass and bias functions of dark matter host halos, the mass function and accretion times of dark matter subhalos, and the orbital decay times of subhalos within their hosts.

6. IMPLICATIONS FOR THE ASSEMBLY OF GALAXIES

The main ingredient of our model is a description of the relation between halo mass and the stellar mass of its central galaxy, as a function of redshift. In the previous section we have seen how this relation can be constrained using observational data. We now investigate what our models imply for the assembly of galaxies.

6.1. *The Galaxy Mass - Halo Mass Relation*

The upper panels of Fig. 13 show the $M_{*,c}$ - M relations at different redshifts predicted by model FIT-CSMF (results for FIT-2PCF are fairly similar). The lower panels show the same relations, but this time in terms of the mass ratio $M_{*,c}/M$. Results are shown separately for models that are constrained by SMF1 (left-hand panels) and SMF2 (right-hand panels). For comparison, in Fig. 14 we also plot the results obtained from SMF1 (red dot-dashed lines) and SMF2 (red solid lines) at each redshift in the same panel, together with a no-evolution model (cyan dashed line) and two models from the literature (Moster et al. 2010, blue dotted lines, and Leauthaud et al. 2012, green long-dashed lines).

At all redshifts the central stellar mass increases with halo mass. For massive halos with $M \gtrsim 10^{13} \, h^{-1}\mathrm{M_\odot}$, the (average) central stellar mass is actually more massive at higher redshift. Note, though, that this does not mean that the stellar mass of a particular central galaxy decreases with time. After all, the main branch mass of a halo also increases with time. However, it *does* mean that the central stellar mass cannot grow proportionally to halo mass. The straight dashed lines in Figs. 13 and 14 mark a stellar mass of $10^{11.8}h^{-2} \, \mathrm{M_\odot}$, which roughly corresponds to the largest stellar mass in the SDSS survey (see Fig. 19). If galaxies more massive than this are absent from the local universe, it is reasonable to assume that there are also no such galaxies at higher redshifts. Note that this is consistent with the SMFs shown in Figs.6 and 7. Unfortunately, since the high-mass ends of the high-z SMFs are uncertain (as massive galaxies are rare and current survey volumes are relatively small) and can be quite significantly impacted by the actual scatter in the stellar mass estimations (see the cyan, dot-dashed curves in Figs. 6 and 7 for an illustration), the $M_{*,c}$ - M relation is not well constrained at the very massive end. Nevertheless, despite the uncertainties, the observational data clearly indicate that the central galaxy of a high-mass halo at high-z (usually too rare to be observed) is more massive than that of a low-z halo of the same mass. As we will see in more detail in Section 6.3, this also means that massive galaxies, currently residing in massive halos, must have formed early in progenitor halos with much lower masses. The stellar masses of these massive galaxies have increased little during the later growth of their host halos, indicating that star formation in these galaxies must have ceased at early times, and that they have not cannibalized too many (massive) satellites.

For low-mass halos, especially those with $M \lesssim 10^{12} \, h^{-1}\mathrm{M_\odot}$, there is a huge increase in the stellar mass for a given halo mass from $z \gtrsim 2$ to $z \sim 0$. This increase is more than a factor of 10 for SMF1 and a factor of more than 3 for SMF2 (see Fig. 14). This has important implications for the star formation efficiencies in low mass halos at high z. Afterall, the $M_{*,c}/M$ ratio of low mass halos at low z is already far below the uni-
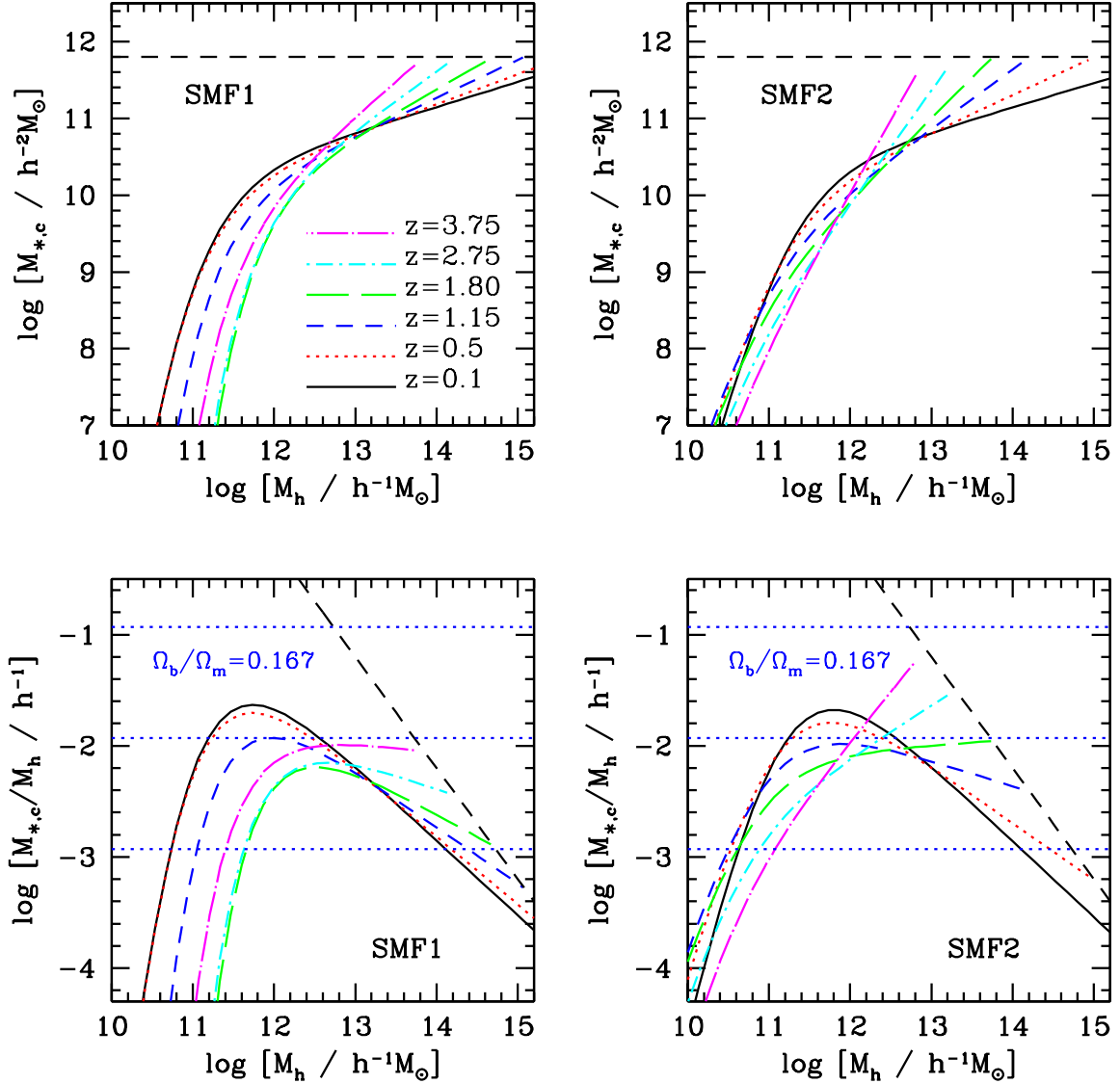
FIG. 13.— Similar to Fig. 12, but here we show model predictions at different redshifts. Results are shown separately for SMF1 (left-hand panels) and SMF2 (right-hand panels). For simplicity, results are only shown for model FIT-CSMF, although the results for model FIT-2PCF are very similar. The black dashed lines correspond to $M_* = 10^{11.8} h^{-2}$ M$_\odot$, which roughly reflects the observed stellar mass limit of galaxies.

versal baryon fraction (see lower panels of Fig. 13). If this ratio is a factor 3 to 10 lower at higher redshifts, it indicates that star formation in these halos must be extremely inefficient. As to be discussed in more detail in Section 7, this poses a serious challenge to our current theory of galaxy formation. Although it is standard practice to invoke supernova feedback as a feedback mechanism to suppress star formation in low mass haloes, this process is not expected to be very efficient in haloes with $M \gtrsim 10^{11} h^{-1}$M$_\odot$ (e.g., Dekel & Silk 1986), and it appears that additional mechanisms are required to explain the low inferred star formation efficiencies at high-z. Alternatively, one might question whether the data for faint galaxies is sufficiently reliable. After all, the SMFs at the low-mass ends obtained by D05 are significantly higher than those by PG08. However, as one can infer from a comparison between the data points and the cyan, dot-dashed curves in Figs. 6 and 7, the 'no-evolution' assumption (assuming the $M_{*,c}$ - M relations at high-z to

be the same as that at $z = 0.1$) over-predicts the high-z stellar mass functions at the low-mass ends by very large amounts, about a factor of 5 for SMF1 and about a factor of 2 for SMF2 at $\log(M_*/ h^{-2}$M$_\odot) \sim 10$ at redshift $z \sim 2.0$. Such large discrepancies are difficult to be explained by observational uncertainties. Indeed, as shown in Marchesini et al. (2009), the SMFs of D05 at the low-mass ends are already the highest among a handful of independent observations. Hence, the implied low star formation efficiencies in low-mass halos at high-z have to be taken serious.

6.2. Comparison with Previous Studies

For completeness, we compare our results regarding the evolution of the $M_{*,c}$-M relation to a few previous studies. Note that in order to carry out proper comparisons, one needs to take into account various systematics among different analyses. First, most of the analyses, except perhaps those based on gravitational lensing, have
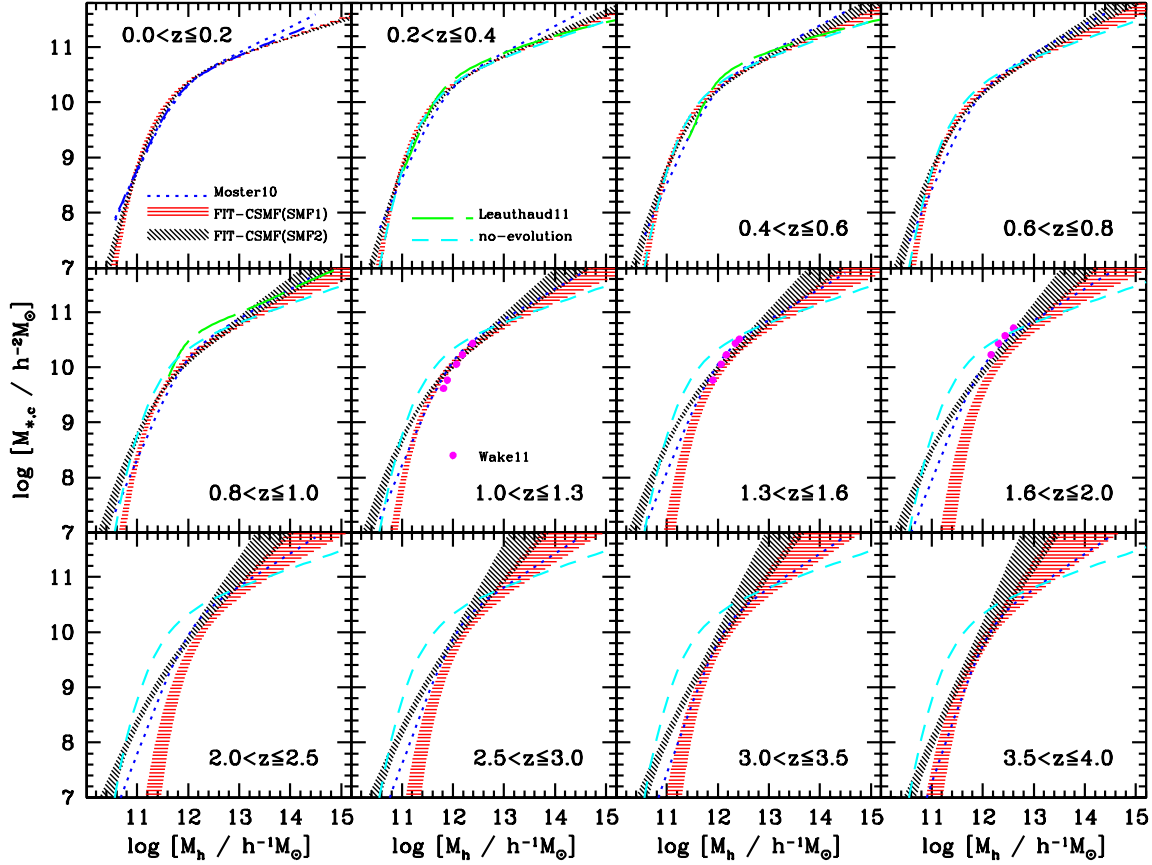
Fig. 14.— The $M_{*,c}$ - M relations in different redshift bins. In each panel we compare the predictions of model FIT-CSMF using SMF1 and using SMF2 (shaded areas for the 68% confidence levels as indicated), respectively. For comparison, we also show in each panel the prediction of the "no-evolution model", which simply is the $M_{*,c}$ - M relation at $z = 0.1$ (using SMF1; dashed line), and the model predictions of Moster et al. (2010; dotted line). In addition, for three redshift bins we also indicate the model predictions obtained by Leauthaud et al. (2012; long-dashed lines) and Wake et al. (2011; filled dots), respectively.

to assume a cosmology, so that the result is cosmology dependent (see van den Bosch et al. 2003b). Second, different SED (Spectral Energy Distribution) fitting codes may yield significantly different stellar masses even with the same IMF (see e.g. Behroozi et al. 2010). Finally, the uncertainty in the stellar masses may be redshift dependent (e.g. Drory et al. 2005).

At low redshift, the $M_{*,c}$-M relation has been studied not only in the framework of HOD/CLF, but also with the use of weak gravitational lensing, X-ray observations, and satellite kinematics. As shown in More et al. (2009) and Leauthaud et al. (2012), these measurements are in general agreement with each other. As we have shown above, our results at redshift $z = 0.1$ are in good agreement with those of Yang et al. (2008), and thus are also in agreement with other results (see e.g., More et al. 2009). Here we focus on comparison of results at high redshift.

Moster et al. (2010) used a method that is very similar to subhalo abundance matching, and stellar mass functions of Fontana et al. (2006) covering a wide range in redshifts, to constrain the galaxy-dark matter connection from $z \sim 4$ to the present. The resulting $M_{*,c}$ - M relations are shown as blue, dotted lines in Fig. 14. At low redshift, Moster et al. used the stellar mass function of Panter et al. (2007), which is actually very similar to the SMF (for SDSS DR7) we adopt (see Fig. 2). The signifi-

cantly higher $M_{*,c}$ at the massive end obtained by Moster et al. (2010) is likely due to the following two factors. First, the model of Moster et al. (2010) assumes zero scatter in the $M_{*,c}$ - M relation. As a demonstration, we show their model prediction assuming $\sigma_c = 0.15$ instead of $\sigma_c = 0$ in the top-left panel of Fig. 14 as the dot-dashed line. As one can see, assuming a finite dispersion indeed significantly suppresses the slope of the $M_{*,c}$ - M relation at the high mass end. Second, Moster et al.'s results are based on abundance matching using a particular N-body simulation of a box size of $L = 100\,\mathrm{Mpc}$, and may be affected by box-size effect, particularly for massive halos. It might be that massive halos are under-represented in their simulation, so that their model has to assign massive galaxies to halos with relatively low masses. At high redshift, Moster et al. used a set of SMFs obtained by Fontana et al. (2006), where uncertainties in the estimated stellar masses might be significant. Nevertheless, if we use the difference in the predictions of SMF1 and SMF2 as an indication of the observational uncertainty, the Moster et al. results are consistent with ours.

We also compare our results to those of Leauthaud et al. (2012), at least for the three redshift bins $0.2 < z \leq 0.4$, $0.4 < z \leq 0.6$, and $0.8 < z \leq 1.0$ (green long-dashed curves in Fig. 14). Rather than using subhalo abundance matching, Leauthaud et al. used galaxy number densities (SMFs), galaxy clustering and galaxy-galaxy lens-

ing in the COSMOS survey (Scoville et al. 2007), in order to constrain the galaxy dark matter connection from $z \simeq 0.2$ to $z \simeq 1.0$. Since they parameterized the occupation statistics of centrals and satellites separately, they effectively allow for a dependence on subhalo accretion times, and for evolution in the satellite population after accretion. A comparison of their $M_{*,c}$ - M relations to ours shows that their stellar masses for central galaxies at a given halo mass are generally very similar to ours, especially for the two low redshift bins. For the highest redshift bin, there is noticeable discrepancy in the intermediate halo mass range ($M \sim 10^{12.0}$). Unfortunately the origin of the discrepancy is not clear.

Finally, we also compare our results to those obtained by Wake et al. (2011) in three redshift bins: $1.0 < z \leq 1.2$, $1.2 < z \leq 1.6$, and $1.6 < z \leq 2.0$ (filled dots in Fig. 12). These data are obtained by fitting HOD models to the abundance and clustering of galaxies, as function of stellar mass, obtained from the NEWFIRM Medium Band Survey (van Dokkum et al. 2009). A comparison with our results shows that their $M_{*,c}$ - M relations are in quite good agreement with our results. Note however, as pointed out in a recent paper by Leauthaud et al. (2011), that using different functional form for the HOD model might impact the average halo masses that host given stellar mass galaxies as well.

6.3. The Growth of Stellar Components in Dark Matter Halos

Using the redshift-dependent CSMFs obtained above, we can predict the growth of the stellar masses of both central and satellite galaxies along the main branch of their dark matter halos. The median stellar mass at redshift z of a central galaxy that at redshift $z_0 \leq z$ is located in a host halo of mass M_0 can be written as

$$M_{*,c}(z|M_0, z_0) = M_{*,c}(M_a, z). \qquad (48)$$

Here, as before, M_a is the median mass at redshift $z \geq z_0$ of the main progenitor of a host halo of mass M_0 at redshift z_0. The median, *total* stellar mass of surviving satellite galaxies in the main branch can be obtained by integrating the CSMF of satellite galaxies:

$$m_{*,s}(z|M_0, z_0) = \int \mathrm{d}\log m_* \, m_* \, \Phi_{\mathrm{s}}(m_*|M_a, z). \qquad (49)$$

Thus, once we know the assembly history of a dark matter halo, it is straightforward to use our model to obtain the corresponding assembly histories of the stellar components of its central and satellite galaxies. In addition, we also examine what the models predict for the total mass of satellite galaxies that have been accreted onto the main branch, which includes the surviving satellites as well as those that have been cannibalized by the central or disrupted by the tidal field. Note that here we have taken into account the evolution of the satellite galaxies after their accretion, e.g. the addtional star formation and passive evolution, using the parameter c. This component is thus given by

$$m_{*,\mathrm{acc}}(z|M_0, z_0) = \int_{z_0}^{z} \frac{\mathrm{d}z_a}{(1+z_a)} \int \mathrm{d}\log m_* \, m_* \qquad (50)$$
$$\Phi_{\mathrm{e}}(m_*|m_a, z_a, z) \, n_{\mathrm{sub}}(m_a, z_a|M_0, z_0).$$

Here we adopt two different methods to obtain the assembly histories of dark matter halos. The first is based on halo merger trees extracted directly from a large N-body simulation. The second uses the analytical model of Y11 (see also Section 2.4), which relies on the fitting formula of Zhao et al. (2009) to describe the mean assembly history for halos of a given final mass and adopts a log-normal dispersion around the mean main-branch mass at each time. As shown in Y11, this analytical model accurately matches the simulation results averaged over halos of a given final mass. However, it does not fully take into account the variance among different halos, as it ignores the covariance of the masses at different times along individual main branches. Using the merger trees extracted from the numerical simulations does not suffer from this shortcoming and therefore allows us to get an estimate for the halo-to-halo scatter, taking full account of the variance in their assembly histories.

The simulation used here is the $300 h^{-1}$Mpc simulation box described in Y11, which evolves 1024^3 dark matter particles in a WMAP5 cosmology from redshift $z = 100$ to the present epoch ($z = 0$) using the massively parallel GADGET2 code (Springel et al. 2001; 2005). The particle mass and softening length are $1.87 \times 10^9 \, h^{-1} \mathrm{M}_\odot$ and $6.75 \, h^{-1}$kpc, respectively. A total of 100 outputs are available between $z = 50$ and $z = 0$, spaced in equal $\log(1+z)$ intervals. Dark matter halos were identified at each output using the standard friends-of-friends (FOF) algorithm (Davis et al. 1985) with a linking length of 0.2 times the mean interparticle separation. Only halos with at least 20 particles are used. Based on halos at different outputs, halo merger trees were constructed. A halo in an earlier output is considered to be a progenitor of the present halo if more than half of its particles are found in the present halo. The main branch of a merger tree is defined to consist of all the progenitors as one climbs from the bottom to the top, choosing always the most massive branch at every branching point. These progenitors are the main-branch progenitors, and the time dependence of the main branch mass is the assembly history of the halo. We extracted 200 merger trees for present-day halos in each of the mass bins centered at $\log(M/h^{-1}\mathrm{M}_\odot) = 12.0$, 13.0, 14.0 and 14.5. The median and the 68% range of the distribution of assembly histories thus obtained are indicated as solid lines and hatched areas, respectively, in the panels in the top row of Fig. 15. For comparison, the dotted lines indicate the mean assembly histories obtained using the analytical model of Zhao et al. (2009), which are in excellent agreement with the solid lines. In general, more massive halos assemble later than smaller ones, which reflects the hierarchical nature of structure formation in the CDM model (e.g., van den Bosch 2002; Wechsler et al. 2002). Note that, as we have tested our results using another set of halo merger trees constructed with a different method from simulations of the WMAP1 cosmology (Han et al. 2011), we found that our results are robust against the change in cosmology and in the method of merger-tree construction.

In the following subsections, we use these halo assembly histories to examine in detail how the different stellar components in dark matter halos (central galaxies, satellite galaxies, and halo stars) grow with time.
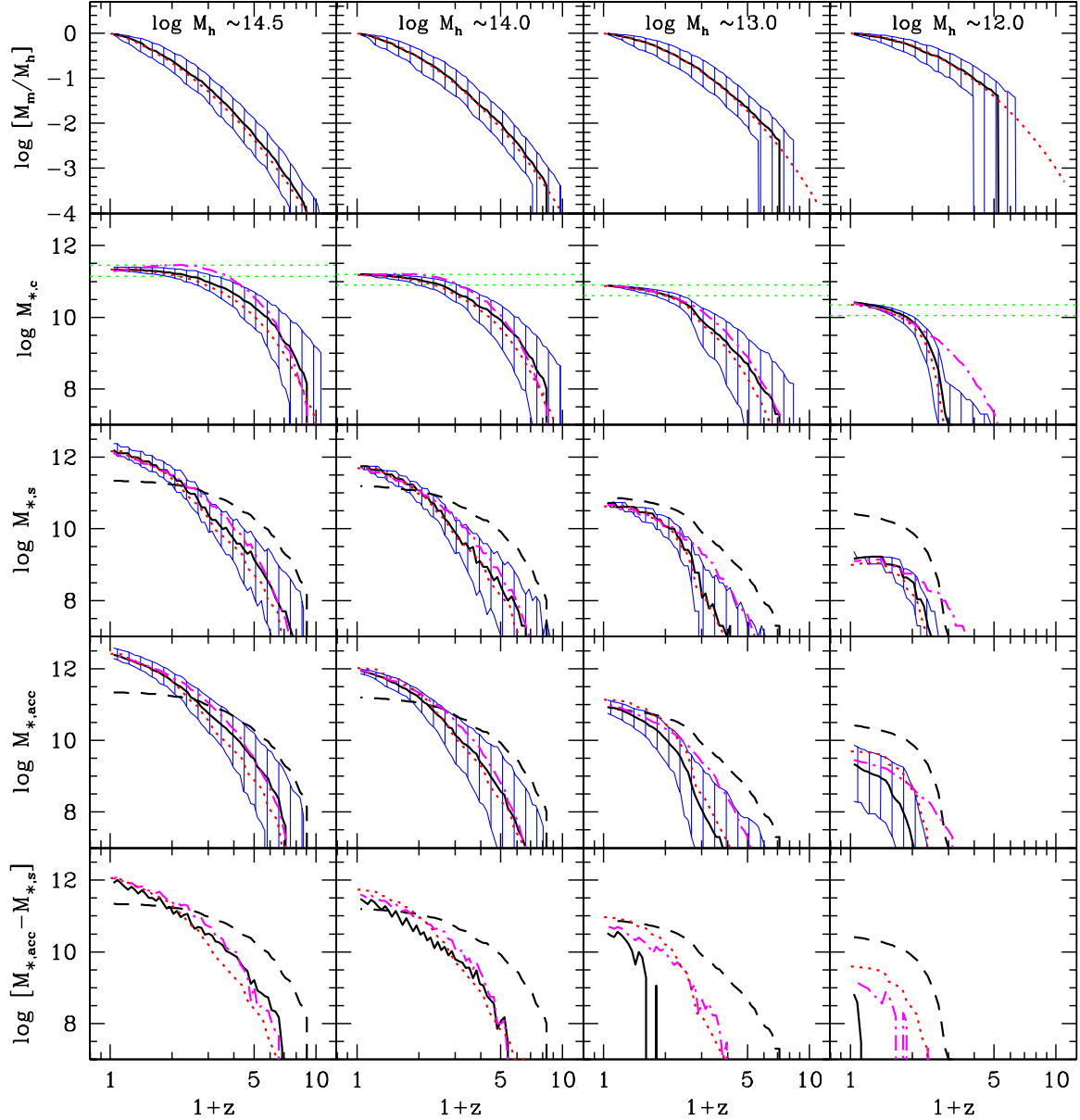
6.3.1. Central Galaxies

FIG. 15.— The growth of host (main branch) halo mass (top row panels), the stellar mass of central galaxies (second row), the total stellar mass in surviving satellite galaxies (third row), the total stellar mass brought into the main branch by sub-halos (fourth row), and the stellar mass of the "disrupted" component (bottom row, see text for definition), all as function of redshift. These results are obtained using the best-fit parameters of model ID=10, listed in Table 3 (using WMAP5 cosmology and SMF1). Results in different columns correspond to host halos with masses centered at $\log(M/h^{-1}\mathrm{M}_\odot) = 14.5$, 14.0, 13.0 and 12.0, from left to right. The solid line and shaded area in each panel indicate the median and 68% percentile obtained from 200 simulated halo merger trees. The dotted line is the prediction obtained using the analytical model of Y11. The two horizontal dotted lines in the second row indicate the maximum and half-maximum values of the median stellar mass of the central galaxies. The dashed lines in the third, fourth and bottom rows are the same as the solid lines in the top panels. Finally, for comparison, the dot-dashed lines (in all rows except the top one) are model predictions obtained using the best fit parameters of model ID=10 listed in Table 4 (using WMAP5 cosmology and SMF2).

Using model FIT-CSMF for the WMAP5 cosmology (ID=10 in Tables 3 and 4), we populate the host halos in the simulation outputs with central galaxies[5]. Here we ignore the scatter in the central stellar mass - halo mass relation, simply because it is relatively small and because it is difficult to take it into account properly owing to possible covariances between the stellar masses in the main branch of a halo at different times. The results are shown in the second row of Fig. 15, where different panels correspond to different present-day halo masses, as indicated in the top panels. The solid lines and shaded areas indicate the median and 68 percentiles of $M_{*,c}(z|M_0, z_0)$ obtained from 200 halo merger trees. For comparison, the red, dotted curves show the $M_{*,c}(z|M_0, z_0)$ obtained from Eq. (48). Note that these agree extremely well with the results obtained from the merger trees in the numerical simulations.

In each panel, the two horizontal doted lines indicate

[5] We have also used the FIT-2PCF models (ID=9) instead, and found very similar results. For the sake of brevity, we will only show results for model FIT-CSMF.
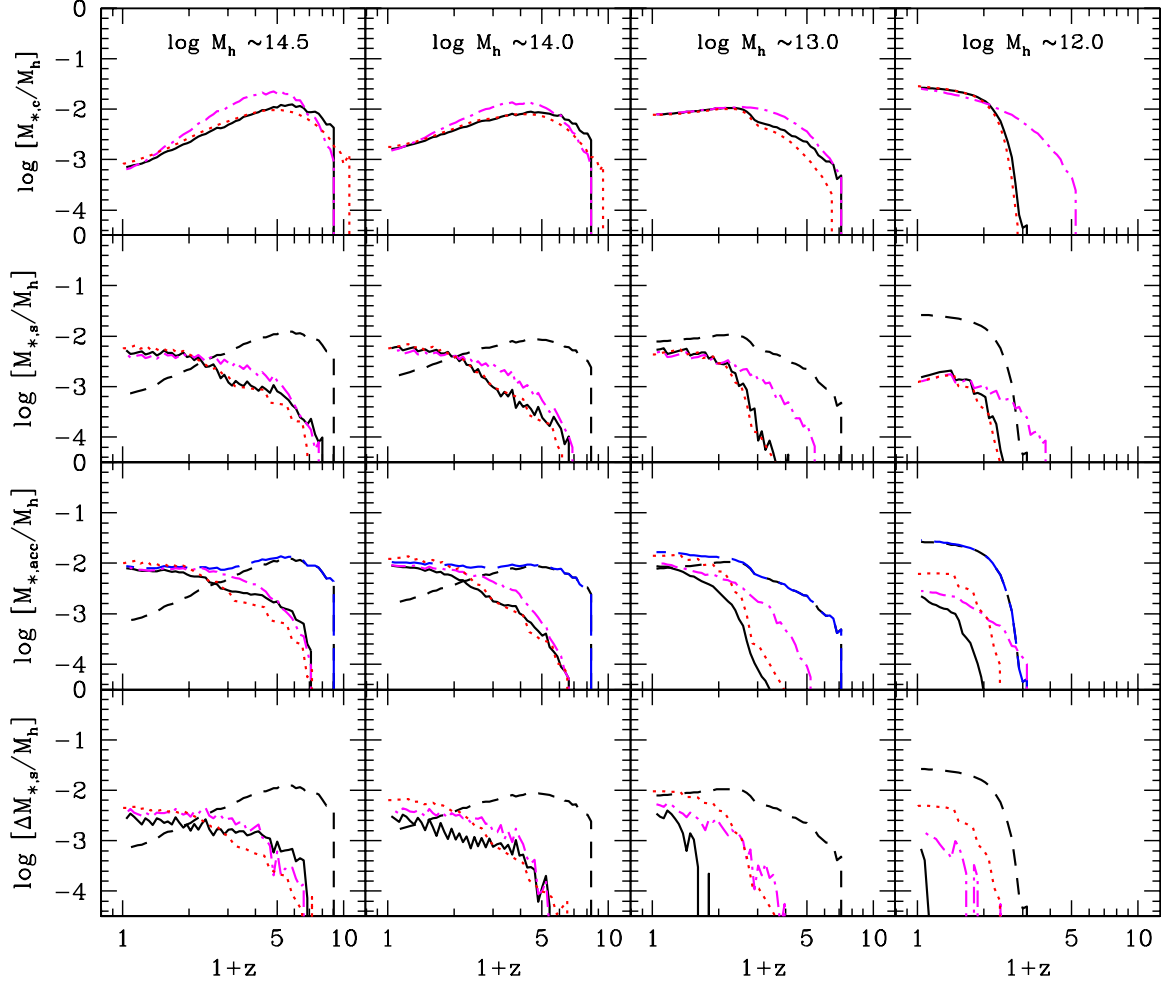
FIG. 16.— Similar to the lower four rows of Fig. 15, but this time we have normalized all stellar masses by the median, instantaneous main-branch halo mass, M_h (the solid lines in the top panels of Fig. 15); i.e., the various lines indicate the *median* stellar-to-halo mass ratios (in units of h^{-1}). From the top row to the bottom row, the results are shown for the stellar mass in central galaxies (first row), the total stellar mass in surviving satellite galaxies (second row), the total stellar mass brought into the main branch by sub-halos (third row), and the stellar mass of the "disrupted" component (bottom row). Line styles are the same as in Fig. 15.

the maximum and half of the maximum of the median stellar mass of the central galaxies at $z = 0$. These can be used to read off when the central galaxies, on average, acquired half their present day stellar masses; for centrals in present-day halos of $\log(M/h^{-1}M_\odot) \sim 12.0$, 13.0, 14.0 and 14.5 this occurs at $z \sim 0.5$, 1.0, 1.5 and 2.0, respectively. Thus, although more massive halos assemble their masses later, their central galaxies actually assembled *earlier* than centrals in lower-mass halos (see also Conroy & Wechsler 2009). Note how the stellar mass assembly histories of central galaxies reach a plateau in halos with $M \gtrsim 10^{13}\ h^{-1}M_\odot$, indicating that central galaxies in massive halos grow very little in stellar mass at low redshifts. In particular, central galaxies in clusters with $M \sim 10^{14.5}h^{-1}M_\odot$ have not grown in mass (significantly) since $z \sim 1.0$. In contrast, central galaxies in Milky-Way sized halos with $M \sim 10^{12}\ h^{-1}M_\odot$ continue to grow in stellar mass down to the present day. The slow growth of central galaxies in massive halos suggests not only that their star formation must have been quenched by some processes, but also that their increase in stellar mass due to the accretion of satellite galaxies cannot have been significant. As discussed in Section 7, this has important

implications for our understanding of galaxy formation and evolution.

Another interesting way to depict the growth of the stellar mass of central galaxies is to show the ratio between stellar mass and host halo mass (the main branch mass) at the redshift in question. These curves are shown in the top panels of Fig. 16 using the same line styles as in Fig. 15. As one can see, central galaxies in host halos of different final masses reach a maximum of about $(0.015 - 0.03)h^{-1}$, quite independent of the final host halo mass. However, the maximum is reached at very different redshifts of $z \sim 5$, 4, 1.5 and 0 for $\log(M/h^{-1}M_\odot) \sim 14.5$, 14.0, 13.0, and 12.0, respectively. Interestingly, all these redshifts roughly correspond to a similar main branch mass of $\sim 10^{12}\ h^{-1}M_\odot$.

Finally, in order to illustrate the effects of the uncertainties in the high-z SMF measurements, the magenta dot-dashed curves in Figs. 15 and 16 show the median stellar masses obtained using the D05 SMFs (case SMF2, the best-fit parameters of which are listed under ID=10 in Table 4). The results are qualitatively the same as those obtained from SMF1. However, the stellar masses of central galaxies in low-mass halos at high-z are higher

than those obtained from SMF1. This simply reflects that the high-z SMFs of D05 are significantly steeper at the low mass end than the PG08 SMFs (see Fig. 3).

6.3.2. *Satellite Galaxies*

Next we use the merger trees in our simulation box to investigate how the population of surviving satellite galaxies grows in stellar mass. The results are shown in the third row of panels in Fig. 15. Once again the solid lines and shaded areas indicate the median and 68 percentiles of $m_{*,s}(z|M_0, z_0)$ obtained from 200 halo merger trees, while the red dotted lines indicate the $\langle m_{*,s} \rangle(z|M_0, z_0)$ obtained from Eq. (49) using the analytical model of Y11 for the halo assembly history. The black, dashed lines indicate the median of the stellar mass of central galaxies, taken from the panels in the second row, and are shown for comparison. As one can see, the total mass of satellites only becomes larger than that of the central galaxy in massive halos at low redshifts. In Milky-Way sized halos the total satellite mass never exceeds $\sim 10\%$ of the central mass. For all halos, satellite galaxies contain less than a few percent of the total stellar mass at all $z \gtrsim 3$. The total satellite mass in a massive halo continues to grow all the way to the present time, whereas the central galaxy ceases to grow once the halo mass reaches $\sim 10^{12} h^{-1} M_\odot$. As shown by the magenta, dot-dashed lines, the use of SMF2 predicts higher satellite masses at high-z than the use of SMF1, especially in low-mass halos. Once again this reflects the fact that the high-z SMFs of D05 are steeper at the low mass end than their PG08 counterparts.

The ratios between the total satellite mass and the main branch halo mass are shown in the second row of Fig. 16. For low-mass halos and for massive halos at early times, this ratio increases rapidly with time, implying that the total satellite mass grows faster than the halo mass. The reason for this is that for a given halo mass, the stellar mass of central galaxies in low-mass halos increases rapidly with time (see upper panels of Fig. 16), and so the ratio between the stellar mass and dark matter mass of the accreted matter increases rapidly with time. For massive halos, the ratio flattens at low-z to a value $\sim 0.002 h^{-1}$, corresponding to a halo mass to stellar mass ratio of $\sim 200h$ which is close to the universal mass-to-light ratio.

6.3.3. *Halo Stars and Star Formation in Central Galaxies*

The third component we consider is the total stellar mass that is brought into the main branch by all satellite galaxies at the time of their accretion. Here we have taken into account the later evolution effect of the satellite galaxies, such as the addtional star formation and passive evolution. This mass contains not only the mass of the 'surviving' satellite galaxies, but also that of the satellites that have been cannibalized or disrupted. The mass growth histories of this mass component are shown in the fourth row of Fig. 15, where as before the solid lines and shaded areas depict the medians and 68 percentiles obtained from 200 merger trees, respectively. The dotted lines show the results obtained by integrating Eq. (50). The corresponding ratios between this mass component and the main branch halo mass are shown in the third row of panels of Fig. 16. In halos with $M \lesssim 10^{13} h^{-1} M_\odot$, the total accreted stellar mass

is roughly similar to that of the surviving satellite population. In halos with $M \gtrsim 10^{14} h^{-1} M_\odot$, however, the total accreted stellar masses are significantly larger than those in the surviving satellite population, especially at low redshift ($z \lesssim 1.0$). This is more clearly seen in the bottom rows of Fig. 15 and 16, which show the differences between the median accreted mass and the median mass of the surviving satellites. This indicates that in massive halos a significant fraction of the total stellar mass brought in by subhalos is actually not associated with surviving satellite galaxies and must exist in other forms. For convenience, we will refer to this stellar mass component as the "disrupted" component.

There are two possible fates for the disrupted component: either it is accreted by the central galaxy or it gives rise to a population of halo stars (also referred to as intracluster stars, or ICS, in the case of massive halos). Unfortunately, our model cannot uniquely discriminate between these two components, as the mass of the central galaxy can also grow through star formation. However, we can obtain important constraints by comparing the growth of the disrupted component to that of the central galaxies (black, dashed lines). This shows that central galaxies in halos with $M \lesssim 10^{14} h^{-1} M_\odot$ must have grown mainly through *in situ* star formation, simply because the total mass in the disrupted component is much smaller than that of the central. For more massive halos, however, the situation could be very different. Here the total stellar mass in the disrupted component is actually larger than that of the central galaxy. Hence, the existence of ICS is inevitable; the total stellar mass locked up in the stellar halo can be more than 2 times as massive as the central galaxy at redshifts $z < 1.5$ (see also Purcell et al. 2007). As one can see from the left two panels in the bottom row of Fig. 15, although the total mass of the disrupted fraction is sufficient to form the central galaxy in massive halos, in reality central galaxies in these halos must have acquired their stellar mass mainly through *in situ* star formation, rather than through the accretion of satellites (see also results along this line obtained from hydro-dynamical simulations by e.g., Naab et al. 2009; Oser et al. 2010; 2012; Hrischmann et al. 2012). This can be inferred from the fact that these central galaxies have already build up most of their stellar mass at high redshifts, when the mass in the disrupted component is too small to make a dominant contribution. Accretion can only be significant at $z \lesssim 2$ in massive halos, when the disrupted component is sufficiently massive compared to the mass of the central. However, at these low redshifts, the central galaxies in these massive halos no longer seem to grow much in stellar mass. Hence, even central galaxies in massive halos must have mainly grown via *in situ* star formation.

Finally, we point out that the use of SMF2 leads to masses in the disrupted component that are quite similar to those obtained using SMF1. The higher total accreted mass predicted with SMF2 for low-mass halos at high-z is largely due to the higher mass in the survived satellites. Note also that the analytical model predicts larger disrupted components in low-mass halos at high-z than using the merger trees in the numerical simulation (cf solid black lines and dotted red lines in the bottom panels of Figs. 15 and 16). This is mainly due to the
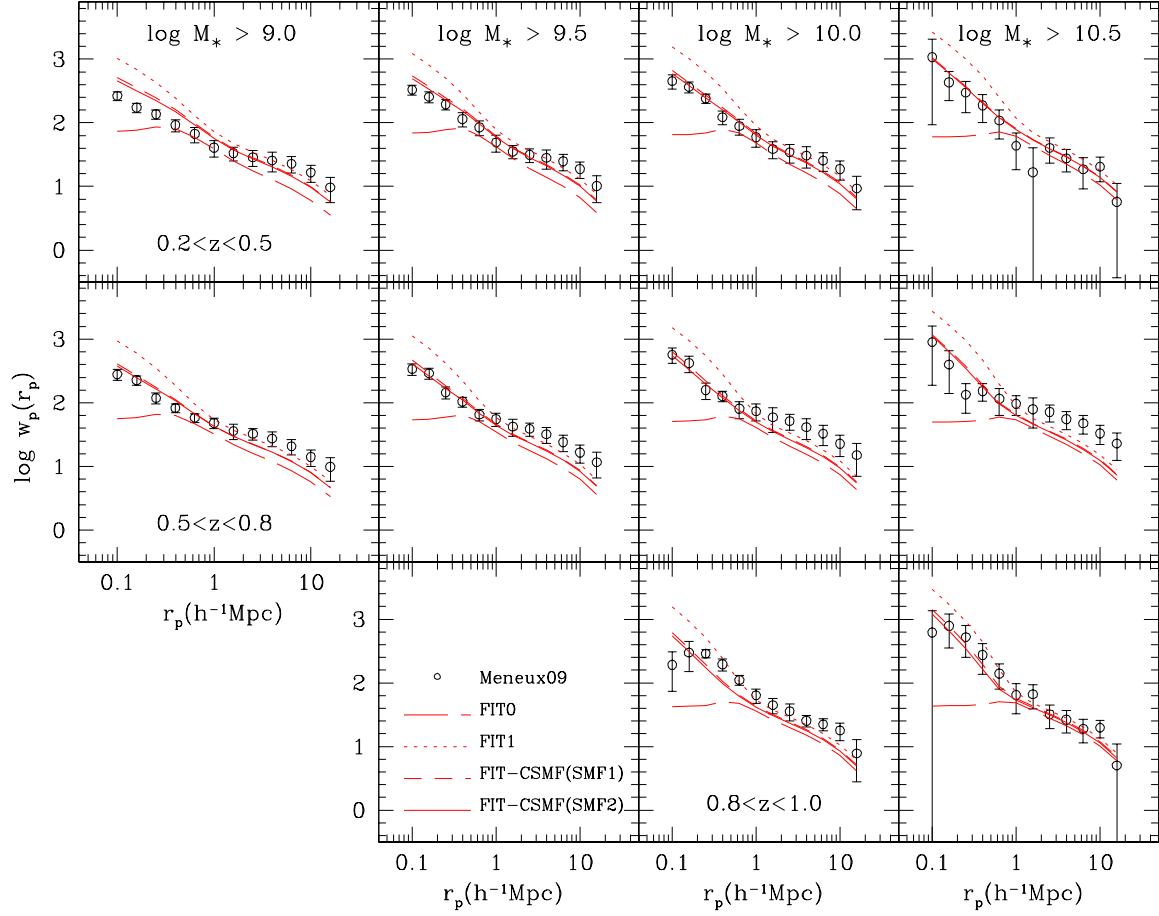
FIG. 17.— The projected 2PCFs for galaxies in different stellar mass and redshift bins. Here we compare model predictions (various lines) with the observational measurements obtained by Meneux et al. (2009) from zCOSMOS (open circles with error-bars). The long-dashed, dotted, and dashed lines show the predictions of models FIT0, FIT1, and FIT-CSMF, respectively, all of which have used SMF1 as constraints for the stellar mass functions. For comparison, the solid lines show the predictions for model FIT-CSMF using SMF2.
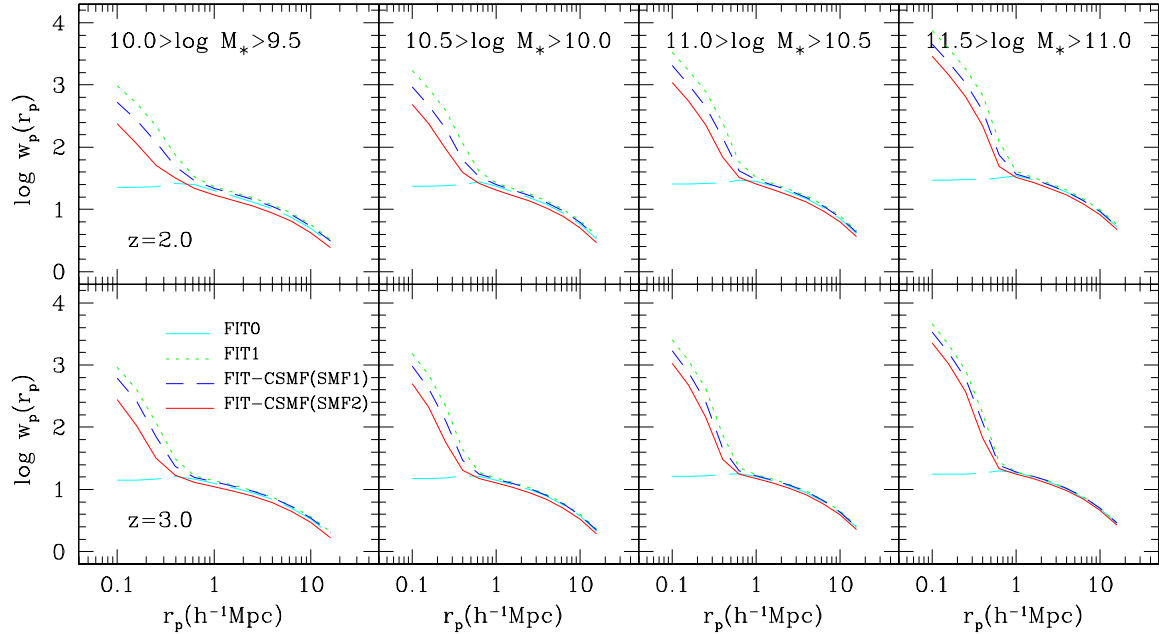

FIG. 18.— Predictions for the projected 2PCFs in different stellar mass bins at redshifts $z = 2.0$ (upper panels) and $z = 3.0$ (lower panels). Results are shown for the same four models as in Fig. 17, using the same line-styles, as indicated.

fact that small progenitors are not well resolved in the simulation at high-z (see the top-right panel of Fig. 15).

6.4. *Galaxy Clustering at High Redshift*

With the model described in Section 3.2, we are also able to predict the correlation functions of galaxies at high-z. In Fig. 17 we show the model predictions for FIT0, FIT1, and FIT-CSMF using SMF1 as well as for FIT-CSMF using SMF2 (the predictions of FIT-2PCF are similar to those of FIT-CSMF). The model predictions are compared with the observational results of Meneux et al. (2009), which are shown as open circles with errorbars. As one can see, all our models underpredict the correlation function on large scales, particularly for galaxies in the redshift range $0.5 < z < 0.8$. As pointed out in Meneux et al. (2009), and as briefly mentioned in Section 6.1 above, these enhanced correlations on large scales are likely due to the fact that the zCOS-MOS field happens to correspond to a high density region of the Universe. Nevertheless, the results show that different models predict very different correlations on small scale ($r_{\rm p} \lesssim 1 h^{-1}$Mpc), once again demonstrating that accurate clustering measurements on small scales can provide important constraints on the galaxy-dark matter connection (in particular regarding the dynamical evolution of satellite galaxies).

In Fig. 18 we show model predictions for the projected 2PCFs at $z = 2.0$ (upper panels) and $z = 3.0$ (lower panels). Here again results are shown for FIT0, FIT1, and FIT-CSMF using SMF1, as well as FIT-CSMF using SMF2. Different panels correspond to galaxies in different stellar mass ranges, as indicated. The projected 2PCFs on large scales decrease with both increasing redshift and decreasing stellar mass. Note that the differences among the different models are extremely small at large scale ($r_{\rm p} \gtrsim 1 h^{-1}$Mpc). On small scales our models predict that the 2PCFs are greatly enhanced relative to a simple extrapolation from large scales, except for the FIT0 models which has zero satellites, and therefore no one-halo term. Note that this enhancement is stronger for more massive galaxies, and that it is fairly different for the different models. Hence, as for the low-z 2PCFs, the clustering strength on large scales does not provide much more information than the SMFs themselves (see also Moster et al. 2010), while that on small scales does.

7. SUMMARY AND DISCUSSION

In this paper we have developed a new and self-consistent model that describes the galaxy-dark matter connection over cosmic history. Unlike the popular abundance matching technique, our model takes account of the fact that sub-halos in a host halo are accreted at different times, so that the stellar masses associated with them are likely to depend on both their halo masses at accretion and their accretion times. In addition, our model allows for dynamical evolution of the satellite population (mass stripping, tidal disruption, cannibalism).

We have used galaxy stellar mass functions observed in the redshift range $0 \leq z \lesssim 4$, together with the conditional stellar mass function and two-point correlation functions (both at $z \simeq 0.1$, and both obtained from SDSS), to constrain the evolution of the galaxy-dark matter connection from $z \sim 4$ to the present. The relation between halo mass and stellar mass thus obtained

is used, together with simulated and theoretical halo assembly histories, to predict how the masses of different stellar components in dark matter halos (central galaxies, satellite galaxies, and halo stars) evolve as function of time. We also used our model to predict the 2PCFs of high-z galaxies as a function of their stellar masses. Our main findings can be summarized as follows.

1. Our model provides a reasonable fit to all the data within the observational uncertainties, which indicates that the current ΛCDM model is consistent with a wide variety of data regarding the galaxy population across cosmic time.

2. At low-z, the stellar mass of central galaxies, $M_{*,c}$, increases with halo mass as $M^{0.3}$ and $M^{\gtrsim 4.0}$ at the massive and low-mass ends, respectively. The ratio $M_{*,c}/M$ reveals a maximum of ~ 0.03 at a halo mass $M \sim 10^{11.8} h^{-1} {\rm M}_\odot$. The fact that this maximum value is much lower than the universal baryon fraction (~ 0.17) reflects the overall inefficiency of star formation. At higher redshifts the maximum in $M_{*,c}/M$ remains close to ~ 0.03, but shifts to higher halo mass (see also Wake et al. 2011).

3. The $M_{*,c}$-M relations obtained here are roughly in agreement with previous studies (e.g., Moster et al. 2010; Wang & Jing 2010; Leauthaud et al. 2012). However, our model allows us to put constraints on the satellite population so that we can interpret the results in terms of the evolution of galaxies in dark halos. We find that low-mass satellite galaxies can significantly increase their stellar masses after accretions by their host halos.

4. The time-scale for the disruption of satellite galaxies is about the same as the dynamical friction time scale of their subhalos obtained in N-body simulations, suggesting that most disruption occurs once the galaxy has 'depleted' its orbital energy, at which point it is either accreted by the central galaxy or torn apart by the strong tidal field.

5. The stellar mass assembly history for central galaxies is completely decoupled from the assembly history of its host halo. Initially the ratio $M_{*,c}/M$ increases rapidly with time, until the halo mass reaches $\sim 10^{12} h^{-1} {\rm M}_\odot$, at which point $M_{*,c}/M \sim 0.03$. Once $M \gtrsim 10^{12} h^{-1} {\rm M}_\odot$, there is little growth in $M_{*,c}$, causing the ratio $M_{*,c}/M$ to decline.

6. Most massive centrals assemble their stellar mass earlier than their less massive counterparts, even though their host haloes assemble later. In Milky-Way sized halos more than half of the central stellar mass is assembled at $z \lesssim 0.5$, while brightest cluster galaxies had already grown to half their present day stellar mass by $z \simeq 2.0$.

7. The accretion of satellite galaxies contributes little to the formation of central galaxies in small halos. Hence, most of their stars must have formed *in situ* so that their assembly histories closely resemble their star formation histories. In massive halos more than a half of the stellar mass of the

central galaxy has to be formed *in situ* at $z \gtrsim 2$. The accretion of stars in satellites by the centrals only becomes significant at $z \lesssim 2$, when the total mass available for the accretion reaches a significant fraction of the mass of the central galaxies.

8. In massive halos, the total mass in halo stars is more than two times that of the central galaxy, while in Milky-Way sized halos the mass in halo stars is much smaller ($\lesssim 10\%$) than that of the central galaxy.

9. The 2PCFs of galaxies on large scales do not provide much more constraints than those already provided by the stellar mass functions of galaxies (see also Moster et al. 2010). On small scales, however, the 2PCFs provides important constraint on how satellite galaxies evolve within dark matter halos. Future observations of the small scale clustering strength of galaxies at high-z will therefore be important for our understanding of galaxy formation and evolution. Our models predict that the high-z 2PCFs on small scales are much steeper than at low-z, especially for more massive galaxies.

These results have important implications for our understanding of galaxy formation and evolution. Here we highlight a few issues which we believe to be particularly interesting.

One of the implications of our results is that star formation in low mass halos at high-z must be extremely inefficient. This basically follows from the strong evolution in the $M_{*,c}$-M relation that we infer between high-z and the present at the low mass end: halos of $10^{11} \, h^{-1} \mathrm{M}_\odot$ host central galaxies at $z \sim 4$ that are orders of magnitude less massive than centrals in halos of the same mass at $z = 0$ (see Fig. 13). Note that even at $z = 0$ central galaxies in halos with $M = 10^{11} \, h^{-1} \mathrm{M}_\odot$ have a stellar mass that is only 2-3 percent of the universal baryon fraction. Hence, only a minute fraction of the baryons associated with low mass halos at high-z are turned into stars. It is typically assumed that star formation is suppressed in low-mass halos due to supernova feedback and/or photo-ionization. However, it has become clear in recent years that either the standard treatment of these processes is inadequate, or that additional mechanisms are needed to help suppress star formation in low mass halos. In particular, recent observations have indicated that the specific star formation rates (SSFRs) of star forming galaxies, at fixed stellar mass, increase with redshift from $z = 0$ until they reach a plateau at $z \gtrsim 2$ (see e.g., Stark et al. 2009; Labbé et al 2010a,b; González et al. 2010). As pointed out by several studies, this constancy of the SSFRs is inconsistent with predictions of 'standard' models for galaxy formation, which instead predict SSFRs that continue to increase with redshift (Lo Faro et al. 2009; Dutton, van den Bosch & Dekel 2010; Bouche et al. 2010; Firmani & Avila-Reese 2010; Weinmann, Neistein & Dekel 2011; Lacey et al. 2011). Simply increasing the supernova feedback efficiency in order to lower the star formation rates at high-z is not a solution, because it has no impact on the SSFRs, as it changes both the SFR *and* the stellar mass (Dutton et al. 2010; Bouche et al. 2010). In addition, it will result in

too little stellar mass at low and intermediate redshifts, not to mention the fact that the supernova feedback efficiencies that are typically invoked are already unrealistically high (e.g., Benson et al. 2003). What seems to be needed instead is a modification of the 'standard' model that (i) causes a larger suppression of star formation in low mass halos at high-z, and (ii) a boost in star formation at intermediate redshifts ($z \sim 1-2$). Although there has been no shortage of ideas (e.g., Mo et al. 2005; Lo Faro et al. 2009; Bouche et al. 2010; Lacey et al. 2011; Krumholz & Dekel 2011; Weinmann, Neistein & Dekel 2011; Wang, Weinmann & Neistein 2011; Avila-Reese et al. 2011), it is clear that much more work is required before this outstanding problem in galaxy formation and evolution is adequately addressed. We believe that our constraints on the stellar assembly histories of (central) galaxies may play an important role in testing and calibrating these new models. In particular, the rapid increase in $M_{*,c}/M$ at high-z (before the host halo reaches a mass $M \sim 10^{12} \, h^{-1} \mathrm{M}_\odot$) indicates that the specific star formation rate of (central) galaxies is much higher than the specific growth rate of its dark matter halo, which may hold important clues.

Another intriguing feature from the stellar mass assembly histories is the fact that $M_{*,c}/M$ reaches a maximum of ~ 0.03 once M reaches a mass of $\sim 10^{12} \, h^{-1} \mathrm{M}_\odot$. This feature seems to hold independent of the final host halo mass of the central galaxy. Since, as we have shown, the stellar mass growth in host halos with $M \lesssim 10^{12} \, h^{-1} \mathrm{M}_\odot$ is dominated by *in situ* star formation (rather than accretion), this suggests that something quenches star formation in central galaxies once its halo mass reaches $10^{12} \, h^{-1} \mathrm{M}_\odot$. Interestingly, this mass scale is very similar to the cold-mode to hot-mode transition scale (Birnboim & Dekel 2003; Kereš et al. 2005), suggesting that the quenching of central galaxies coincides with the formation of a hot gaseous halo. This is indeed what seems to be required in order to explain the observed bimodality in colors and/or specific star formation rates of the galaxy population (e.g., Cattaneo et al. 2006; Birnboim et al. 2007). Different mechanisms have been invoked to explain why this transition is associated with a shutdown of star formation in the central galaxies, ranging from AGN feedback (e.g., Tabor & Binney 1993; Ciotti & Ostriker 1997; Croton et al. 2006; Bower et al. 2006; Hopkins et al. 2006) and gravitational heating (e.g., Fabian 2003; Khochfar & Ostriker 2008; Dekel & Birnboim 2008; Birnboim & Dekel 2011) to thermal conduction (e.g., Kim & Narayan 2003) and turbulence (e.g., Zhu, Feng & Fang 2011). Although our results are unable to provide direct insight into the exact quenching mechanism, it is fascinating (or at least reassuring) that our analysis, which uses no (direct) data on star formation rates or the color-bimodality of the galaxy population, also comes to the conclusion that galaxies are quenched once their halo mass reaches $\sim 10^{12} \, h^{-1} \mathrm{M}_\odot$.

Another important result regards the implied buildup of stellar halos. We have argued in Section 6.3.3 that central galaxies build up the vast majority of their stellar mass via *in situ* star formation (the only possible exception are the most massive centrals, which may have build up as much as roughly half their stellar mass via accretion). This implies that the difference between the total

mass in accreted satellites and surviving satellites, what we called the "disrupted" component in Section 6.3.3, must have given rise to a stellar halo. This result is consistent with a number of recent studies which have argued that reconciling halo occupation statistics with halo merger rates requires that a significant fraction of satellite galaxies is indeed tidally disrupted (e.g., Conroy, Ho & White 2007; Conroy, Wechsler & Kravtsov 2007; Kang & van den Bosch 2008; Yang, Mo & van den Bosch 2009a). As these studies have argued, satellite disruption is an important ingredient of galaxy formation, which has hitherto been largely ignored in semi-analytical models. Properly accounting for satellite disruption may alleviate the problem with the excessive growth of massive galaxies (e.g., Monaco et al. 2006; Conroy, Wechsler & Kravtsov 2007, Brown et al. 2008), with the overabundance of satellite galaxies in the semi-analytical models (Liu et al. 2010), and may even be important for understanding the observed metallicities of satellite galaxies (Pasquali et al. 2010). Note that our model predicts that the fraction of stars associated with the stellar halo is an increasing function of halo mass (see also Purcell, Bullock & Zentner 2007 and Henriques, Bertone & Thomas 2008), in qualitative agreement with observations (Gonzalez, Zaritsky & Zabludoff 2007).

Finally we point out that our results may have important implications for the 'missing satellite problem', which refers to the fact that the predicted subhalo count in a Milky-Way (MW) sized halo vastly exceeds the number of observed satellite galaxies in the MW (Moore et al. 1999; Klypin et al. 1999). Although theoretical progress combined with the discovery of a large population of new (typically ultra-faint) satellite galaxies in the Milky Way (e.g., Belokurov et al. 2007) has at least partially alleviated this concern about a mismatch between the numbers of low-mass subhalos and faint MW satellites, it has become clear that it is difficult to reconcile the observed abundance of satellite galaxies with their kinematics: whereas the line-of-sight velocity dispersions of the satellites suggest that they reside in subhalos of relatively low mass, their abundance suggests they reside in much more massive subhalos (e.g., Madau, Diemand & Kuhlen 2008; Boylan-Kolchin, Bullock & Kaplinghat 2011). This problem is particularly acute if one uses subhalo abundance matching techniques to link satellite galaxies to subhalos (e.g., Boylan-Kolchin et al. 2011, see also Busha et al. 2011). As we have argued, subhalo abundance matching is not self-consistent in that it does not account for dependence on subhalo accretion times. Since our model shows that there is very strong redshift dependence in the $M_{*,c}$-M relation at the low mass end, with low mass halos at higher z hosting central galaxies that are much less massive, the large scatter in subhalo accretion times implies a huge amount of scatter in the ratio between the stellar mass of satellite galaxies and their halo mass at infall. Such a large scatter may be exactly what is needed to reconcile the observed satellite population of the MW with predictions from ΛCDM cosmologies (e.g,., Madau et al. 2008), and may already have observational support from the fact that the ultra-faint dwarfs appear to reside in halos of similar mass as the much more massive 'classical' dwarfs (Strigari et al. 2008; Walker et al. 2009). We intend to return to this intriguing issue in more detail in a future paper.

APPENDIX

A. THE PROJECTED TWO-POINT CORRELATION FUNCTION OF GALAXIES AND ITS DEPENDENCE ON STELLAR MASS FROM SDSS DR7

In this Appendix we present our measurements of the projected 2PCFs for galaxies in different stellar mass bins. We use the New York University Value-Added Galaxy Catalogue (NYU-VAGC; Blanton et al. 2005), which is based on SDSS DR7 (Abazajian et al. 2009) but with an independent set of significantly improved reductions. From the NYU-VAGC, we select all galaxies in the Main Galaxy Sample with an extinction corrected apparent magnitude brighter than $r = 17.72$, with redshifts in the range $0.01 \leq z \leq 0.20$ and with a redshift completeness $\mathcal{C}_z > 0.7$. This gives a sample of $639,359$ galaxies with a sky coverage of 7748 square degrees. For each galaxy, we estimate its stellar mass using the fitting formula of Bell et al. (2003).

A.1. Galaxy samples

Galaxies are separated into five stellar mass bins, with $\log[M_*/h^{-2}\mathrm{M}_\odot] = [9.0, 9.5]$, $[9.5, 10.0]$, $[10.0, 10.5]$, $[10.5, 11.0]$ and $[11.0, 11.5]$, respectively. These samples are referred to as 'Mass-limited' samples, and are indicated in the stellar mass versus redshift plot shown in the upper left-hand panel of Fig. 19. The number densities of galaxies in the five stellar mass bins as function of redshift are shown as histograms in the upper right-hand panel of Fig. 19. For clarity the number densities are scaled by constant factors. The advantage of using these 'Mass-limited' samples is that it maximizes the number of galaxies in each mass bin. However, the drawback is that these samples are not homogeneous in the radial direction, and therefore not straightforward to compare with model predictions. We therefore also construct another set of samples as follows: For each of the five stellar mass bins, we first find the maximum number density of galaxies (at some redshift). Next we determine the minimum and maximum redshifts at which the number density of galaxies (in that stellar mass bin) drops to *half* of the maximum value. Only galaxies within these two redshift limits are kept in the sample. In what follows we refer to the five samples thus selected as 'Volume1' samples, and the corresponding number densities as function of redshift are shown as the shaded areas in the upper right-hand panel of Fig. 19.
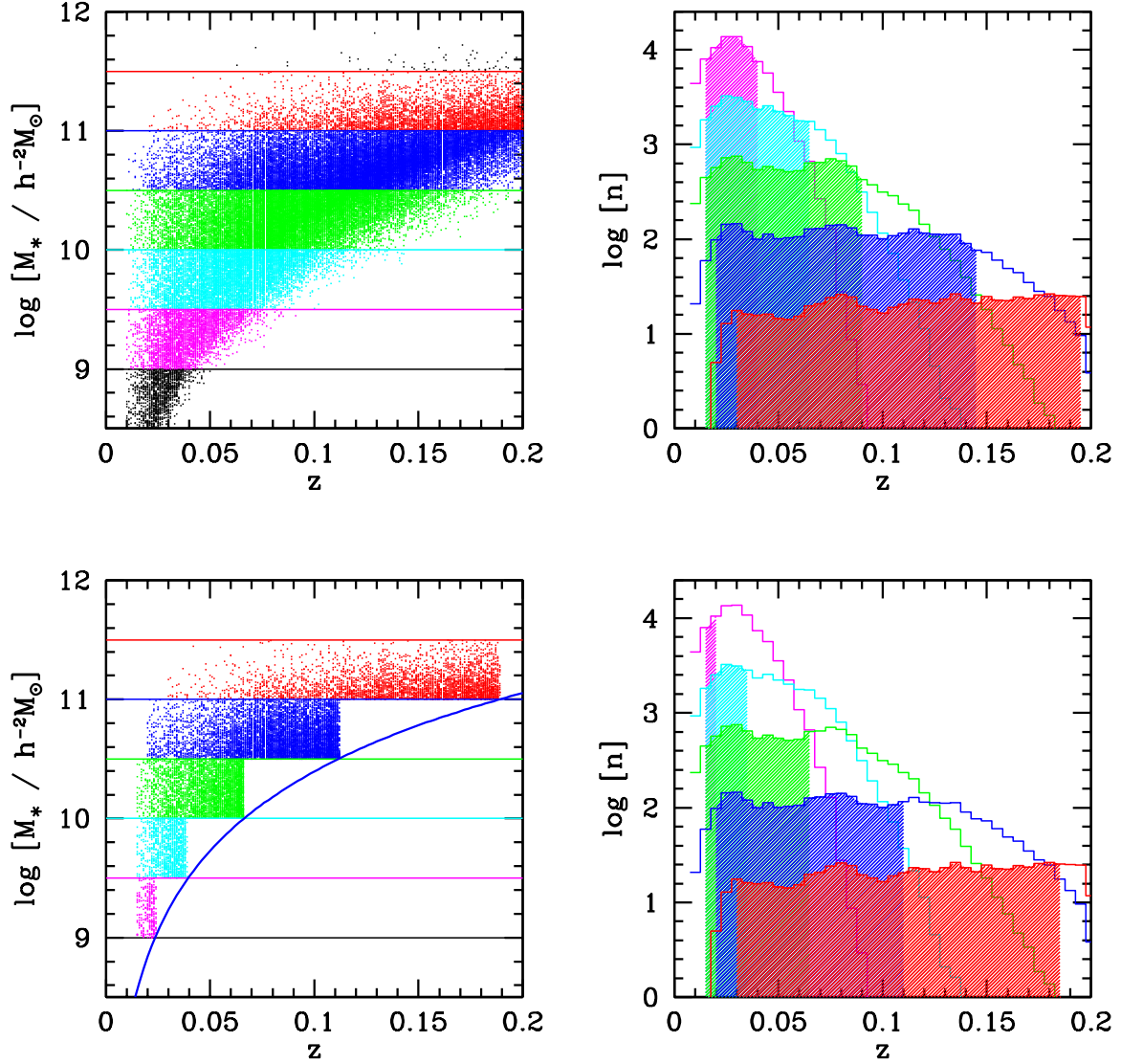
FIG. 19.— The distributions of stellar mass versus redshift for galaxies in the SDSS DR7 (left-hand panels), and the number density distribution of these galaxies as a function of redshift (right-hand panels). Galaxies within five stellar mass bins are selected. The selection criteria for these five samples are specified using their redshift distributions (histograms and/or the shaded areas). See text for details regarding the constructions of these samples.

Since the SDSS galaxy sample is flux limited, red and blue galaxies of the same stellar mass suffer from different selection effects because of their different stellar mass-to-light ratios. Using conservative limits, van den Bosch et al. (2008) have shown that the stellar mass completeness limit as a function of redshift for the SDSS catalogue is given by

$$\log[M_{*,\mathrm{lim}}/(h^{-2}\,\mathrm{M_\odot})] = \frac{4.852 + 2.246\log D_L(z) + 1.123\log(1+z) - 1.186z}{1 - 0.067z} \ . \tag{A1}$$

Using this limit we also construct five samples in stellar mass that are 'complete'. The corresponding selection criteria are shown in the lower left-hand panel of Fig. 19, while the shaded areas in the lower right-hand panel indicate the corresponding number densities as function of redshift. In what follows we refer to these five samples as 'Volume2' samples.

To estimate the two-point correlation functions, one needs to construct random samples to normalize the galaxy-pair counts (see below). In order to take account of the overall selection effects in the SDSS catalogue, we first construct a random sample using the SDSS luminosity function and then apply various observational selection effects (magnitude limits, redshift completeness, sky boundary) according to the SDSS survey mask. Since galaxies in different stellar mass bin do not follow the overall luminosity function, we re-assign a redshift to each mock galaxy by randomly sampling the redshifts of the SDSS galaxies in the corresponding stellar mass bin. Hence, the random samples have exactly the same redshift distributions as their corresponding SDSS samples. By applying the same redshift cuts, we obtain the random samples for the 'Mass-limited', 'Volume1' and 'Volume2' galaxy samples, respectively.
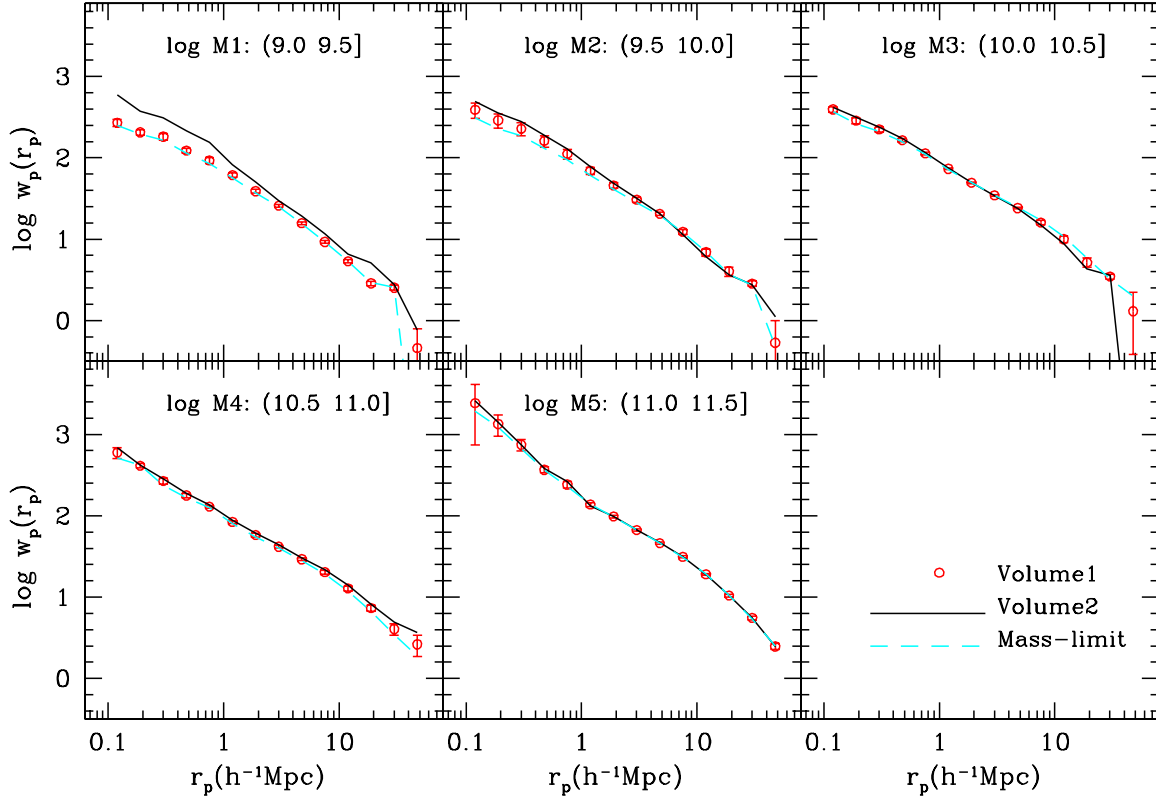
FIG. 20.— The projected 2PCFs of galaxies in different stellar mass bins, as indicated by the $\log[M_*/(h^{-2}\,M_\odot)]$-values in brackets. Open circles with error bars are the results for the Volume1 samples. Solid and dashed lines show the results for the Volume2 samples and Mass-limited samples, respectively.

TABLE 5
THE PROJECTED 2PCFS MEASURED FROM THE SDSS DR7 WITHIN DIFFERENT STELLAR MASS BINS.

ID	r_p	$w_p(r_p)$	σ_{w_p}	$w_p(r_p)$	σ_{w_p}	$w_p(r_p)$	σ_{w_p}	$w_p(r_p)$	σ_{w_p}	$w_p(r_p)$	σ_{w_p}
(1)	(2)	(3)	(4)	(5)	(6)	(7)	(8)	(9)	(10)	(11)	(12)
		[9.0, 9.5]		[9.5, 10.0]		[10.0, 10.5]		[10.5, 11.0]		[11.0, 11.5]	
1	0.12	373.399	200.617	388.815	83.198	393.234	30.913	597.466	90.192	2423.422	1684.429
2	0.19	259.170	92.989	288.384	55.778	287.154	25.668	411.860	24.702	1340.480	391.143
3	0.30	221.851	69.188	228.047	40.157	223.528	14.039	267.002	23.886	746.369	123.150
4	0.48	152.048	46.861	161.172	25.446	164.613	7.819	177.249	10.115	366.864	30.737
5	0.75	112.231	32.711	111.791	14.929	113.182	3.683	129.185	5.566	241.362	21.748
6	1.20	67.752	12.318	69.407	7.387	73.073	1.938	83.692	3.573	137.289	7.388
7	1.90	42.485	6.752	45.751	3.630	49.318	0.960	57.954	2.935	98.301	3.801
8	3.01	27.063	2.678	30.453	2.027	34.459	0.776	41.691	1.673	66.697	2.229
9	4.77	16.820	1.987	20.490	0.995	24.065	0.617	29.157	1.126	45.976	1.532
10	7.55	10.066	1.942	12.326	0.888	15.995	0.983	20.199	1.041	31.164	0.951
11	11.97	5.762	0.959	6.884	0.677	9.983	0.895	12.782	0.942	18.996	0.569
12	18.97	3.637	1.183	4.021	0.539	5.171	0.673	7.316	0.618	10.485	0.414
13	30.07	2.613	0.369	2.850	0.229	3.470	0.229	4.050	0.647	5.545	0.297
14	47.66	0.486	0.448	0.532	0.463	1.306	0.922	2.619	0.762	2.473	0.213

NOTE. — Column (1): a counting ID. Column (2): the projected comoving distances in unit of h^{-1}Mpc. Column (3-12): the projected 2PCFs, $w_p(r_p)$, and their errors, σ_{w_p}, for galaxies in different stellar mass bins, as indicated (in terms of $\log(M_*/\,h^{-2}M_\odot)$).

A.2. The estimator of the two-point correlation function and the results

We estimate the two-point correlation function (2PCF), $\xi(r_p, r_\pi)$, for galaxies in each sample using the following estimator,

$$\xi(r_p, r_\pi) = \frac{\langle RR \rangle \langle DD \rangle}{\langle DR \rangle^2} - 1 \,, \tag{A2}$$

where $\langle DD \rangle$, $\langle RR \rangle$, and $\langle DR \rangle$ are, respectively, the number of galaxy-galaxy, random-random, and galaxy-random pairs with separation (r_{p}, r_π) (Hamilton 1993). The variables r_{p} and r_π are the pair separations perpendicular and parallel to the line-of-sight, respectively. Explicitly, for a pair of galaxies, one located at $\mathbf{s_1}$ and the other at $\mathbf{s_2}$ with $\mathbf{s_i} = c z_i \hat{\mathbf{r_i}}/H_0$, we define

$$ r_\pi = \frac{\mathbf{s} \cdot \mathbf{l}}{|\mathbf{l}|} , \qquad r_{\mathrm{p}} = \sqrt{\mathbf{s} \cdot \mathbf{s} - \pi^2} , \tag{A3} $$

where $\mathbf{l} = (\mathbf{s_1} + \mathbf{s_2})/2$ is the line of sight intersecting the pair, and $\mathbf{s} = \mathbf{s_1} - \mathbf{s_2}$. Since redshift-space distortions only affect r_π, the projection of $\xi(r_{\mathrm{p}}, r_\pi)$ along the r_π axis is not sensitive to peculiar velocities, and directly related to the real-space correlation function. This projected 2PCF, $w_{\mathrm{p}}(r_{\mathrm{p}})$, is estimated using

$$ w_{\mathrm{p}}(r_{\mathrm{p}}) = \int_{-\infty}^{\infty} \xi(r_{\mathrm{p}}, r_\pi)\, \mathrm{d}r_\pi = 2 \sum_k \xi(r_{\mathrm{p}}, r_\pi)\, \Delta r_\pi \tag{A4} $$

(Davis & Peebles 1983). In our analysis, the summation is made over $k = 1$ to 40, which, for our adopted bin width of $\Delta r_\pi = 1\, h^{-1} \mathrm{Mpc}$, corresponds to an integration from $r_\pi = 0\, h^{-1} \mathrm{Mpc}$ to $r_\pi = 40\, h^{-1} \mathrm{Mpc}$. In order to obtain the error bars and the covariance matrix for the projected 2PCFs, we use 200 bootstrap resamplings of the galaxies in consideration. The covariance matrix is obtained using

$$ \mathbf{C}_{ij} \equiv \mathrm{Cov}(w_{p,i}, w_{p,j}) = \frac{1}{N-1} \sum_{l=1}^{N} (w_{p,i}^l - \bar{w}_{p,i})(w_{p,j}^l - \bar{w}_{p,j}), \tag{A5} $$

where $N = 200$, and $w_{p,i}^l$ represents the value of the projected 2PCF of the ith bin in the lth resampling.

The projected 2PCFs $w_{\mathrm{p}}(r_{\mathrm{p}})$ for all the galaxy samples described above are shown in Fig. 20, with different panels corresponding to galaxies in different stellar mass bins, as indicated. Open circles with error bars correspond to the 'Volume1' samples, while solid and dashed lines correspond to the 'Volume2' and 'Mass-limited' samples, respectively. Note that the results for the same stellar mass bin are very similar regardless of the sample used, except in the lowest stellar mass bin. The big difference between the 'Volume2' from other samples in the lowest stellar mass bin is probably produced by the fact that the excess galaxies in other samples are mainly blue galaxies which are relatively bright. In general, 'Volume2' sample is unbiased with respect to galaxy color, however suffer more severely from the survey volume effect. Therefore, for our model constraints in the main text, we obtain the averaged projected 2PCFs over the 'Volume1', 'Volume2' and 'Mass-limited' samples. The resulting covariance matrixes are updated using the total 600 bootstrap resampling values as well. Thus obtained values of $w_{\mathrm{p}}(r_{\mathrm{p}})$ are listed in Table 5. The related covariance matrixes are available from the authors upon request. As we have tested, our results are in good agreement with those obtained by Li et al. (2006) from the SDSS DR2 data and those obtained by Guo et al. (2011) from the SDSS DR7 data, which are based on stellar masses estimated from galaxy spectra and photometries, respectively. For consistency with our stellar mass functions, which are all based on the stellar masses obtained using the model of Bell et al. (2003), we use our own measurements of $w_{\mathrm{p}}(r_{\mathrm{p}})$ together with the covariance matrixes based on the same stellar masses.

B. THE STELLAR MASS FUNCTIONS AND CONDITIONAL STELLAR MASS FUNCTIONS MEASURED FROM SDSS DR7

We have constructed group catalogues from the latest SDSS DR7 using the same method described in Yang et al. (2007) [6]. Here we provide the updated stellar mass functions and conditional stellar mass functions obtained from these group catalogues. Readers are referred to Yang et al. (2009b) for the details of these measurements.

Listed in Table 6 are the stellar mass functions of galaxies. Galaxies are classified into three categories according to their memberships in groups: all galaxies (ALL), central galaxies (CENTRAL) and satellites (SATELLITE). For galaxies in each category , results are provided for all galaxies (all), red galaxies (red) and blue galaxies (blue), using the same color separation as in Yang et al. (2009b).

For the present paper, investigation in this study, only data for all galaxies in 'ALL' groups are used. This stellar mass function is shown in Fig. 2 as open circles with error bars. Fitting the observational data with the Schechter function,

$$ \Phi(M_*) = \phi^\star \left(\frac{M_*}{M^\star} \right)^{(\alpha+1)} \exp\left[-\frac{M_*}{M^\star} \right] , \tag{B1} $$

we obtain the best fit parameters, $\phi^\star = 0.0083635$, $\alpha = -1.117$, and $\log M^\star = 10.673$. The best fit is shown as the solid line in Fig. 2.

Listed in Table 7 are the conditional stellar mass functions of galaxies. Here halo masses are obtained assuming the mass function of the WMAP7 cosmology.

REFERENCES

[6] See also Yang et al. (2012, in preparation)

Abazajian, K. N., et al. 2005, AJ, 129, 1755
Abazajian, K. N., et al. 2009, ApJS, 182, 543
Adelman-McCarthy, J. K., et al. 2006, ApJS, 162, 38

TABLE 6
THE GALAXY STELLAR MASS FUNCTIONS $\Phi(M_*)$

(1) log M_*	ALL			CENTRAL			SATELLITE		
	(2) all	(3) red	(4) blue	(5) all	(6) red	(7) blue	(8) all	(9) red	(10) blue
8.2	3.7705 ± 1.5258	0.9436 ± 0.7870	2.8269 ± 1.2665	3.0870 ± 1.6328	0.9436 ± 0.7870	2.1434 ± 1.3832	0.6835 ± 0.9345	0.0000 ± 0.0000	0.6835 ± 0.9345
8.3	3.4598 ± 0.7363	1.2416 ± 0.4523	2.2182 ± 0.5867	2.1801 ± 0.5884	0.6520 ± 0.3011	1.5281 ± 0.4684	1.2796 ± 0.5566	0.5896 ± 0.3436	0.6900 ± 0.4418
8.4	4.1293 ± 0.5891	1.1804 ± 0.2965	2.9489 ± 0.4627	2.7961 ± 0.4415	0.5128 ± 0.2023	2.2833 ± 0.3748	1.3332 ± 0.4736	0.6676 ± 0.2879	0.6656 ± 0.2905
8.5	3.6421 ± 0.5547	0.9305 ± 0.2886	2.7116 ± 0.3771	2.4913 ± 0.3387	0.4905 ± 0.1597	2.0008 ± 0.2727	1.1508 ± 0.3368	0.4400 ± 0.1997	0.7108 ± 0.2176
8.6	3.3055 ± 0.4245	0.8003 ± 0.2345	2.5052 ± 0.2674	2.2182 ± 0.2612	0.3709 ± 0.1511	1.8474 ± 0.2058	1.0873 ± 0.2604	0.4294 ± 0.1365	0.6578 ± 0.1831
8.7	3.1321 ± 0.3100	0.8215 ± 0.1561	2.3106 ± 0.2224	2.1598 ± 0.2294	0.3756 ± 0.1010	1.7842 ± 0.1819	0.9723 ± 0.1686	0.4459 ± 0.1020	0.5264 ± 0.1109
8.8	3.0391 ± 0.2499	0.8716 ± 0.1181	2.1675 ± 0.1865	1.8100 ± 0.1428	0.3005 ± 0.0669	1.5095 ± 0.1253	1.2291 ± 0.1729	0.5711 ± 0.0936	0.6580 ± 0.1253
8.9	2.7949 ± 0.2433	0.8404 ± 0.1442	1.9545 ± 0.1538	1.7266 ± 0.1265	0.2997 ± 0.0582	1.4269 ± 0.1027	1.0683 ± 0.1745	0.5407 ± 0.1141	0.5276 ± 0.0929
9.0	3.1430 ± 0.1822	0.9815 ± 0.1210	2.1614 ± 0.1161	1.9179 ± 0.0875	0.3476 ± 0.0524	1.5702 ± 0.0968	1.2251 ± 0.1483	0.6339 ± 0.0941	0.5912 ± 0.0871
9.1	3.1047 ± 0.2357	1.0438 ± 0.1518	2.0609 ± 0.1199	1.8162 ± 0.1129	0.3595 ± 0.0608	1.4568 ± 0.0765	1.2884 ± 0.1579	0.6843 ± 0.1131	0.6042 ± 0.0723
9.2	2.9365 ± 0.1816	1.0557 ± 0.1398	1.8808 ± 0.0760	1.6895 ± 0.1021	0.3411 ± 0.0622	1.3484 ± 0.0606	1.2470 ± 0.1151	0.7146 ± 0.0969	0.5324 ± 0.0409
9.3	2.8092 ± 0.1786	1.0230 ± 0.1329	1.7861 ± 0.0766	1.5992 ± 0.0730	0.3624 ± 0.0458	1.2368 ± 0.0476	1.2100 ± 0.1358	0.6607 ± 0.1043	0.5493 ± 0.0518
9.4	2.8013 ± 0.0925	1.0764 ± 0.0703	1.7249 ± 0.0477	1.6116 ± 0.0621	0.4012 ± 0.0381	1.2104 ± 0.0420	1.1897 ± 0.0549	0.6753 ± 0.0479	0.5145 ± 0.0292
9.5	2.5093 ± 0.1140	1.0816 ± 0.0917	1.4277 ± 0.0418	1.4360 ± 0.0522	0.4290 ± 0.0420	1.0070 ± 0.0354	1.0733 ± 0.0804	0.6526 ± 0.0637	0.4208 ± 0.0290
9.6	2.3481 ± 0.1002	1.0112 ± 0.0787	1.3369 ± 0.0362	1.3756 ± 0.0508	0.4339 ± 0.0302	0.9416 ± 0.0307	0.9725 ± 0.0653	0.5772 ± 0.0598	0.3953 ± 0.0173
9.7	2.0970 ± 0.0640	1.0132 ± 0.0488	1.0837 ± 0.0286	1.2562 ± 0.0420	0.4760 ± 0.0288	0.7802 ± 0.0231	0.8408 ± 0.0368	0.5373 ± 0.0304	0.3035 ± 0.0153
9.8	1.9927 ± 0.0653	1.0453 ± 0.0526	0.9473 ± 0.0239	1.2189 ± 0.0254	0.5060 ± 0.0210	0.7129 ± 0.0171	0.7738 ± 0.0509	0.5393 ± 0.0407	0.2345 ± 0.0168
9.9	1.8551 ± 0.0555	1.0426 ± 0.0446	0.8125 ± 0.0210	1.1423 ± 0.0240	0.5284 ± 0.0176	0.6139 ± 0.0143	0.7128 ± 0.0398	0.5142 ± 0.0337	0.1986 ± 0.0119
10.0	1.7485 ± 0.0555	1.0329 ± 0.0448	0.7156 ± 0.0184	1.1068 ± 0.0241	0.5713 ± 0.0197	0.5355 ± 0.0110	0.6417 ± 0.0393	0.4616 ± 0.0320	0.1801 ± 0.0119
10.1	1.6715 ± 0.0430	1.0297 ± 0.0343	0.6418 ± 0.0156	1.0844 ± 0.0161	0.5863 ± 0.0100	0.4981 ± 0.0121	0.5871 ± 0.0326	0.4434 ± 0.0293	0.1436 ± 0.0066
10.2	1.6340 ± 0.0417	1.0560 ± 0.0331	0.5780 ± 0.0142	1.0963 ± 0.0122	0.6465 ± 0.0088	0.4498 ± 0.0082	0.5377 ± 0.0346	0.4095 ± 0.0289	0.1282 ± 0.0087
10.3	1.5273 ± 0.0419	1.0368 ± 0.0355	0.4905 ± 0.0113	1.0326 ± 0.0104	0.6491 ± 0.0078	0.3835 ± 0.0069	0.4947 ± 0.0356	0.3877 ± 0.0318	0.1071 ± 0.0064
10.4	1.3308 ± 0.0339	0.9331 ± 0.0266	0.3978 ± 0.0105	0.9275 ± 0.0104	0.6129 ± 0.0081	0.3146 ± 0.0067	0.4033 ± 0.0273	0.3202 ± 0.0232	0.0831 ± 0.0057
10.5	1.0870 ± 0.0292	0.7817 ± 0.0237	0.3052 ± 0.0084	0.7882 ± 0.0095	0.5383 ± 0.0066	0.2499 ± 0.0051	0.2988 ± 0.0225	0.2435 ± 0.0193	0.0553 ± 0.0045
10.6	0.8692 ± 0.0265	0.6337 ± 0.0210	0.2354 ± 0.0077	0.6445 ± 0.0097	0.4523 ± 0.0069	0.1922 ± 0.0047	0.2247 ± 0.0194	0.1814 ± 0.0164	0.0432 ± 0.0040
10.7	0.6629 ± 0.0208	0.4876 ± 0.0164	0.1753 ± 0.0061	0.5122 ± 0.0089	0.3643 ± 0.0064	0.1479 ± 0.0039	0.1507 ± 0.0138	0.1232 ± 0.0116	0.0274 ± 0.0029
10.8	0.4749 ± 0.0168	0.3555 ± 0.0133	0.1194 ± 0.0045	0.3796 ± 0.0078	0.2776 ± 0.0056	0.1020 ± 0.0031	0.0953 ± 0.0101	0.0779 ± 0.0088	0.0173 ± 0.0019
10.9	0.3130 ± 0.0133	0.2368 ± 0.0104	0.0762 ± 0.0038	0.2598 ± 0.0083	0.1923 ± 0.0063	0.0675 ± 0.0029	0.0532 ± 0.0057	0.0445 ± 0.0047	0.0087 ± 0.0013
11.0	0.1913 ± 0.0086	0.1491 ± 0.0066	0.0422 ± 0.0026	0.1636 ± 0.0059	0.1260 ± 0.0044	0.0376 ± 0.0021	0.0277 ± 0.0032	0.0231 ± 0.0027	0.0046 ± 0.0007
11.1	0.1055 ± 0.0056	0.0840 ± 0.0041	0.0215 ± 0.0019	0.0943 ± 0.0044	0.0745 ± 0.0031	0.0198 ± 0.0015	0.0112 ± 0.0015	0.0095 ± 0.0012	0.0016 ± 0.0004
11.2	0.0540 ± 0.0028	0.0447 ± 0.0021	0.0092 ± 0.0009	0.0495 ± 0.0023	0.0408 ± 0.0017	0.0087 ± 0.0008	0.0045 ± 0.0006	0.0039 ± 0.0006	0.0006 ± 0.0001
11.3	0.0245 ± 0.0015	0.0207 ± 0.0013	0.0039 ± 0.0004	0.0231 ± 0.0014	0.0194 ± 0.0011	0.0037 ± 0.0004	0.0015 ± 0.0002	0.0013 ± 0.0002	0.0001 ± 0.0001
11.4	0.0104 ± 0.0007	0.0086 ± 0.0006	0.0019 ± 0.0002	0.0101 ± 0.0006	0.0083 ± 0.0005	0.0018 ± 0.0002	0.0003 ± 0.0001	0.0003 ± 0.0001	0.0000 ± 0.0000
11.5	0.0042 ± 0.0003	0.0034 ± 0.0003	0.0008 ± 0.0001	0.0041 ± 0.0003	0.0033 ± 0.0003	0.0008 ± 0.0001	0.0001 ± 0.0000	0.0001 ± 0.0000	0.0000 ± 0.0000
11.6	0.0013 ± 0.0001	0.0010 ± 0.0001	0.0003 ± 0.0001	0.0013 ± 0.0001	0.0010 ± 0.0001	0.0003 ± 0.0001	0.0000 ± 0.0000	0.0000 ± 0.0000	0.0000 ± 0.0000
11.7	0.0003 ± 0.0001	0.0002 ± 0.0001	0.0001 ± 0.0000	0.0003 ± 0.0001	0.0002 ± 0.0001	0.0001 ± 0.0000	0.0000 ± 0.0000	0.0000 ± 0.0000	0.0000 ± 0.0000

NOTE. — Column (1): the median of the logarithm of the galaxy stellar mass with bin width $\Delta \log M_* = 0.05$. Column (2 - 4): the stellar mass functions of all, red and blue for 'ALL' group members. Column (5 - 7): the stellar mass functions of all, red and blue for 'CENTRAL' group members. Column (8 - 10): the stellar mass functions of all, red and blue for 'SATELLITE' group members. Note that all the galaxy stellar mass functions listed in this table are in units of $10^{-2} h^3 \mathrm{Mpc}^{-3} \mathrm{d} \log M_*$, where log is the 10 based logarithm.

Yang et al.

TABLE 7
THE CONDITIONAL STELLAR MASS FUNCTIONS OF GALAXIES $\Phi(M_*|M_h)$

(1) $\log M_*$	(2) [12.1, 12.4]	(3) [12.4, 12.7]	(4) [12.7, 13.0]	(5) [13.0, 13.3]	(6) [13.3, 13.6]	(7) [13.6, 13.9]	(8) [13.9, 14.2]	(9) [14.2, 14.5]	(10) > 14.5
8.9	0.857 ± 0.238	1.534 ± 0.558	3.944 ± 1.745	7.232 ± 3.599	0.000 ± 0.000	0.000 ± 0.000	0.000 ± 0.000	0.000 ± 0.000	0.000 ± 0.000
9.0	0.867 ± 0.191	1.793 ± 0.364	2.569 ± 0.723	7.962 ± 1.834	10.542 ± 4.496	19.005 ± 6.481	38.365 ± 10.604	120.947 ± 91.664	0.000 ± 0.000
9.1	0.860 ± 0.138	1.117 ± 0.237	2.984 ± 0.662	7.154 ± 1.573	12.582 ± 4.204	22.436 ± 4.295	44.760 ± 17.909	105.092 ± 53.583	232.801 ± 187.113
9.2	0.740 ± 0.099	1.353 ± 0.209	2.221 ± 0.437	6.045 ± 0.845	11.677 ± 3.663	20.303 ± 4.000	35.106 ± 10.618	120.722 ± 59.000	273.560 ± 191.005
9.3	0.626 ± 0.080	1.278 ± 0.180	2.412 ± 0.321	4.447 ± 0.903	7.831 ± 1.935	19.684 ± 3.393	37.028 ± 9.060	114.475 ± 54.627	240.362 ± 124.617
9.4	0.572 ± 0.071	1.252 ± 0.136	3.118 ± 0.316	4.153 ± 0.540	8.288 ± 1.085	20.259 ± 2.992	39.099 ± 8.065	100.398 ± 30.349	268.824 ± 134.078
9.5	0.476 ± 0.057	1.064 ± 0.110	2.034 ± 0.222	4.965 ± 0.653	9.177 ± 1.263	21.391 ± 2.823	37.373 ± 4.539	87.398 ± 26.248	251.692 ± 57.480
9.6	0.522 ± 0.054	0.991 ± 0.093	2.512 ± 0.218	4.064 ± 0.455	8.755 ± 1.012	16.330 ± 1.757	33.938 ± 5.091	94.456 ± 22.537	188.324 ± 47.538
9.7	0.414 ± 0.037	0.873 ± 0.078	1.691 ± 0.160	3.553 ± 0.382	6.781 ± 1.065	15.900 ± 1.777	41.002 ± 4.031	85.229 ± 17.790	206.746 ± 46.094
9.8	0.419 ± 0.046	0.817 ± 0.088	1.700 ± 0.138	3.288 ± 0.283	7.694 ± 0.865	14.748 ± 1.399	36.148 ± 3.253	78.295 ± 13.852	170.928 ± 37.206
9.9	0.401 ± 0.028	0.802 ± 0.055	1.733 ± 0.133	2.959 ± 0.243	7.274 ± 1.067	16.538 ± 1.313	38.849 ± 5.484	78.331 ± 10.478	163.676 ± 24.944
10.0	0.339 ± 0.052	0.766 ± 0.057	1.598 ± 0.104	2.983 ± 0.197	6.379 ± 0.630	15.380 ± 1.293	30.516 ± 2.681	71.385 ± 8.285	154.757 ± 21.411
10.1	0.283 ± 0.055	0.673 ± 0.037	1.388 ± 0.073	3.167 ± 0.173	6.209 ± 0.453	13.795 ± 0.807	30.357 ± 2.111	67.792 ± 8.082	133.214 ± 26.301
10.2	0.176 ± 0.040	0.610 ± 0.039	1.391 ± 0.079	2.850 ± 0.133	5.491 ± 0.486	13.024 ± 0.811	26.062 ± 2.053	60.936 ± 5.756	117.930 ± 16.417
10.3	0.088 ± 0.034	0.547 ± 0.098	1.300 ± 0.097	2.473 ± 0.147	5.500 ± 0.242	11.631 ± 0.710	23.506 ± 1.265	48.402 ± 4.657	109.039 ± 10.113
10.4	0.010 ± 0.013	0.357 ± 0.061	1.077 ± 0.071	2.332 ± 0.130	4.577 ± 0.218	10.016 ± 0.700	20.390 ± 1.332	45.767 ± 4.143	103.090 ± 8.596
10.5	0.002 ± 0.002	0.113 ± 0.039	0.828 ± 0.120	1.918 ± 0.094	3.793 ± 0.199	8.246 ± 0.323	16.756 ± 1.288	35.299 ± 3.344	76.226 ± 6.337
10.6	0.000 ± 0.001	0.014 ± 0.017	0.418 ± 0.078	1.546 ± 0.158	3.206 ± 0.217	6.514 ± 0.337	12.571 ± 0.726	24.642 ± 1.687	60.269 ± 5.612
10.7	0.001 ± 0.003	0.001 ± 0.002	0.094 ± 0.048	0.843 ± 0.154	2.318 ± 0.197	4.879 ± 0.407	9.591 ± 0.418	19.094 ± 1.294	42.580 ± 3.151
10.8	0.002 ± 0.004	0.000 ± 0.000	0.005 ± 0.009	0.295 ± 0.073	1.433 ± 0.201	3.261 ± 0.261	7.104 ± 0.555	13.486 ± 0.764	27.614 ± 1.719
10.9	0.013 ± 0.016	0.002 ± 0.003	0.001 ± 0.001	0.036 ± 0.025	0.583 ± 0.104	1.891 ± 0.255	4.694 ± 0.363	9.536 ± 0.396	19.100 ± 1.067
11.0	0.032 ± 0.036	0.004 ± 0.004	0.000 ± 0.000	0.003 ± 0.004	0.117 ± 0.043	0.991 ± 0.189	2.748 ± 0.289	6.312 ± 0.364	13.341 ± 0.736
11.1	0.109 ± 0.106	0.014 ± 0.017	0.001 ± 0.003	0.000 ± 0.000	0.005 ± 0.005	0.233 ± 0.062	1.201 ± 0.143	3.402 ± 0.489	9.205 ± 0.568
11.2	0.341 ± 0.247	0.052 ± 0.047	0.009 ± 0.010	0.001 ± 0.005	0.001 ± 0.002	0.021 ± 0.015	0.296 ± 0.071	1.387 ± 0.188	5.054 ± 0.459
11.3	0.740 ± 0.421	0.143 ± 0.105	0.029 ± 0.025	0.007 ± 0.008	0.000 ± 0.000	0.003 ± 0.003	0.034 ± 0.018	0.277 ± 0.061	2.132 ± 0.290
11.4	1.817 ± 0.184	0.471 ± 0.161	0.108 ± 0.071	0.028 ± 0.020	0.005 ± 0.008	0.001 ± 0.002	0.000 ± 0.000	0.026 ± 0.022	0.704 ± 0.168
11.5	3.559 ± 0.827	1.043 ± 0.291	0.342 ± 0.143	0.121 ± 0.055	0.017 ± 0.019	0.000 ± 0.000	0.004 ± 0.006	0.017 ± 0.018	0.210 ± 0.089
11.6	2.973 ± 0.558	1.889 ± 0.352	0.869 ± 0.154	0.351 ± 0.140	0.123 ± 0.048	0.050 ± 0.025	0.000 ± 0.000	0.000 ± 0.000	0.000 ± 0.000
11.7	0.511 ± 0.489	3.753 ± 0.869	1.629 ± 0.224	0.940 ± 0.162	0.410 ± 0.135	0.141 ± 0.051	0.021 ± 0.019	0.005 ± 0.023	0.000 ± 0.000
11.8	0.052 ± 0.060	2.449 ± 0.269	2.606 ± 0.293	1.687 ± 0.139	0.961 ± 0.166	0.482 ± 0.123	0.162 ± 0.064	0.013 ± 0.023	0.000 ± 0.000
11.9	0.009 ± 0.010	0.294 ± 0.287	3.360 ± 0.650	2.320 ± 0.133	1.854 ± 0.116	1.112 ± 0.171	0.551 ± 0.106	0.183 ± 0.058	0.009 ± 0.035
12.0	0.003 ± 0.003	0.030 ± 0.034	1.158 ± 0.200	2.866 ± 0.491	2.449 ± 0.059	1.997 ± 0.137	1.336 ± 0.140	0.597 ± 0.130	0.080 ± 0.067
12.1	0.000 ± 0.001	0.007 ± 0.008	0.082 ± 0.089	1.769 ± 0.303	2.381 ± 0.219	2.533 ± 0.069	2.298 ± 0.207	1.613 ± 0.120	0.785 ± 0.150
12.2	0.000 ± 0.000	0.002 ± 0.003	0.012 ± 0.013	0.227 ± 0.110	1.732 ± 0.321	2.107 ± 0.085	2.310 ± 0.090	2.360 ± 0.141	1.481 ± 0.197
12.3	0.000 ± 0.000	0.000 ± 0.001	0.006 ± 0.007	0.021 ± 0.023	0.432 ± 0.107	1.410 ± 0.266	1.791 ± 0.114	2.135 ± 0.141	2.194 ± 0.226
12.4	0.000 ± 0.000	0.000 ± 0.000	0.001 ± 0.001	0.004 ± 0.005	0.034 ± 0.026	0.527 ± 0.083	1.189 ± 0.176	1.659 ± 0.132	2.157 ± 0.223
12.5	0.000 ± 0.000	0.000 ± 0.000	0.001 ± 0.001	0.002 ± 0.003	0.009 ± 0.010	0.069 ± 0.036	0.445 ± 0.132	1.023 ± 0.140	1.674 ± 0.217
12.6	0.000 ± 0.000	0.000 ± 0.000	0.000 ± 0.000	0.001 ± 0.002	0.003 ± 0.004	0.011 ± 0.007	0.091 ± 0.020	0.418 ± 0.077	1.007 ± 0.174
12.7	0.000 ± 0.000	0.000 ± 0.000	0.000 ± 0.000	0.000 ± 0.000	0.001 ± 0.001	0.001 ± 0.002	0.007 ± 0.007	0.046 ± 0.023	0.445 ± 0.124
12.8	0.000 ± 0.000	0.000 ± 0.000	0.000 ± 0.000	0.000 ± 0.000	0.000 ± 0.000	0.001 ± 0.002	0.003 ± 0.005	0.005 ± 0.011	0.128 ± 0.081
12.9	0.000 ± 0.000	0.000 ± 0.000	0.000 ± 0.000	0.000 ± 0.000	0.000 ± 0.000	0.000 ± 0.000	0.000 ± 0.000	0.000 ± 0.000	0.014 ± 0.029
13.0	0.000 ± 0.000	0.000 ± 0.000	0.000 ± 0.000	0.000 ± 0.000	0.000 ± 0.000	0.000 ± 0.000	0.000 ± 0.000	0.000 ± 0.000	0.028 ± 0.043

NOTE. — Column (1): the median of the logarithm of the galaxy stellar mass with bin width $\Delta \log M_* = 0.05$. Column (2 - 10): the conditional stellar mass functions in halos of different mass ranges as indicated. The average halo masses in these bins are $\log < M_h >= 12.26, 12.55, 12.85, 13.15, 13.44, 13.74, 14.04, 14.33, 14.72$, respectively. Note that all the conditioanl galaxy stellar mass functions listed in this table are in units of $d \log M_*$, where log is the 10 based logarithm. Here results are listed for satellite (upper part) and central (lower part) galaxies separately, which can be distinguished with zero measurements. Note here the stellar masses for central galaxies should be converted using $\log M_{*,c} = \log M_* - 1.0$.

Avila-Reese, V., & Firmani, C. 2011, Revista Mexicana de Astronomia y Astrofisica Conference Series, 40, 27

Avila-Reese, V., Colín, P., González-Samaniego, A., et al. 2011, ApJ, 736, 134

Behroozi, P. S., Conroy, C., & Wechsler, R. H. 2010, ApJ, 717, 379

Bell, E. F., McIntosh, D. H., Katz, N., & Weinberg, M. D. 2003, ApJS, 149, 289

Belokurov, V., et al. 2007, ApJ, 654, 897

Benson, A. J., Bower, R. G., Frenk, C. S., Lacey, C. G., Baugh, C. M., & Cole, S. 2003, ApJ, 599, 38

Birnboim, Y., & Dekel, A. 2003, MNRAS, 345, 349

Birnboim, Y., Dekel, A., & Neistein, E. 2007, MNRAS, 380, 339

Birnboim, Y., & Dekel, A. 2011, MNRAS, 415, 2566

Blanton, M. R., et al. 2003, ApJ, 592, 819

Blanton, M. R., et al. 2005, AJ, 129, 2562

Blanton, M. R., & Roweis, S. 2007, AJ, 133, 734

Bond, J. R., Cole, S., Efstathiou, G., & Kaiser, N. 1991, ApJ, 379, 440

Borch A., et al., 2006, A&A, 453, 869

Bouché, N., et al. 2010, ApJ, 718, 1001

Bouwens, R. J., et al. 2011, ApJ, 737, 90

Bower, R. G., Benson, A. J., Malbon, R., Helly, J. C., Frenk, C. S., Baugh, C. M., Cole, S., & Lacey, C. G. 2006, MNRAS, 370, 645

Boylan-Kolchin, M., Ma, C.-P., & Quataert, E. 2008, MNRAS, 383, 93

Boylan-Kolchin, M., Bullock, J. S., & Kaplinghat, M. 2011, MNRAS, 415, 40

Brown, M. J. I., et al. 2008, ApJ, 682, 937

Bryan, G. L., & Norman, M. L., 1998, ApJ, 495, 80

Bullock J.S., Kolatt T.S., Sigad Y., Somerville R.S., Klypin A.A., Primack J.R., Dekel A., 2001, MNRAS, 321, 559

Bullock, J. S., Wechsler, R. H., Somerville, R. S. 2002, MNRAS, 329, 246

Busha, M. T., Wechsler, R. H., Behroozi, P. S., et al. 2011, ApJ, 743, 117

Cacciato M., van den Bosch F.C., More S. Li R., Mo H.J., Yang X., 2009, MNRAS, 394, 929

Cattaneo, A., Dekel, A., DeVriendt, J., Guiderdoni, B., & Blaizot, J., 2006, MNRAS, 370, 1651

Ciotti, L., & Ostriker, J. P. 1997, ApJ, 487, L105

Coil, A. L., Newman, J. A., Cooper,M. C., Davis, M., Faber, S.M., Koo, D. C., Willmer, C. N. A., 2006, ApJ, 644, 671

Cole, S., Lacey, C. G., Baugh, C. M., & Frenk, C. S. 2000, MNRAS, 319, 168

Cole, S., Helly, J., Frenk, C. S., & Parkinson, H. 2008, MNRAS, 383, 546

Colless M., et al., 2001, MNRAS, 328, 1039

Conroy, C., et al. 2005, ApJ, 635, 982

Conroy, C., Wechsler, R. H., & Kravtsov, A. V. 2006, ApJ, 647, 201

Conroy, C., et al. 2007, ApJ, 654, 153

Conroy, C., Ho, S., & White, M. 2007, MNRAS, 379, 1491

Conroy, C., Wechsler, R. H., & Kravtsov, A. V. 2007, ApJ, 668, 826

Conroy, C., & Wechsler, R. H. 2009, ApJ, 696, 620

Conroy, C., Gunn, J. E., & White, M. 2009, ApJ, 699, 486

Cooray, A. 2005, MNRAS, 364, 303

Cooray, A. 2006, MNRAS, 365, 842

Cooray, A., Ouchi, M., 2006, MNRAS, 369, 1869

Croton, D. J., et al. 2006, MNRAS, 365, 11

Daddi, E., et al. 2003, ApJ, 588, 50

Davis M., Peebles P.J.E., 1983, ApJ, 267, 465

Davis M., Efstathiou G., Frenk C.S., White S.D.M., 1985, ApJ, 292, 371

Davis M., et al. 2003, Proc. SPIE, 4834, 161

Dekel, A., & Silk, J. 1986, ApJ, 303, 39

Dekel, A., & Birnboim, Y. 2008, MNRAS, 383, 119

de la Torre S., et al, 2010, MNRAS, in press

De Lucia G., et al., 2004, MNRAS, 348, 333

Diemand J., Kuhlen M., Madau P., 2007, ApJ, 667, 859

Drory, N., Salvato, M., Gabasch, A., Bender, R., Hopp, U., Feulner, G., & Pannella, M. 2005, ApJ, 619, L131

Dunkley, J., Bucher, M., Ferreira, P. G., Moodley, K., & Skordis, C. 2005, MNRAS, 356, 925

Dunkley, J., et al. 2009, ApJS, 180, 306

Dutton, A. A., van den Bosch, F. C., & Dekel, A. 2010, MNRAS, 405, 1690

Eke, V. R., Navarro, J. F., & Steinmetz, M. 2001, ApJ, 554, 114

Eke, V. R., et al. 2004, MNRAS, 355, 769

Fabian, A. C. 2003, MNRAS, 344, L27

Fakhouri O., Ma C. P., 2008, MNRAS, 386, 577

Fakhouri, O., Ma, C.-P., & Boylan-Kolchin, M. 2010, MNRAS, 406, 2267

Firmani, C., & Avila-Reese, V. 2010, ApJ, 723, 755

Fontana A., et al., 2006, A&A, 459, 745

Foucaud S., Conselice C. J., Hartley W. G., Lane K. P., Bamford S. P., Almaini O., Bundy, K., 2010, MNRAS, 406, 147

Gao L., White S.D.M., Jenkins A., Stoehr F., Springel V., 2004, MNRAS, 355, 819

Giocoli C., Tormen G., van den Bosch F.C., 2008, MNRAS, 386, 2135

Gonzalez, A. H., Zaritsky, D., & Zabludoff, A. I. 2007, ApJ, 666, 147

González, V., Labbé, I., Bouwens, R. J., Illingworth, G., Franx, M., Kriek, M., & Brammer, G. B., 2010, ApJ, 713, 115

Guo, Q., White, S. D. M., Li, C., & Boylan-Kolchin, M. 2010, MNRAS, 404, 1111

Guo, Q., White, S., Boylan-Kolchin, M., et al. 2011, MNRAS, 413, 101

Hamana, T., Yamada, T., Ouchi, M., Iwata, I., Kodama, T. 2006, MNRAS, 369, 1929

Hamilton A.J.S., 1993, ApJ, 417, 19

Han, J., Jing, Y. P., Wang, H., & Wang, W. 2011, arXiv:1103.2099

Henriques, B. M., Bertone, S., & Thomas, P. A. 2008, MNRAS, 383, 1649

Hirschmann, M., Naab, T., Somerville, R. S., Burkert, A., & Oser, L. 2012, MNRAS, 419, 3200

Hopkins, P. F., Hernquist, L., Cox, T. J., Di Matteo, T., Robertson, B., & Springel, V. 2006, ApJS, 163, 1

Jenkins A., Frenk C.S., White S.D.M., Colberg J.M. Cole S., Evrard A.E., Couchman H.M.P., Yoshida N., 2001, MNRAS, 321, 372

Jing Y. P., & Suto Y., 2000, ApJ, 529L, 69

Jing Y. P., & Suto Y., 2002, ApJ, 574, 538

Jing Y.P., Mo H.J., Börner G., 1998, ApJ, 494, 1

Kang, X., & van den Bosch, F. C. 2008, ApJ, 676, L101

Kauffmann G., et al., 2003, MNRAS, 341, 33

Kereš, D., Katz, N., Weinberg, D. H., & Davé, R. 2005, MNRAS, 363, 2

Khochfar, S., & Ostriker, J. P. 2008, ApJ, 680, 54

Kim, W.-T., & Narayan, R. 2003, ApJ, 596, 889

Klypin, A. A., Kravtsov, A. V., Valenzuela, O., & Prada, F. 1999, ApJ, 522, 82

Komatsu, E., et al. 2011, ApJS, 192, 18

Kroupa P., 2001, MNRAS, 322, 231

Krumholz, M. R., & Dekel, A. 2011, preprint (arXiv:1106.0301)

Labbé, I., et al. 2010a, ApJ, 708, 26

Labbé, I., et al. 2010b, ApJ, 716, 103

Lacey, C. G., & Cole, S. 1993, MNRAS, 262, 627

Lacey, C. G., Baugh, C. M., Frenk, C. S., & Benson, A. J. 2011, MNRAS, 412, 1828

Le Fevre O., et al. 2005, A&A, 439, 845

Leauthaud, A., Tinker, J., Behroozi, P. S., Busha, M. T., & Wechsler, R. H. 2011, ApJ, 738, 45

Leauthaud, A., Tinker, J., Bundy, K., et al. 2012, ApJ, 744, 159

Lee, K.,Giavalisco,M., Gnedin,O.Y., Somerville, R., Ferguson, H.,Dickinson,M., Ouchi, M., 2006, ApJ, 642, 63

Li C., Kauffmann G., Jing Y.P., White S. D. M., Boerner G., Cheng F.Z. 2006, MNRAS, 368, 21

Li C., White S.D.M., 2009, MNRAS, 398, 2177

Li Y., Mo H.J., 2009, preprint (arXiv:0908.0301)

Lilly S. J., et al. 2007, ApJS, 172, 70

Liu, L., Yang, X., Mo, H. J., van den Bosch, F. C., & Springel, V. 2010, ApJ, 712, 734

Lo Faro, B., Monaco, P., Vanzella, E., Fontanot, F., Silva, L., Cristiani, S. 2009, MNRAS, 399, 827

Macciò, A. V., Dutton, A. A., van den Bosch, F. C., Moore, B., Potter, D., & Stadel, J. 2007, MNRAS, 378, 55

Madau, P., Diemand, J., & Kuhlen, M. 2008, ApJ, 679, 1260

Mandelbaum, R., et al. 2005, MNRAS, 361, 1287

Mandelbaum, R., Seljak, U., Kauffmann, G., Hirata, C. M., & Brinkmann, J. 2006, MNRAS, 368, 715

Marchesini, D., van Dokkum, P. G., Förster Schreiber, N. M., Franx, M., Labbé, I., & Wuyts, S. 2009, ApJ, 701, 1765

McCracken H.J., Ilbert O., Mellier Y., Bertin E., Guzzo L., Arnouts S., Le F evre O., Zamorani G., 2008, A&A 479, 321

Meneux, B., et al. 2008, A&A, 478, 299

Meneux, B., et al. 2009, A&A, 505, 463

Mo, H. J., & Fukugita, M. 1996, ApJ, 467, L9

Mo, H. J., Mao, S., & White, S. D. M. 1999, MNRAS, 304, 175

Mo H. J., van den Bosch F. C., White S. D. M., 2010, Galaxy Formation and Evolution, Cambridge University Press

Mo H.J., White S.D.M., 1996, MNRAS, 282, 347

Mo H.J., White S.D.M., 2002, MNRAS, 336, 112

Mo, H. J., Yang, X., van den Bosch, F. C., & Katz, N. 2005, MNRAS, 363, 1155

Monaco, P., Murante, G., Borgani, S., & Fontanot, F. 2006, ApJ, 652, 89

Moore, B., Ghigna, S., Governato, F., Lake, G., Quinn, T., Stadel, J., & Tozzi, P. 1999, ApJ, 524, L19

More, S., van den Bosch, F. C., Cacciato, M., Mo, H. J., Yang, X., & Li R., 2009, MNRAS, 392, 801
More, S., van den Bosch, F. C., Cacciato, M., Skibba, R., Mo, H. J., & Yang, X. 2011, MNRAS, 410, 210
Moster, B. P., Somerville, R. S., Maulbetsch, C., van den Bosch, F. C., Macció, A. V.. Naab, T., & Oser, L. 2010, ApJ, 710, 903
Moustakas, L. A., & Somerville, R. S. 2002, ApJ, 577, 1
Naab, T., Johansson, P. H., & Ostriker, J. P. 2009, ApJ, 699, L178
Navarro, J. F., Frenk, C. S., & White, S. D. M. 1997, ApJ, 490, 493
Norberg, P., et al. 2002a, MNRAS, 332 827
Norberg, P., et al. 2002b, MNRAS, 336 907
Neistein, E., Weinmann, S. M., Li, C., & Boylan-Kolchin, M. 2011a, MNRAS, 414, 1405
Neistein, E., Li, C., Khochfar, S., et al. 2011b, MNRAS, 416, 1486
Oser, L., Naab, T., Ostriker, J. P., & Johansson, P. H. 2012, ApJ, 744, 63
Oser, L., Ostriker, J. P., Naab, T., Johansson, P. H., & Burkert, A. 2010, ApJ, 725, 2312
Panter B., Jimenez R., Heavens A.F., Charlot S., 2007, MNRAS, 378, 1550
Parkinson, H., Cole, S., & Helly, J. 2008, MNRAS, 383, 557
Pasquali, A., Gallazzi, A., Fontanot, F., van den Bosch, F. C., De Lucia, G., Mo, H. J., & Yang, X. 2010, MNRAS, 407, 937
Peacock J.A., Smith R.E., 2000, MNRAS, 318, 1144
Perez-Gonzalez P.G., et al. 2008, ApJ, 675, 234
Phleps, S.; Peacock, J. A.; Meisenheimer, K.; Wolf, C., 2006, A&A, 457, 145
Pollo, A., et al. 2006, A&A, 451, 409
Popesso P., Biviano A., Böhringer H., Romaniello M., 2006, A&A, 445, 29
Press W.H., Schechter P., 1974, ApJ, 187, 425
Purcell, C. W., Bullock, J. S., & Zentner, A. R. 2007, ApJ, 666, 20
Salpeter, E. E. 1955, ApJ, 121, 161
Scoville, N., Aussel, H., Brusa, M., et al. 2007, ApJS, 172, 1
Shankar, F., Lapi, A., Salucci, P., De Zotti, G., & Danese, L. 2006, ApJ, 643, 14
Sheth, R. K., & Lemson, G. 1999, MNRAS, 305, 946
Sheth R.K., Mo H.J., Tormen G., 2001, MNRAS, 323, 1
Sheth R.K., Tormen, G., 1999, MNRAS, 308, 119
Somerville, R. S., & Kolatt, T. S. 1999, MNRAS, 305, 1
Spergel, D. N., Verde, L., Peiris, H. V., et al. 2003, ApJS, 148, 175
Spergel, D. N., et al. 2007, ApJS, 170, 377
Springel V., White S. D. M., Tormen G., Kauffmann G., 2001, MNRAS, 328, 726
Springel V. et al. , 2005, Nat., 435, 639
Stark, D. P., Ellis, R. S., Bunker, A., Bundy, K., Targett, T., Benson, A., & Lacy, M. 2009, ApJ, 697, 1493
Strigari, L. E., Bullock, J. S., Kaplinghat, M., Simon, J. D., Geha, M., Willman, B., & Walker, M. G. 2008, Nature, 454, 1096
Tabor, G., & Binney, J. 1993, MNRAS, 263, 323
Tinker J.L., Weinberg D.H., Zheng Z., Zehavi I., 2005, ApJ, 631, 41
Tinker, J. L., Robertson, B. E., Kravtsov, A. V., Klypin, A., Warren, M. S., Yepes, G., & Gottlöber, S. 2010, ApJ, 724, 878
Tormen G., Moscardini L., Yoshida N., 2004, MNRAS, 350, 1397
Vale, A., & Ostriker, J. P. 2004, MNRAS, 353, 189
Vale, A., & Ostriker, J. P. 2006, MNRAS, 371, 1173
van den Bosch, F. C. 2002, MNRAS, 331, 98
van den Bosch, F. C., Yang, X., & Mo, H. J. 2003a, MNRAS, 340, 771

van den Bosch, F. C., Mo, H. J., & Yang, X. 2003b, MNRAS, 345, 923
van den Bosch, F. C., Norberg, P., Mo, H. J., & Yang X. 2004, MNRAS, 352, 1302
van den Bosch, F. C., Tormen, G., & Giocoli, C. 2005a, MNRAS, 359, 1029
van den Bosch, F. C., Yang, X., Mo, H. J., & Norberg, P. 2005b, MNRAS, 356, 1233
van den Bosch, F. C., et al. 2007, MNRAS, 376, 841
van den Bosch F.C., Aquino D., Yang X., Mo H.J., Pasquali A., McIntosh D.H., Weinmann S.M., Kang X., 2008, MNRAS, 387, 79
van Dokkum, P. G., Labbé, I., Marchesini, D., et al. 2009, PASP, 121, 2
Wake, D. A., et al. 2011, ApJ, 728, 46
Walker, M. G., Mateo, M., Olszewski, E. W., Penarrubia, J., Evans, W., & Gilmore, G. 2009, ApJ, 704, 1274
Wang L., Jing Y.P., 2010, MNRAS, 402, 1796
Wang L., Li C., Kauffmann G., De Lucia G., 2006, MNRAS, 371, 537
Wang, L., & Jing, Y. P. 2010, MNRAS, 402, 1796
Wang L., Weinmann, S. M., & Neistein, E. 2011, preprint (arXiv:1107.4419)
Wang Y., Yang X., Mo H.J., van den Bosch F.C., Chu Y., 2004, MNRAS, 353, 287
Wang Y., Yang X. Mo H.J., van den Bosch F.C., 2007, ApJ, 664, 608
Wechsler, R. H., Bullock, J. S., Primack, J. R., Kravtsov, A. V., & Dekel, A. 2002, ApJ, 568, 52
Weinmann, S. M., Neistein, E., & Dekel, A. 2011, preprint (arXiv:1103.3011)
Weller J., Ostriker J.P., Bode P., Shaw L., 2005, MNRAS, 364, 823
Wetzel A.R., White M., 2010, MNRAS, 403, 1072
White, M., Zheng, Z., Brown, M. J. I., Dey, A., Jannuzi, B. T., 2007, ApJ, 655, L69
Wolf C., et al. 2004, A&A, 421, 913
Yan, R., Madgwick, D. S., White, M., 2003, ApJ, 598, 848
Yang X., Mo H.J., van den Bosch F.C., 2003, MNRAS, 339, 1057
Yang, X., Mo, H. J., Jing, Y. P., van den Bosch, F. C., & Chu, Y. 2004, MNRAS, 350, 1153
Yang X., Mo H.J., van den Bosch F.C., Jing Y.P., 2005a, MNRAS, 356, 1293
Yang X., Mo H.J., Jing Y.P., van den Bosch F.C. 2005b, MNRAS, 358, 217
Yang X., Mo H.J., van den Bosch F.C., Pasquali A., Li C., Barden M., 2007, ApJ, 671, 153
Yang X., Mo H.J., van den Bosch F.C., 2008, ApJ, 676, 248
Yang X., Mo H. J., van den Bosch F. C., 2009a, ApJ, 693, 830
Yang X., Mo H. J., van den Bosch F. C., 2009b, ApJ, 695, 900
Yang, X., Mo, H. J., Zhang, Y., & van den Bosch, F. C. 2011, ApJ, 741, 13
York D., et al., 2000, AJ, 120, 1579
Zehavi, I., et al. 2005, ApJ, 630, 1
Zehavi, I., et al. 2011, ApJ, 736, 59
Zentner, A. R., Berlind, A. A., Bullock, J. S., Kravtsov, A. V., & Wechsler, R. H. 2005, ApJ, 624, 505
Zhao D.H., Jing Y.P., Mo H.J., Börner, 2003, MNRAS, 339, 12
Zhao, D. H., Jing, Y. P., Mo, H. J., Börner, G. 2009, ApJ, 707, 354
Zheng Z., 2004, ApJ, 610, 61
Zheng Z., et al., 2005, ApJ, 633, 791
Zheng Z., Coil A.L., Zehavi I., 2007, ApJ, 667, 760
Zhu, W., Feng, L.-L., & Fang, L.-Z. 2011, MNRAS, 415, 1093